SCUOLA DI DOTTORATO
UNIVERSITÀ DEGLI STUDI DI MILANO-BICOCCA

Department of

Materials Science

PhD program in **Materials Science and Nanotechnology**
Cycle XXXVI

Dating unconventional material: age of ancient mortars and vitrified forts

Miriam Saleh
784720

Tutor: Prof.ssa Anna Galli

Coordinator: Prof. Francesco Montalenti

ACADEMIC YEAR 2022/2023

I am among those who think that
science has great beauty.
A scientist in his laboratory is not only
a technician; he is also a child place
before natural phenomenon, which
impress him like a fairy tale.

- Marie Curie -

To my dear ones, for whom love knows no bounds.

Abstract

The beginnings of luminescence dating techniques can be traced back to the mid-20th century. These techniques are based on the fundamental principle of the luminescence phenomenon, which involves the emission of light by semiconductors or insulating materials upon exposure to an external stimulus. This stimulus can be in various forms, such as heat and light. The thermoluminescence (TL) phenomenon occurs when a thermal stimulus is applied.
Alternatively, when the stimulus is derived from electromagnetic radiation, a differentiation is possible according to the wavelength of the emitted light. This distinction gave rise to the development of techniques such as Optical Stimulated Luminescence (OSL), which uses visible light wavelengths, and Infrared Stimulated Luminescence (IRSL), which uses infrared wavelengths as input.
These methods have revolutionised the way researchers determine the age of materials, opening up new avenues for understanding history of the material analysed.
This thesis delves into the fundamentals of these luminescence dating methods and, most importantly, explores their application to determine the age of two unconventional materials: ancient mortars and vitrified forts.
The research presented here seeks to shed light on these material dating methods and their significance in unravelling the mysteries of the past.
Mortar dating serves as a tool for determining the construction timeline of historical buildings. Thermoluminescence (TL) was the primary well-established method for the absolute dating of brickworks. However, it has its limitations. TL calculates the time elapsed since the firing, rendering it ineffective when dealing with reused or unfired materials. In contrast, mortars are prepared shortly before use and are typically not recycled, making them an ideal subject for dating. One of the main challenges in mortar dating is the assurance of complete quartz grain bleaching. The aim is in fact to date them from the moment they received their last sunlight, thus the moment they were laid between bricks. OSL dating was conducted on more than thirty aliquots per sample to ensure statistical significance. Preliminary results revealed a discordance from the expected ages. Analysing raw curve signals emerged as a parallel alternative to standard data treatment protocols. The proposal sug-

gests working on a primitive form of algorithmic selection and prediction, primarily based on the deconvolution of the OSL signal and then selection new exclusion criteria on the raw curve shape.
These efforts aimed to align ages more closely with the expected one.
In parallel, research on vitrified fort found near Acri in Calabria, Italy was conducted. This research aimed to explore two undisclosed origin hypotheses: a natural one or an anthropic one. Evidence pointed toward an anthropogenic origin, suggesting these rocks were remnants of structures from the Late Bronze Age and Iron Age civilization. What makes this discovery even more remarkable is the absence of such rocks in the Mediterranean European region. Samples subjected to the "Prebleach with blue LEDs" protocol, an innovative way for dating glassy material. The results were promising making the protocol suitable for this material. However, the study of anomalous fading was essential to ensure accurate dating.

Riassunto

Le prime applicazioni delle tecniche di datazione con luminescenza risalgono alla metà del XX secolo. Queste tecniche si basano sul fenomeno della luminescenza, che comporta l'emissione di luce da parte di semiconduttori o materiali isolanti in seguito all'esposizione a uno stimolo esterno. Questo stimolo può assumere varie forme, come il calore e la luce. Il fenomeno della termoluminescenza (TL) si verifica quando viene applicato uno stimolo termico. In alternativa, quando lo stimolo deriva dalla radiazione elettromagnetica, è possibile una differenziazione in base alla lunghezza d'onda della luce emessa. Questa distinzione ha dato origine allo sviluppo di tecniche come la Luminescenza Ottica Stimolata (OSL), che utilizza lunghezze d'onda della luce visibile, e la Luminescenza Stimolata all'Infrarosso (IRSL), che utilizza lunghezze d'onda dell'infrarosso come input.
Questi metodi hanno rivoluzionato il modo in cui i ricercatori determinano l'età dei materiali, aprendo nuove strade per la comprensione della storia del materiale analizzato.
Questa tesi approfondisce i fondamenti di questi metodi di datazione a luminescenza e, soprattutto, ne esplora l'applicazione per determinare l'età di due materiali non convenzionali: le malte antiche e i vitrified forts.

La datazione della malta è utile per determinare la cronologia di costruzione degli edifici storici. La termoluminescenza (TL) è stato il metodo principale e consolidato per la datazione assoluta dei mattoni. Tuttavia, questo metodo ha i suoi limiti. La TL infatti calcola il tempo trascorso dalla cottura del materiale, ciò lo rende un metodo inefficace quando si tratta di materiali riutilizzati o non cotti. Al contrario, le malte vengono preparate poco prima dell'uso e in genere non vengono riciclate, il che le rende un soggetto ideale per la datazione della costruzione per cui sono state prodotte. Una delle sfide principali nella datazione delle malte è la garanzia di un completo sbiancamento dei grani di quarzo. Lo scopo è infatti di datare dal momento in cui hanno ricevuto l'ultima luce solare, quindi il momento in cui sono state stese in opera. La datazione OSL per questa ricerca è stata condotta su più di trenta aliquote per campione per garantire la significatività statistica. I risultati preliminari hanno rivelato una discordanza rispetto alle età previste. L'analisi dei segnali delle curve grezze è emersa come un'alternativa ai protocolli standard di trattamento dei dati. La proposta suggerisce di lavorare su una forma primitiva di selezione e previsione algoritmica, basata principalmente sulla deconvoluzione del segnale OSL e sulla selezione di nuovi criteri di esclusione sulla forma della curva grezza.
Parallelamente, è stata condotta una ricerca sul forte vetrificato rinvenuto nei pressi di Acri, in Calabria, Italia. Questa ricerca mirava a esplorare due ipotesi di origine discusse: una naturale o una antropica. I risultati hanno portato ad propendere per l'origine antropica, suggerendo che queste rocce erano resti di strutture della civiltà della tarda età del bronzo e/o dell'età del ferro. Ciò che rende questa scoperta ancora più notevole è l'assenza di rocce di questo tipo nella regione europea mediterranea. I campioni sono stati sottoposti al protocollo "Prebleach with blue LEDs", un metodo innovativo per la datazione di materiali vetrosi. I risultati sono stati promettenti, rendendo il protocollo adatto a questo materiale. Tuttavia, lo studio del fading anomalo è stato essenziale per garantire una datazione accurata.

Acknowledgement

Marie Curie's words encapsulate the profound lessons learnt on this doctoral journey: the wonder at the beauty of science and the ability to face the challenges of research. Like children, we often find ourselves in need of guidance, taking steps towards what we do not know, driven by the desire to start our own path.

The choice of Marie Curie's phrase is intentional, because she is an outstanding woman in science, an identity that has always filled me with pride. To begin my gratitude, I thank two women who have been my guides during this PhD.

Firstly, I express my gratitude to Professor Anna Galli. Thanks to her guidance and understanding even in misunderstandings. She constantly challenged and pushed me to give my best.

Special recognition is due to Dr Laura Panzeri, who deserves a special place on the cover of this thesis. My debt to her goes beyond mere acknowledgement; she has been the source of my knowledge and expertise in this work. I also appreciate the countless hours spent together in the red light of the laboratory.

My gratitude extends to the entire LAMBDA lab team for the engaging discussions, the imparting of non-trivial knowledge.

All my appreciation goes to Professor Georgios S. Polymeris, Dr Efstathios Tsoutsoumanos and the entire Institute of Nanoscience and Nanotechnology of the NCSR 'Demokritos' in Athens. Your warm welcome and collaborative spirit fuelled the flame of my research, creating a sense of belonging despite the geographical distances.

I would also like to thank the working groups of the University of Padua and the University of Modena and Reggio Emilia. Their valuable contributions have served as both samplers and early supporters of further research efforts.

Finally, I want to thank Prof Flavia Groppi, whose encouragement has been a constant motivation. Her insight not only confirmed the pursuit of research, but also revealed the rewarding nature of teaching, a revelation that has enriched my academic journey.

I'll be there someday, I can go the distance
I will find my way if I can be strong
I know every mile would be worth my while
When I go the distance, I'll be right where I belong

Contents

Another brick in dating cultural heritage

The development of luminescence dating techniques can be traced back to the 50s and 60s years of the past century. [1, 2]
The fundamental principle is the *luminescence* phenomenon. That is an emission of light from a semiconductor or a insulating material after these have been exposed to an external stimulus. Heat and light are two examples of stimulus.
The *Thermoluminescence (TL)* occurs when a thermal stimulus is present. Otherwise, in the case of stimulus originating from electromagnetic radiation, differentiation can be achieved based on the wavelength of the emission. Thus, has led to the development of techniques like *Optical Stimulated Luminescence (OSL)*, which uses light with visible wavelengths, and *Infrared Stimulated Luminescence (IRSL)*, which uses infrared wavelengths as the input [3, 4].
Nowadays, luminescence dating methods are successfully used in fields such as geology and archaeology.
The fundamentals of these dating methods and their application to determine the ages of two unconventional materials, ancient mortars and vitrified forts, will be discussed in this thesis.

The discussion will be divided into two distinct part. The first one will be dedicated to the theme of dating mortars [Part I - page 5]. The second part will delve into the enigmatic vitrified fort discovered in the town of Acri, Calabria [Part II - page 97].

The dating of mortars always remains an intriguing research topic in insights and possibilities [Chapter 3 - page 21]. Nevertheless, its complete validation remains an ongoing research. This thesis has the challenge of enhancing our understanding of OSL dating, with a primary focus on the issue of bleaching. To deal with this challenge, an innovative approach that involves

an in-depth analysis of the raw curve's characteristics is proposed [Chapter 4 - page 25]. The study of the OSL signal will include an examination of its components derived through deconvolution [Section 4.3]. Furthermore, we discuss novel criteria, skewness and kurtosis, generated from residual distribution analysis (RDA), a method rooted in descriptive statistics, to distinguish usable OSL signals for dating from those requiring further analysis [Section 4.6]. In conclusion, we will propose a new analysis path for handling mortar dating data, an effort that is based on a comprehensive understanding of the nature of mortar [Chapter 7 - page 51].
This cannot be done without knowledge of how a mortar is prepared. Will be offer a concise introduction to the process of mortar preparation, a fundamental precursor to understanding the application of dating techniques to the datable material [Chapter 1 - page 5]. This will be necessary in order to understand where dating techniques can come into play on the datable material. Moreover, an in-depth examination of the techniques employed in this thesis will be discussed [Chapter 2 - page 9]. It will also be shown in chapter 2 how an OSL curve has several components and how these can be studied [Section 2.2].
The mortars involved in this research come from four distinct sites located throughout Italy [Chapter 5 - page 37]. All samples were analyse at LAMBDA laboratory (LAboratory of Milano-Bicocca University for Dating and Archaeometry) [Chapter 6 - page 45].
Finally, will be presented the focus on the specific date results to a discussion of the procedural characteristics that should define the mortar dating process upon the conclusion of this research segment [Chapter 8 - page 91].

Part II will be exclusively dedicated to the mysteries surrounding the vitrified forts. Many scholars have attempted to understand their origin and age, but this is surrounded by uncertainty [Chapter 9 - page 97]. First attempts to comprehend their origin and age began only at the end of the last century, with the application of the thermoluminescence method [Section 9.1 - page 102]. However, dating materials with a glassy nature has posed persistent challenges [Chapter 10 - page 105].
Many attempts have been unsuccessful for various reasons, including signal fading [Section 10.1 - page 106]. In response to these challenges, this the-

sis work introduces an innovative protocol, referred to as ”pre-bleached with blue LED” [Section 10.2 - page 107].
The material under investigation comes from Monte Serravuda, near Acri in Calabria. A team of geologists from the University of Modena and Reggio Emilia characterized the samples. An extensive discussion of the origins at the end of the geological and chemical characterisation was carried out by them [Chapter 11 - page 111].
Building upon this work, our research has the aim to provide insights into the age and origins of this material. The question of whether these rocks are a product of human activity or the result of natural phenomena has been a subject of ongoing debate. Through the application of the ”pre-bleached with blue LED” protocol and the correction for signal fading, the obtained dates appear to trace back to the ancient Bronze Age [Chapter 12 - page 121].
While the origins of these vitrified forts still under debate, the introduction of this new dating protocol offers promise, making dating a feasible work. This development holds the potential to play a crucial role in understanding and unravelling the mystery of these vitrified forts [Chapter 13 - page 137].

List of Acronym

TL Thermoluminescence

OSL Optical Stimulated Luminescence

IRSL Infrared Stimulated Luminescence

LED Light Emitting Diod

ED Equivalent Dose

MAAD Multiple Aliquot Additive Dose

SAR Single Aliquot Regenerative Dose

MG Multigrain

SG Single-grain

MAM Minumum Age Model

CAM Central Age Model

RDA Residual Distribution Analysis

AD Anno Domini

BC Before Christ

FWHM Full Width at Half Maximum

FOM Figure Of Merit

Part I

Mortar Dating

1 Mortar

A mortar is an artificial composite substance consisting of a binder and an aggregate material that is laid between masonry elements (bricks and stones) [5, 6].
Binder is defined as that material which, when mixed with water, allows the formation of an easily workable substance with the ability to consolidate and form a single solid structure. The binder defines the type of mortar, and the choice of binder also suggest the history of mortars use. Initially, simple clay-rich mud was used as a mortar, later the binders since ancient times were carbonate based (calcite, dolomite [$CaCO_3$], [$MgCO_3$]), sulfate (gypsum [$CaSO_4 \cdot 2(H_2O)$]) or aluminium-silicate based (cements).
Pure binders are rarely used; aggregates are then added. These are non-reactive phases, such as quartz contained in sand, gravel or pozzolan. Thus, the role of the aggregate is to reduce fractures during hardening process and allow the binder volume to increase. Usually the aggregate has size in the range of sands (0.6-0.8 mm). Inorganic and organic components (e.g., ceramic fragments, charcoal) can also be found in mortars.
The important concept in understanding mortar's production is that heating and then hardening allow a reactive material to be transformed into a more stable one. The major differences between binders, and consequently mortars, are (1) the nature of the initial material that drives the chemical reaction, and (2) the temperature at which the heating takes place [5, 7].
Another difference is the nature of hardening, which may involve simple absorption of CO_2 from the atmosphere to produce carbonates or pozzolanics reaction involving dissolutions of aluminosilicates, and the presence then of silicate hydrates. The former are called aerial (or non-hydraulic) binders because they harden in contact with the atmosphere. The latter are called hy-

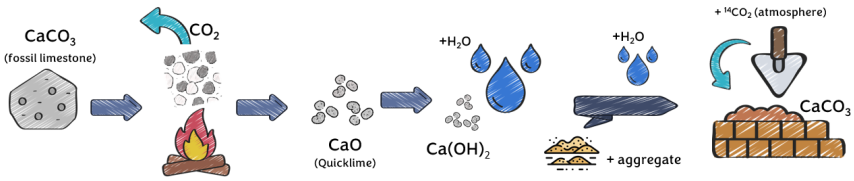

Figure 1.1: Mortar making process, from $CaCO_3$ in the limestone to binder and mortar [9]

draulic binders because they can also harden in contact with water. Reactions generally occur kinetically quickly under ambient conditions [5, 8].

1.1 Mortar preparation

The technology behind the production of mortar is quite simple and is shown in figure 1.1.

In general, the reactions involved in the use of lime can be summarized as follows:

1. **Lime production:**
   $CaCO_3$ (calcite) + heat $\rightarrow$ CaO (lime) + CO_2 (carbon dioxide)

2. **Rapid hydration:**
   CaO (lime) + H_2O (water) $\rightarrow$ $Ca(OH)_2$ (Portlandite) + heat

3. **Long-term carbonation:**
   $Ca(OH)_2 + CO_2 \rightarrow CaCO_3 + H_2O$

The temperature required to produce CaO (phase 1) should be around 850 °C, although carbonate decomposition can also occur at lower temperatures (780-800 °C) under reducing conditions. Temperatures reached by the kilns are in the range of 920-1000 °C: higher temperatures should be avoided as they could lead to unreactive lime. The production of lime requires a great deal of energy and a large amount of biomass for heating.
The kilns used for firing carbonates are massive formations up to several meters high.

Limestone blocks are lowered from the top and burnt for days. Wood or coal are constantly added to the combustion chamber at the base of the kiln. The blocks then fired are crushed to obtain quicklime powder, an unstable compound that could give reaction already upon exposure to the humidity of the atmosphere. If CaO is mixed with water in a stoichiometric way the product is a dry powder. The required amount is added to produce Portlandite ($Ca(OH)_2$). This process is called dry hydration. If, on the other hand, the CaO powder is mixed in excess of water then a smooth paste is obtained in form of slurry (fluid mortar); the process is called "lime quenching". Portlandite paste (slaked lime or putty) can then be used as a binder for architectural component or as a raw material for modelling even art objects. After its application, the paste reacts with atmospheric carbon dioxide and produces a hardened material composed of microcrystalline calcite. The kinetics of the carbonation reaction is slow, as a result some residual Portlandite grains may also not react. During carbonation and hardening, the nature of the slaked lime paste changes considerably. The presence of calcite nodules has been widely discussed as to their importance in identifying ancient mortars, partly because of the need to determine the original proportion of binder to aggregate. Three sources of calcite nodules can be identified: (1) Residue of unfired geological carbonate; (2) Formation of non-uniform slaked lime leading to Portlandite during successive carbonations; (3) Subsequent precipitation of calcite [5, 10, 11].
The importance of identifying precipitated calcite is related to the fact that it is the only one associated with to the hardening of the mortar at the time of laying.

The technique of mortar preparation is an ancient tradition that has lasted over time. Revealing its hidden complexities can provide insights to discern datable phases and shed light on the evolution of this technology.

2 Luminescence dating

Knowing when archaeological and geological materials were last exposed to light or heat constitutes an essential information in dating. Luminescence dating methods like Thermoluminescence (TL) or Optically Stimulated Luminescence (OSL) can be used to gather this information.
These two techniques are based on a common mechanism. Whereby electrons are trapped by the interaction of ionising radiation with matter. Afterward, light emission occurs as a result of heating to a high temperature or exposure to light (a bleaching event). Ceramics, bricks, and mortar include quartz and feldspar grains, which act as dosimeters and may record the radiation dose they were exposed to [1, 3]. Radioactivity is everywhere in the environment and in the samples themself. Quartz and feldspar minerals contain radioactive isotopes, such as uranium (U), thorium (Th), and potassium (K), which absorb a fraction of the energy emitted by radiation. This absorbed energy is subsequently released as light and measured in the process known as luminescence dating.
The dose value obtained provides information on the time elapsed since the last heating/light exposure event.
In the materials of interest (e.g. mortars, bricks), quartz and feldspars can both be used as dosimeters, however the latter become vulnerable to the anomalous fading phenomenon [4]. Due to the instability of deep traps, anomalous fading causes signal loss progressively, which might cause an underestimation of the sample age.

The total amount of absorbed energy resulting from quartz's interaction with natural radiation after the zeroing event has to be calculated for dating. This value is called paleodose or Equivalent Dose (ED) and the amount of absorbed energy per mass of mineral is equal to 1 J kg^{-1} = 1 Gy (Gray). The

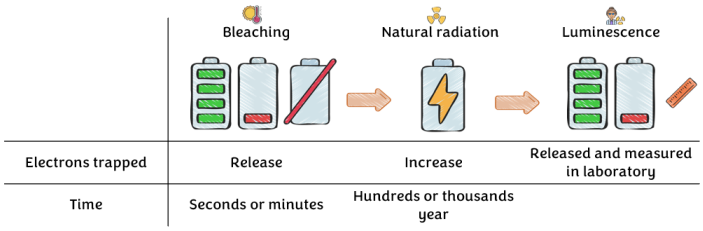

Figure 2.1: A useful analogy with the rechargeable battery for understanding the behavior of mineral grains and how luminescence dating works

Equivalent Dose (ED) is determined by comparing the natural luminescence signal with an artificially induced luminescence signal.
The age will be established by comparing the ED with the dose rate, defined as the amount of energy deposited per mass of mineral as a result of radiation absorbed over a specific amount of time, tipically a year (radiation absorbed annually, Gray/years).
This relationship is represented by the following equation and is referred as ”age equation”:

$$Age(years) = \frac{\text{Equivalent Dose}(Gy)}{\text{Annual Dose}(Gy/years)} \tag{2.1}$$

To understand the dating process is common to use analogy with rechargeable batteries (see figure 2.1). If the mineral grain of the sample is imagined as a battery, its exposition to a resetting event released all its energy. Hereafter, the battery starts to recharge. It is exposed to the natural radioactivity, and as the time pass more energy can be stored. At the moment of laboratory measurement this energy is release in form of light: the luminescence signal. The stored energy is proportional to the brightness of the luminescence signal. By knowing how fast the battery is charged, one can know the charging time and thus the period of time since the battery was last emptied.

2.1 Thermoluminescence (TL)

Thermoluminescence is a luminescence phenomenon that occurs when certain materials, usually semiconductors or isolating crystals or minerals, are heated after being irradiated with ionising radiation. In nature there are some natural dosimeters, as quartz and feldspars, that if exposed to natural source of ionising radiation act as chronometers [12, 13].
After being exposed to ionizing radiation, the material's crystal lattice entraps electrons in metastable levels in the forbidden energy gap. The trapped electrons are released from the higher energy states and return to the lower energy levels when the material is heated (e.g during brick baking). Visible light, which can be detected and measured, is the physical manifestation of energy which is emitted.
The resulting graph (glow-curve) shows the TL light intensity as a function of temperature. A peak will be obtained at each trap in the material. A sample that undergoes to a Thermoluminescence (TL) measurement is prepared following the so-called fine grain technique [14]. The aim is to obtain mineral grain size fraction in the range of 1-8 μm. Particle size separation is achieved by taking advantage of the fact that the settling time of grains is determined by their diameter. The powder taken from the material is placed in acetone for the time required to obtain grains of the desired size. The grains obtained are then resuspended in acetone. As the acetone evaporates, it leaves a deposit a few microns thick on stainless steel disks [14].

2.2 Optically Stimulated Luminescence (OSL)

Optical Stimulated Luminescence (OSL) is a luminescence dating technique that involves light to release electrons trapped in minerals and crystals. As in thermoluminescence, charges are trapped as a result of the interaction of mineral crystals with ionizing radiation [4, 15].
The primary focus of early applications was sediment [16]. In this case, a coarse-grained preparation is utilized [17]. After a preliminary sieve selection (100-300 μm), the sample powder undergoes chemical attacks. First step is removing organic material using H_2O_2 (10%) treatment for one day. This is followed by a 6-hour HCl attack to dissolve the carbonates. At last, etching

treatments with HF (48%) are carried out for roughly 40 minutes to eliminate the feldspathic component. If necessary, sodium polytungstate is used to separate minerals based on their density, this method is known as heavy liquid separation. In priciple, only the presence of quartz grains with the required grain size should be examined at the conclusion of the treatment.

The OSL technique's main limitation is the inability to verify that the signal has completely bleached before the last exposure to the light. The age and the time of zeroing event might not match in the case of a residual signal. Although the causes of incomplete zeroing are still being investigated, it is evident that one of the factors is the presence of quartz from various sources [4].
The plateau test may be used to determine the bleaching level. The absence of a plateau is an indication of occurrences that had place during the process or preparation, such as the existence of contamination, insufficient bleaching, or proof that part of the geological signal is still present. The plateau test was initially developed to determine where the age equation (see eq.2.1) is applicable. The existence of the plateau suggests that the traps have a long enough lifespan to be compared to the sample's age.
The test consists of plotting the Equivalent Dose as a function of optical stimulation time. Each signal will be more sensitive to the optical stimulus than the next stimulus imparted. The result is a flat plot for zeroed samples, and an increasing plot for unbleached samples [18].

OSL components

In the OSL technique, the trapping phenomenon can be detected by changing the temperature and wavelength. This approach allows three distinct components of the OSL curve to be identified, called fast (OSL_f), medium (OSL_m) and slow (OSL_s). These components show different rates of luminescence decay upon optical stimulation [4, 19, 20].
The individual components are intricately linked to specific families of traps, as outlined by the quartz band model. Within this trap model, there exists a spectrum of intermediate states positioned between the valence and conduction bands, commonly referred to as "traps." These traps have the capacity to

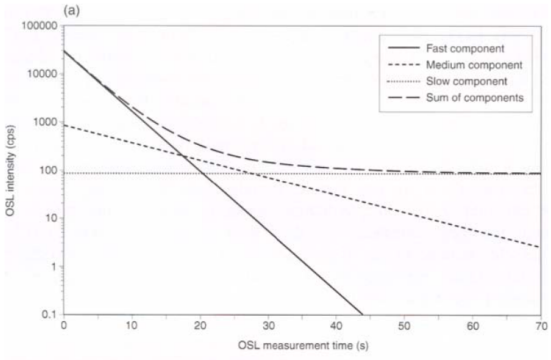

Figure 2.2: OSL decay curves recorded by Bøtter-Jensen by subjecting naturally irradiated sedimentary quartz to a 70-second stimulation at 160°C using a filtered halogen lamp. The acquired signal shows the three exponential components, classified as fast, medium and slow [4].

induce various effects, and each of the three components is distinctly associated with distinct trap families [4]. Traditionally, OSL dating focuses mainly on extracting signals from the initial seconds of OSL decay curves. In fact, the Single Aliquot Regenerative (SAR) protocol, the one used to determine ED (see section 2.3), has shown remarkable efficiency, particularly when dealing with quartz samples dominated by the fast OSL component [21]. Isolating and focusing the measurement on this component is therefore the aim of the curve component analysis. The fast and medium components are restored by an exposure to sunlight of only a few seconds. This allows for sure the isolation of the slow component initially characterised by Bailey [22]. In any dating technique, a fundamental requirement is to establish a baseline for the signal over time, either at zero or at a value known at the time of the event to be dated. Identifying samples where the OSL signal has been partially zeroed prior to deposition is critical and leads to attempt to isolate the fast component.
Smith and Rhodes initially identified the three quartz components, suggesting that OSL decay is not a simple exponential process [23]. There are two interpretations of this model:
1. stimulating light initially releases a charge from a trap; effects such as retrapping of the charge (a charge being released and then trapped again) may be responsible for the non-exponential OSL decay.
2. The effect of processes such as retrapping on the observed OSL decay is

minor and the decay represents the release of charge from traps with different rates of charge loss.
If the first interpretation is correct, it seems unlikely that partial bleaching can be detected. However, the second interpretation suggests that the observed form of OSL decay would change depending on the degree of bleaching and that partial bleaching should be detectable. In general, however, the possibility of a constant rate of trapping in other bleaching or thermally unstable traps cannot be completely dismissed. In conclusion, it is highly unlikely that a single trap type is responsible for the measured OSL.

According to Bailey, the slow component of the OSL emission accounts for a considerable amount of charge, while, the fast component decreases with increasing bleaching time [19, 22]. It is therefore suggested that the observed changes in the shape of the OSL decay measured at room temperature following partial bleaching are a function of a progressive change in the ratio of the signal dominated by the fast and medium components. As the duration of partial bleaching increases, a higher percentage of the fast signal is depleted compared to the medium component. The medium component also often plays a crucial role in the first moments of decay of the OSL curve.
The quartz model is still under discussion, but it can be assumed that the fast and medium OSL components derive from emission at longer wavelengths, and they derive from charges trapped in two slightly different lattice positions.
The exact mechanism responsible for the signal of the slow OSL component remains less clear [22]. However, its longer wavelength emission suggests recombination in a luminescence centre distinct from the fast and medium components, possibly facilitated by localised transitions in the core of the luminescent centre.
The aim of employing OSL is not only to recognize samples that have been subjected to light but, critically, to comprehend the mechanism by which this light released electrons from their trapped states. The examination of the curve components plays a pivotal role in determining whether the samples might have inadvertently encountered even minimal light exposure during their collection or preparation. This issue of bleaching analysis will be crucial when dealing with OSL dating.

2.3 Equivalent Dose measurement

We refer to the Equivalent Dose (ED) as the total amount of ionizing radiation to which a mineral or crystal has been exposed since it was last reset by sunlight or heat. In reference to the age equation (see eq.2.1), this measurement represents its numerator. Once the sample has been prepared, the determination of the ED is made in several steps:

- **Irradiation**: With a calibrated radiation source (α, β or γ), the sample is exposed to a known dose of radiation. By determining the sensitivity of the sample's responsiveness to ionizing radiation, it is possible to build a calibration curve. The purpose of calibration is to correlate the sample's proper luminescence signals with the given known dose to which it has been exposed.

- **Preheating**: This step allows the removal of all unstable components of the luminescence signal. By heating the sample, all shallow traps are emptied of the electrons charges [24].

- **Luminescence**: the amount of light emitted by the sample when stimulated by light or heat is obtained.

For Equivalent Dose assessment, it will be necessary to make the comparison between the luminescence signal emitted naturally by the sample (natural dose) and the artificial doses given in the first step. There are two different approaches for this comparison: additive dose method and regenerative dose method.
The *additive method*, typically used in thermoluminescence, adds the imparted dose to the natural one. The *regenerative method*, on the other hand, regenerates the signal after it has been removed and the sample has been re-irradiated. This method is typically used in Optical Stimulated Luminescence (OSL). The construction of a dose response curve will be necessary to understand the relationship between the radiation dose and the luminescence signal for the sample.

The additive dose method

The additive dose method is particularly useful for samples that might have experienced incomplete resetting, as it accounts for both the natural luminescence signal and the added artificial doses to determine the paleodose.
For the additive dose method, multiple aliquots are used and the protocol is known as MAAD (Multiple Aliquot Additive Dose [3]). These are separated into two groups with an equal number of aliquots. For the first group the signal due to the natural dose is measured. The other group will be irradiated adding the irradiated dose to the natural dose.
By plotting the signal against the cumulative dose for each incremental step, the growth curve at the dose is constructed. Finally, by extrapolating the dose-response curve, the natural luminescence signal is interpreted. This extrapolation allows the estimation of the cumulative dose that would correspond to the natural luminescence signal of the sample.
The main issues with this method are related to the fact that not all aliquots yield the same dose response. These behaviors can complicate the interpretation of the dose-response curve and lead to inaccurate Equivalent Dose estimation [18].
Moreover, some samples may exhibit anomalous luminescence behavior, such as sensitization or a nonlinear response. Despite these drawbacks, the additive dose method remains a valuable tool for luminescence dating.

The regenerative dose method

The regenerative dose method finds its primary application in Optically Stimulated Luminescence dating (OSL). All measurements are carried out on a single aliquots of the sample, yielding several advantages such as the elimination of unnecessary normalization, reduced sample requirement, faster measurement times, and enhanced accuracy [25]. The most widely employed version of this approach, known as the Single Aliquot Regenerative Dose (SAR) protocol, was introduced by Murray and Wintle in 2000 [21, 26, 27]. In SAR protocol, the natural luminescence signal of each individual aliquot is measured, and subsequently an artificial dose is imparted in successive cycles, in a regenerative measurement. By comparing the luminescence signal following regenerative treatment with the initial natural luminescence signal, a growth

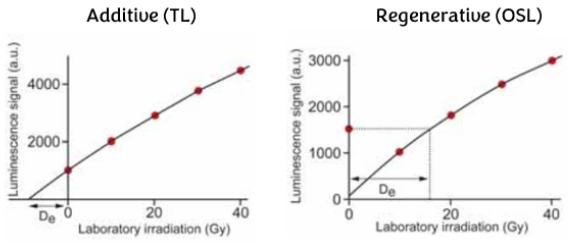

Figure 2.3: Two ways to calculate De from luminescence measurements, additive on the left and and regenerative on right

curve is generated. The Equivalent Dose is then obtain by interpolating the natural OSL signal value from this growth curve.
Early concerns in SAR were focused on the sensitivity variations arising from different irradiation and bleaching cycles [28]. To address this problem, a test dose was incorporated into the protocol. Test dose value remaining constant throughout the cycles and applied after each regenerative measurement, including the initial natural one. The key steps in a SAR protocol are: dose imparted (D_i), preheating, luminescence reading (L_i), test dose (D_t), preheating, and OSL measurement (T_i)[26]. For a comprehensive understanding of the difference between the method, reference can be made to figure 2.3.

Furthermore, two test were build to monitor the progress of the cycles, namely the recuperation and recycling ratio tests.
The *recuperation test* measures the degree of complete bleaching achieved after each irradiation [2], involving a new OSL measurement at the conclusion of the cycle. While, *recycling test* consists of applying the same dose in two distinct cycles (often the first regenerative dose). This test helps to validate the sensitivity correction.
An additional test, the *dose recovery test*, on the other hand, was introduced to validate the suitability of the SAR protocol. This test aims to confirm that a known laboratory-delivered dose can be accurately reconstructed during measurement. The procedure involves optically bleaching the natural signal of an aliquot, applying a known dose, and subsequently initiating a new cycle using the SAR protocol parameters. If the resulting measurement successfully reconstructs the dose value, the employed parameters are assumed to be appropriate [2, 18]. A complete SAR protocol is illustrated in figure 2.4.

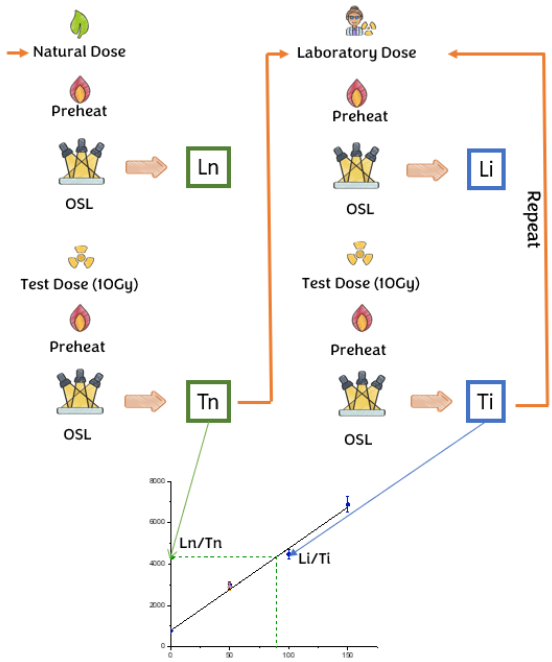

Figure 2.4: The quartz sample undergoes SAR protocol. This involves subjecting the sample to various regeneration doses, and measuring the resulting OSL signals (L1, L2, etc.). Following each measurement, the luminescence sensitivity is determined by a test dose, and measuring the resulting OSL signal (T1, T2, etc.). By plotting the sensitivity-corrected OSL (Lx/Tx) against the laboratory dose, the value of ED for that specific sample can be determined.

2.4 Dose Rate evaluation

To perform dating, it is essential to calculate the dose rate (see eq. 2.1), which represents the amount of radiation absorbed by the sample in a specific period of time (we can refer to the annual dose if we consider this period corresponding to one year). The dose rate should be considered constant throughout the "life" of the analysed sample. The presence of naturally occurring radioactive elements such as uranium (U), thorium (Th) and potassium (K) in the sample and its surroundings contributes to the environmental radiation absorption. To accurately assess the dose rate, four types of radiation need to be taken into account: alpha particles (α), beta particles (β), gamma rays (γ) and cosmic rays (R_c). As a result, the dose rate can be seen as the sum of different

contribution of radiation:

$$D = D_\alpha + D_\beta + D_\gamma + D_{R_C} \tag{2.2}$$

Dose rate assessment involves two aspects: the analysis of radioactivity within the sample itself, and the measurement of radioactivity in the surrounding. In addition, the reduction of radiation contribution must be taken into account. The initial assessment concerns water content, as water in the sample absorbs radiation that would otherwise affect the grains, potentially leading to an underestimated age [14]. Moreover, the size of the grains during sample preparation is another factor to consider, as changes in size affect the absorption capacity [1].

The factors that need to be taken into account when calculating the dose rate are associated with the process of preparing the sample. When utilizing the TL dating method with the *fine-grain* approach, the samples undergo a preparation step involving the removal of the initial 2mm layer of the surface. This action effectively renders the α and β radiation from the external surroundings insignificant. In quartz, α radiation can only penetrate to a depth of approximately 20-30 μm, whereas β radiation can reach depths of 2-3 mm [1, 18, 29]. Moreover, the thermoluminescenceproduced at the same dose by β and γ radiation is almost the same, while it is substantially less for α radiation, lower by a factor called the a-factor (a in the equation). As a result, the age can be calculated considering D_α and D_β value from sample and correct for the water:

$$Age(years) = \frac{EquivalentDose\ (Gy)}{a \cdot D_\alpha + D_\beta + D_\gamma + D_{R_C}} \tag{2.3}$$

When employing the *coarse-grained* preparation method, commonly used for OSL dating, the impact of α particles can be dismissed. The outer layer of grains they might penetrate (10 μm) is eliminated through the use of HF during the preparation process. The significant considerations involve the components of beta (β) and gamma (γ) radiation [1, 18, 29]. The age equation for samples prepared using the coarse-grained approach is therefore formulated as:

$$Age(years) = \frac{EquivalentDose\ (Gy)}{D_\beta + D_\gamma + D_{R_C}} \tag{2.4}$$

3 Mortar dating

3.1 In the beginning there was thermoluminescence, then it was the light

Dating the phase of construction of a building has always been a deeply explored and debated line of research, hence the search for datable building materials.
However, the use of luminescence as a dating technique began with the opportunity to date ceramic artifacts. Early studies of the potential use of thermoluminescence on ceramic objects were consolidated in Martin Aitken's research group at Oxford University in the early 60s [30, 31].
The procedure of sample preparation was studied in the 1970s by Fleming's group and Zimmermann's group. The former proposed a preparation called coarse-grain while the latter the so-called fine-grain; these two approaches differ for the size of quartz grain isolated from ceramics [14, 17]. The thermoluminescence technique was then used on bricks, which was an essential starting point in dating buildings [32, 33]. The method for determining the time of firing quickly spread throughout Europe and developed into a thriving field of research [34–36]. The line of research, however, soon had to face an issue: the bricks of an architectural structure may have been reused [37–39].
In a building, mortar stands out as the sole component that cannot be feasibly reused due to its irreversible hardening process. Conversely, this limitation does not apply to other construction materials, including metal, wood, brick, binder, and stone, which can typically be recycled or repurposed. Mortar dating actually began on the basis of this premise.
Radiocarbon was the first possible dating method for this material. Once the lime binder has been put in place, it is expected that the carbonation process

will occur rapidly in accordance with the architectural history of the building. Therefore, determination of the radiocarbon concentration of the binder would indicate the age of the construction phase. Problems might arise, if there are carbonate impurities from a variety of sources, such as secondary phases containing fossil CO_2, geological limestone pollution, and secondary calcite from dissolution and reprecipitation (see section 1.1) [40, 41]. Afterwards, Optical Stimulated Luminescence (OSL) was suggested as a technique for dating mortars. OSL establishes time that has elapsed since the mineral quartz grains were last exposed to sunlight [15]. The critical point for dating mortars occurs during preparation. The ideal situation requires the quartz in the added aggregate to the binder to be bleached during mortar mixing. But it didn't always happen [29, 42]. This critical point is the cause of numerous uncertainties in dating campaigns [43–47].
The dosimetric properties of mortar were acknowledged by the Bøtter-Jensen's research in 2000 [25]. Early dating attempts, however, frequently failed because the age to be attributed to the analytical method utilized, the Multigrain (MG) technique, was overestimated [42, 48]. Using tens or hundreds of grains at once, the Multigrain approach calculates the average luminescence signals that are produced.
It immediately became obvious that the multigrain choice could only be an effective solution if all of the quartz grains in the mortar had undergone light bleaching throughout their preparation [47, 49, 50]. Although the signal will always be regarded as average [29], limiting the amount of grains on the disc, with so-called small aliquots (not exceeding 300 grains), can be a solution to reduce the disparity of bleaching degrees and the influence of unbleached grains.
What becomes clear is that using the Single-grain (SG) approach should be considered as an alternative to the multigrain strategy. Thus, it enables the recording of the OSL signal of each individual quartz grain, allowing better bleached grains to be separated from a mixture of insufficiently and/or poorly bleached grains [4, 26, 28]. The recent research on the Single-grain method has demonstrated that the location of mortar production and signal intensity are connected to the method's efficacy [51]. The fact that often just a small amount of grains provides suitable signals makes the procedure time-consuming. Another constraint on the method is definitely the quantity of grains that must

be employed.
Nowadays, mortar dating is a recognized method for establishing the age of a building. Nevertheless, because of its recent application, studies conducted so far have always had a dating range to deal with. Despite these limitations, it has been shown that in several contexts there is correspondence with the known age of the building [45, 52, 53].

4 Beyond bleaching: statistical data treatment

In mortar dating research, reliability remains a concern. To enhance data representation, it is imperative, in most instances, to establish supplementary selection and filtration criteria alongside existing tests (recycling ratio and recovery test). The primary aim of this study is to systematically explore and identify these criteria.
It is worth emphasizing that the approach presented in this study seeks to enhance the selection of suitable raw OSL signals by introducing a new verification criteria. All additional criteria and probes will be derived exclusively from the statistical analysis of the raw OSL signals, which are routinely measured as part of a Single Aliquot Regenerative (SAR) OSL protocol [26]. Furthermore, the newly developed probes will be based solely on the shape and characteristics of the raw OSL signal. Additionally, this study will explore the deconvolution analysis with the final goal to select the appropriate background (late or early). The new approach will encompass two distinct statistical analyses: (a) a conventional stimulated luminescence analysis, including deconvolution, and (b) a descriptive analysis, specifically focusing on the symmetry of these distributions, known as Residual Distribution Analysis (RDA).

4.1 Data treatment

Statistical analysis is essential to identify uncertainty. In the field of OSL dating, an example of uncertainty is the presence of grains that have not undergone complete bleaching. This raises difficulties in accurately calculating the Equivalent Dose.
The conventional SAR protocol is based on several straightforward test, no-

tably the recycling ratio and recuperation (see section 2.3). These two parameters, evaluated for each individual aliquot, serve as robust indicators, guiding the acceptance or rejection of the equivalent dose calculations associated with those particular aliquots [21, 26, 27]. Hence, a statistical approach was also found to discard such grains during the final stage of equivalent dose determination. Early statistical methods and models are known as "age models." They were first formulated for the dating of fission track [54, 55].

The determination of Equivalent Dose values relies significantly on the parameters used for its calculation, such as the specific region chosen for integrating the signal and the background [56]. In numerous routine investigations, these decisions are often made without the benefit of experimental validation or a substantiated rationale. The alternative method proposed in this thesis uses the direct analysis of the raw OSL curve. This consists of a process called *deconvolution*, which aids in comprehending the factors influencing the decay curve of the OSL signal.
The Single Aliquot Regenerative (SAR) protocol (see section 2.3) has demonstrated its efficacy, particularly for quartz samples dominated by the fast OSL component (OSL_f), as established by Wintle and Murray in 2006 [21]. In fact, conventional OSL dating practice often uses the early phase signal of OSL decay curves, the one with the lowest recombination lifetime.
The objective of employing deconvolution analysis is to separate the fast component and use only this particular segment for dating purposes. By examining the distinct characteristics of the unprocessed curve, it becomes possible to formulate criteria for selecting the most suitable distribution of Equivalent Dose.

4.2 Age Models

The age models developed for determining equivalent dose are applicable to both bleached and incomplete bleached samples. Here are several age models commonly used in OSL dating:

- Central Age Model (CAM): The CAM assumes a uniform distribution of absorbed dose in the interval between the sample bleaching event and

the present. This model calculates an age equivalent to the midpoint of this dose distribution [54, 55].

- Basic Statistical Age model (BaSAR): The BaSAR is a simple statistical age model that takes into account the variability of dose rates in the surrounding environment. It derives an age estimate by considering the cumulative dose and dose rate of the sample [57].

- Minimum Age Model (MAM): The MAM approximates the minimum age of a sample by considering the lowest conceivable dose rate. It is based on the assumption that the dose rate has consistently maintained the lowest attainable value since the sample was bleached [54, 55].

- Internal-external consistency (IEU) criterion: IEU involves a comparison between dose rates obtained from the internal constituents of the sample (such as grains) and those obtained from the external environment (such as the sediment matrix). The consistency between these measurements can provide indications of age [58].

- Exponential exposure model (EED): The EED employs an exponential function to represent the connection between dose rate and time. This model is fitted to the observed data to obtain an age estimate[59].

The most recent line of research on age models proposed a Bayesian analysis. [60].

It is important to note that the choice of age model depends on the specific characteristics of the sample, such as its degree of bleaching, grain-to-grain variability, and heterogeneity of the dose distribution. Neglecting this step could potentially impact the precision of equivalent dose measurements. Other characteristics to be taken into account are well illustrated by the meticulous work of Urbanova and Guibert [53]. In this work, the authors analyse mortars of different nature and degree of bleaching, concluding that "well-bleached samples can be reliably dated using the Central Age Model (CAM) for archaeological dose calculations." Moreover, poorly bleached samples are highly influenced by heterogeneous microdosimetry for which a universal method of archaeological dose assessment has not yet been found.

The most consistent problem in OSL dating remains the degree of bleaching and how to understand its extent. One way to examine the degree of bleaching is to draw a distribution of the ED value. Among the parameters characterising the distribution there is the overdispersion. This term denotes the unexplained variance between the data [61]. For an unbleached sample, this value systematically exceeds 100%, whereas for well bleached samples it is below 50%. Furthermore, a Gaussian, symmetrical distribution becomes indicative of a good degree of bleaching of the grains [53].
Nowadays, scientific community has developed free software package to use the same age models (`http://CRAN.R-project.org/package=Luminescence`). The application of age models offer a novel way to depict distributions of Equivalent Dose and establish age-related parameters. The discussion on obtained parametres will focus specifically on the Central Age Model (CAM) and the Minumum Age Model (MAM).
This two methods are the most widespread. Starting with the Central Age Model (CAM), the Equivalent Dose values are subjected to logarithmic transformation. This yields to two key parameters: the geometric mean of the distribution, referred to as the central dose (δ), and the overdispersion value (σ). In cases where $\sigma > 0$, it suggests insufficient bleaching of the sample prior to deposition. This could indicate a mixing of sedimentary layers with distinct ages.
Moving to the Minimum Age Model (MAM), it is employed when dealing with samples known not to have received adequate light exposure to fully reset luminescence signals in all grains before final deposition. In MAM, true Equivalent Dose values undergo logarithmic transformation. Additionally, values are drawn from a truncated normal distribution, where the lower truncation point (γ) corresponds to the mean of the true population of completely bleached grains. MAM involves four essential parameters:

The minimum dose (γ), which signifies the lowest age for the deposit.

The proportion (p) of grains/aliquots in the ED distribution that contribute to the minimum age.

The mean (μ) and standard deviation (σ) of the truncated normal distribution, from which the log-transformed ED values are inferred.

These models provide valuable insights into the age estimation process, each tailored to specific sample characteristics and conditions.

4.3 Deconvolution analysis

As previously explained in section 4.1, the process of deconvolution allows the isolation of each component present in the OSL curve. The existence of numerous electron trap types that respond to light in quartz has been extensively documented in previous studies [19, 62]. When the assumption of first-order kinetics (with no re-trapping) is made, the Optical Stimulated Luminescence (OSL) response, can be expressed as the aggregate of n exponential component [4, 23, 25].

$$I(t) = \sum_{i=1}^{n} I_i(t) \tag{4.1}$$

It becomes possible to choose the component that has the qualities needed for dosimetric dating applications, namely, the fast component (OSL_f). The OSL_f exhibits sensitivity to light and maintains sufficient thermal stability to be present over geological timescales.
Even with recent advancements in instrumentation and in the SAR protocol use, which have led to the inclusion of deconvolution analysis software, deconvolution remains not utilized in routine SAR applications. There is currently a lack of a universally applicable, processing-independent solution for deconvolving OSL decay curves. The main difficulty with this target is the relatively low dating accuracy encountered when employing deconvolution for fast component extraction, which presents the main challenges in extracting this component [56].
Various approaches have been explored, highlighting the enhancement in dating reliability when isolating the OSL_f component from the others [63–66]. These studies employ advanced mathematical processing software to facilitate the extraction process, utilizing raw curve data points to refine Equivalent Dose calculations.
Notably, Sheng's investigation reveals improved results, even in cases where total OSL calculations are applied to samples acknowledged to lack adequate bleaching [63]. The use of using MATLAB as a tool for fast component ex-

traction is proposed, while other researchers opt for commercial software solutions like Excel [67].
Isolating solely the initial signal component presents a non-trivial challenge, given that the medium component (OSL_m) can also influence the seconds of the initial signal, thereby cause variation in the accuracy of sample dating [21]. It is worth noting that the OSL signal within the initial 0.1 seconds is, in fact, a composite signal comprising approximately 85% of the fast OSL component, with a variable minor contribution of up to 15% from other components. This percentage fluctuates depending on the specific characteristics and statistical properties of the component itself, as highlighted by Kitis in a preliminary study in 2011 [68].
Disregarding the presence of these additional components certainly leads to inaccurate age estimation [69].

For the analysis of OSL decay curves, a standard practice is to deconvolve these curves, considering the three-component. All the components are categorized based on their recombination lifetimes (τ) [19]. When considering first-order kinetics, the equation 4.1 applies.
However, considering a general order kinetics the parameters under analysis are different [4]. In the deconvolution process, one must validate the following fitting parameters within the presented formula:

$$I(t) = I_0 \left[1 + (b-1)\frac{t}{\tau}\right]^{-\frac{b}{b-1}} \tag{4.2}$$

Where:

- I_0, the highest intensity of the OSL component.
- τ, the recombination lifetime for each OSL component.
- b, the kinetic order.

This relationship, crucial for OSL deconvolution, is well-established in the work of Kitis and Pagonis[64].
Setting b to 1.0001 in 4.2 expression indicates first-order kinetics, and this expression remains applicable. Nevertheless, first-order kinetics predominantly governs the behavior of quartz.

To assess the goodness of the deconvolution fitting, verification can be achieved through the utilization of the Figure Of Merit (FOM). This method was proposed by Balian and Eddy in 1977 [70] and can be described by the following equation 4.3:

$$FOM = \sum_{i} \frac{|Y_{\text{Exper}} - Y_{\text{Fit}}|}{A} \tag{4.3}$$

Where i is the number of event considered. This method involves considering Y_{Fit} as the fitting glow curve, Y_{Exper} as the experimental glow curve, and A as the area under the fitted glow curve. Since the FOM is calculated according to the area under the curve, it is easy to compare the fit of different glow curves. Generally, fits are considered good when the FOM is just a few percent.
Besides FOM, the quality of fit is often indicated by various other parameters, like the sum of squares (weighted or unweighted) between experimental and fitted values or the F-ratio [71, 72]. The software programme Microsoft Excel, with theSolver utility add-in, was used for all curve fittings [67].

4.4 Selection of OSL decay curves: Residual Distribution Analysis

It has become increasingly evident that the key factor for accurate dating in optically stimulated luminescence (OSL) is the presence of a good fast component. In fact, an optimal OSL curve is characterized by the dominance of intense and steep fast OSL signals. The greater the extent to which these characteristics are present in the curve, the higher the precision is achieve in dating and dosimetry. This holds true when a signal predominantly comprised of the fast OSL component is generated, indicating an intensity that diminishes to less than 1% of the initial signal (I_0) after only a few tens of stimulation cycles [4].
Nevertheless, a substantial portion of OSL decay curves lacks these critical features. This deficiency is particularly evident in OSL curves obtained from samples with low sensitivity and/or inadequate bleaching, often attributed to thermal history or a low accumulated dose.

Exploring a method to effectively choose OSL curves with specific desired characteristics presents an intriguing challenge for signal selection.
One approach worth investigating involves the implementation of a selection criteria protocol centred around Residual Distribution Analysis (RDA) of natural OSL signals.
RDA is a statistical technique that not only is applicable on the fundamental physical processes underlying OSL but is also to various other experimental measurements. In this analysis process, a given data set is examined. By computing the difference between each successive data point and the one preceding it, thereby generating a series of values referred to as "residuals". These residuals represent the deviations or variances between consecutive data points. Subsequently, all these residuals are collected, organized, and displayed in the form of a histogram. This histogram provides a representation of the frequency distribution of the residuals, highlighting the patterns and characteristics of the distribution.

Two parameters for visualizing the trend of the curve are *skewness* and *kurtosis*. These parameters are widely utilized in the analysis of residual distribution and offer a means to describe the geometric attributes of distribution curves [73–77].
Skewness, the first of these parameters, serves as an indicator of distribution symmetry. It quantifies the extent to which a distribution departs from perfect symmetry. For any given distribution of a random variable X, skewness can be precisely defined as the standardized third moment [74, 78]. This parameter provides valuable insights into the shape and orientation of the distribution, aiding in the identification of potential deviations from symmetry that may have significance in the context of OSL curve selection and analysis.

$$\mu_3 = E\left[\left(\frac{X-\mu}{\sigma}\right)^3\right] = \frac{\mu^3}{\sigma^3} = \frac{E\left[X-\mu\right]}{\left(E\left[(X-\mu)^2\right]\right)^{3/2}} = \frac{k_3}{k_2^{3/2}} \tag{4.4}$$

In this equation:
- μ_3 represents the third central moment.
- E denotes the expectation operator.
- X is the random variable.
- μ represents the mean of the random variable X.
- σ represents the standard deviation of the random variable X.

- k_3 and k_2 are the third and second cumulants, respectively.
This equation shows the relationship between the central moments and cumulants of a random variable.

Kurtosis, on the other hand, delves into the shape-related aspects of a distribution. It serves as an indicator of how tightly or narrowly the data is grouped within the distribution. This is a valuable metric for the measure of the potential noise in a single OSL measurement. When kurtosis values are high, they suggest that there are probably no elements in an aliquot that could introduce instability into the signal. One such element might be an active trace element that can interrupt dose accumulation or prevent effective bleaching.
Mathematically, kurtosis is defined as the fourth standardized moment [74, 78]:

$$Kurt[X] = E\left[\left(\frac{X-\mu}{\sigma}\right)^4\right] = \frac{E\left[(X-\mu)^4\right]}{(E[(X-\mu)^2])^2} = \frac{\mu_4}{\sigma^4} \tag{4.5}$$

In this equation:
- μ_4 represents the fourth central moment.
- σ represents the standard deviation.
These statistical parameters are employed to identify inaccuracies or anomalies within the data. The process of defining skewness and kurtosis as outlined above ensures that the available OSL signals faithfully represent essential information, without being influenced by potential anomalies or errors.
Essentially, the integration of information derived from the skewness and kurtosis of the residual distribution can contribute to the refinement and enhancement of OSL data interpretation.
The calculation of the residual is obtained like the following equation 4.6:

$$y_{RDA} = a_{n+1} - a_n \rightarrow n < +\infty, a \in \mathbb{R} \tag{4.6}$$

where a indicates an individual data point within a mathematical series, representing a specific point in the dataset. "n" denotes the total count of observations present in the dataset, while the "residual value" refers to the difference between two successive data points, a_n and a_{n+1}.

$$n = \sum_{i=1}^{k} m_i \tag{4.7}$$

Subsequently, equation 4.7 is employed for the purpose of generating the data required for constructing a histogram. Specifically, the function m_i tabulates the count of observations distributed among individual, disjoint categories or bins, where "n" represents the total number of observations, and "k" denotes the overall count of bins. In the context of a perfect Gaussian distribution, which signifies a purely stochastic and random phenomenon, the skewness assumes a value of zero, while kurtosis settles at 3 [75, 76]. As both of these statistical parameters increase, they denote a shift in the distribution towards lower values of the variable, implying a greater influence of deterministic factors.
To facilitate a comparative analysis, figure 4.1 illustrates the Residual Distribution Analysis (RDA) for two distinct OSL decay curves: (a) one predominantly characterized by a rapid OSL component and (b) its exact opposite, noisy and unreadable. It's important to note that the characteristics of these presented curves were generated through simulation.

Assuming an OSL signal that decays very fast and is dominated by the fast OSL component, this is the ideal OSL decay curve. When the residuals associated with this curve are analysed, the resulting distribution show significant skewness and kurtosis values that exceed those associated with a random event. Conversely, in instances of an OSL signal characterized by its flat nature and unsuitability for dating purposes, the residual distribution takes on a symmetrical form closely resembling a Gaussian distribution [79].

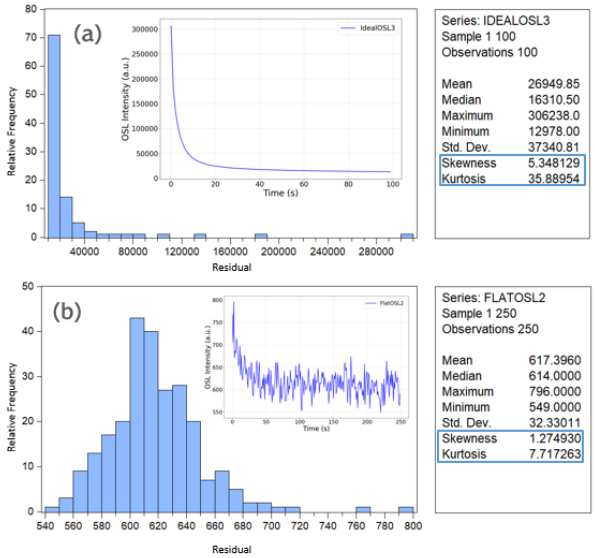

Figure 4.1: RDA histogram result for two distinct simulated OSL decay curves. The first curve (a) is primarily characterized by a fast OSL component, while the second curve (b) exhibits noisy and flat behaviour. In each figure, skewness and kurtosis values are shown in the respective table.

5 Sample's location

5.1 Zairo Theatre

The city of Padua stands at the confluence of two rivers, the Brenta and Bacchiglione. A huge theater with a diameter of about 114 meters stood in the Roman city. The theater is reported by historical sources to have been built during the 1st century AD when the city was known as *Patavium*. Few remains of the building, also known as Zairo, from the Latin *Satiro*, remain below the present urban level of Padua's central square, Prato della Valle. Indeed, materials from the theater have been reused over the centuries for other constructions. Abandoned for centuries, in 1775 a project was started to restore the now marshy area of the former theater. The drainage brought total coverage of the site and built the two canals that now stand in the square. It was necessary to wait until 2017, when an intensive excavation campaign promoted by the University of Padua, under the surpervision of Prof. Bonetto revealed the remains of the theater [80]. Among these remains, the mortars of the surviving radial walls could be taken. The samples under study in this thesis will be three: CPM_84, CPM_119 and CCM_7,
After sampling, an intensive analysis campaign was conducted at the Department of Geosciences of the University of Padua. An XRPD analysis led to the recognition of common features between samples CPM_84 and CPM_119. Both samples have an extremely pure calcic binder, to which two distinct aggregate assortments were incorporated. The primary category of aggregate consists of fine alluvial sand that includes quartz, carbonate clasts, and other components characteristic of river sands in the region. The secondary form of aggregate is characterized by tiny silica-rich clasts of volcanic origin. Subsequently, these clasts triggered a pozzolanic reaction within the compound.

Despite the complete reaction and small, sand-like size, their presence is undetectable within thin sections, but can be detected by SEM analysis. The existence of hydrated magnesium phases serves to substantiate this ongoing reaction.
In contrast, the sample, *CCM_7*, has a roughly rudimentary composition that includes a lime-based binder and an inert aggregate produced from local alluvial sands and a refined component of natural pozzolan, promoting a hydraulic reaction. To this underlying mixture are added black clasts of volcanic origin, which are distinguished by an increased content of glassy material and a larger grain size than the previous fraction.

5.2 Cannero Castle

The Cannero Castle, also known as Borromeo's Castle, are situated on a small island located 300 meters away from the shoreline of Lake Maggiore in the northern region of Italy. The earliest records of their construction date back to the year 1400. Historical records reported that the Mazzardi family constructed their castle with defensive intentions. In the years 1414-1415, the castle was overtaken by a contingent of soldiers dispatched by Filippo Maria Visconti, the Duke of Milan. Subsequent documents reveal that the Borromeo family were granted the ruins of the castle. The present structure, referred to as "Rocca Vitaliana," was erected in a short period of time, spanning from 1519 to 1521. Occupied until 1700, the stronghold was subsequently abandoned and utilized as a shelter for fishermen. The palimpsest of succession of phases is clearly visible in the structure of the castle itself, which is divided into 3 main courtyards (See figure 5.1)
The site of the Cannero Castle has been the subject of a radiocarbon dating campaign on mortars, conducted by the Department of Geosciences at the University of Padua [81]. During the 2016-2017 research campaign, the sampled mortars underwent extensive characterization. The analyses revealed the presence of minerals resulting from hydraulic reaction processes, indicative of the pozzolanic reaction between lime and clay in ancient mortar [82, 83].
Drawing from observations made by Ricci et al., it is apparent that the matrix displays heterogeneity with uniformly dispersed aggregates, and the mineralogical composition corresponds to the local rock formations.

Figure 5.1: Cannero Castle samples position (Image courtesy of `https://www.bmsprogetti.it/projects/cannero-castles/`), location information by [81]

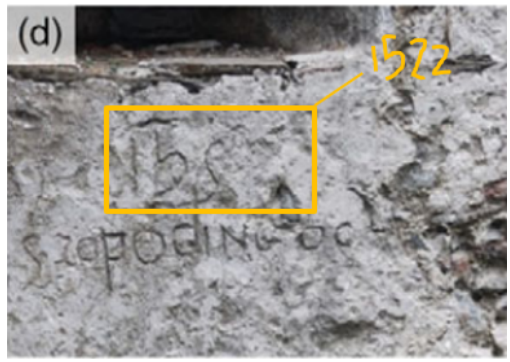

Figure 5.2: MM16 graffiti with 1522 inscription (Photo from Ricci et.al article [81])

The primary focus of the initial research campaigns was to comprehend and distinguish the different phases of construction. This study seeks to reinforce the initial findings acquired by Ricci et al [81].
Two of the analysed samples originate from distinct points within the western courtyard (PM12 and PM15). In this area, archaeological excavations were unable to definitively establish the chronological age of the various structures. Conversely, the sample MM16 is located in proximity to a graffiti inscription that denotes the year of the structure's construction (1522 AD).

5.3 Sarno bath - Pompeii

The so-called Sarno bath is a perfect example of multi-storied building [84]. Sarno Bath are a large Roman spa located in the southern part of the ancient city (Regio VII, insula 2), on the edge of the volcanic plateau on which Pompeii was built. Bernardi and Busana suggest that Insula 2 was already settled during 6th century BC – 3th century BC, and then, in the late republican age (2nd-1st century BC). The area was shaped by the erection of a large number of domus [85]. The ground floor was accessible from the city streets, and consisted of three main units with independent entrances and connected to each other [86]. All samples involved in this study were taken from the ground floor. (see figure 5.3)
In the last decade of the 1800s, all levels of the Sarno complex were brought to light. It was only during the nineteenth and twentieth centuries that restoration activities, not fully documented, were carried out. More recent investigations into the Sarno Bath have been carried out by an interdisciplinary team from the University of Padua since 2016. They continued until 2019 and led to the recognition of different building phases [86–88]. The research campaign establishes a terminus post quem for the construction of the last phase of the domus during the Augustan age (late 1st century BC - early 1st century AD). The samples involved have been analysed here to understand the phases before this one.
Recently, Dilaria et al. were able to study the samples that were involved in this study from a mineralogical point of view. It was therefore possible to divide the samples into different groups. The samples involved in this study are represented by group 1a (M255, M261, M266), group 1b (M256) and group 2b (M245). All samples in the first group are mineralogically characterised by the presence of leucite and leucite-rich rocks.
The presence of leucite in the mortars of Pompeii is a sign of the use of eruptive products in their preparation. This may lead to the conclusion that the mortars of this group are definitely dated after 79 AD. A more recent study decreases the interval by defining the presence of leucite as a sign of restorations that took place after 1631 AD [89].
The proximity and similarity of the group 2 and M245 mortars indicates that they are related to a single construction episode involving only part of the

Figure 5.3: Sarno Bath first floor, with sample location [86]

floor. It has been proposed that it was related to the restoration following the earthquake in Pompeii in AD 63 [86].

5.4 Capiate site

Capiate is a small settlement situated in the southern part of Olginate and located 10 kilometers away from Lecco. It has held a strategic position along the Adda River since the time of the Romans. This geographical feature likely contributed to the Capiate formation.
Throughout its history, Capiate has been a witness to significant historical events. One notable was the "Battle of the Adda" in 490 AD, where Theodoric, the Gothic king, fought against Odoacer, the barbarian general who had ended the Western Roman Empire 14 years earlier. The Lecco territories, even Capiate transitioned from Byzantine control to becoming Lombard possessions between 580 AD and 588 AD. In 745 AD, there is documented evidence that the village was a tributary casale. This record also marks the earliest mention of the Village's name, "Clapiate," derived from the second Lombard king, Clep. Capiate became a monastic feud under the authority of the Sant'Ambrogio Monastery in Milan during the Franks. This affiliation was fundamental in

its development, leading to enhancements productivity, particularly in vineyards. The Basilica of San Nazaro, possibly built prior to the monastery, played a central role in the religious life of the surrounding communities for many centuries. Remains of this medieval religious structure are still visible today.
From 1310 AD until the present, the Capiate property then passed from noble family to noble family, often led to dispose of the property once it fell into disgrace. The families settled into palaces with a characteristic tower, a sign of the passing of time. Between the 9th-16th centuries, defensive structures were raised systematically during the Visconti and Sforza dynasties.
In 1928 AD, the municipality of Capiate, established in 1632 AD, was merged with Olginate. While the complete structures may not be entirely visible today, the Monastery palace and the elegant Villa stand as tangible reminders of Capiate's role as a key player in multiple historical phases [90].

Two structures from the Capiate site underwent thorough analysis: the tower and an ancient church in the court.
In-depth investigations into the region start in 1980, persisted through 1999, and achieved in a significant campaign from 2004 to 2007. The principal work focused primarily on the iconic tower, the structure that give the welcome upon the entrance into the village. This tower, standing 13 meters in height with a base measuring 12 meters by 9 meters, and demonstrate a history of considerable complexity. Illustrated in figure 5.4 are both the present-day photos of the tower and the proposed stratifications, offering a sight into its evolution over time. Despite experiencing partial remodeling during the years, these modifications appear to have left the tower's core intact. What remains unequivocal is that the restoration undertaken in the 1990s, which has included the incorporation of consolidation mortars to address deteriorated or lost joints.
However, a minimum of 10 distinct phases have been delineated, spanning from the Roman era to the 20th century. The size of the masonry structures up to the third phase suggests that they even come from distant areas or at any rate an obvious building effort. The close proximity to the Adda River potentially facilitated transportation.
Additionally, the arches subjected to analysis (see figure 5.4c), particularly those from phase II (late antiquity), were discovered to be entirely covered

Figure 5.4: The Capiate's Tower along with the hypotized phase structures

in layers of lime mortar. The sand utilized, presumably extracted from the Adda River, exhibited an exceptionally fine grain size. The consistency of the mortar proved to be incredibly tenacious [90].

Regarding the church, there is information about its existence found *"fundata in loco qui dicitur Clepiate"*. This fact eliminates any uncertainty surrounding the presence of a church there by the late 9th century. The alteration in the court's structure means that only the apse is currently visible from the original church. Previous analyses have recognized distinct phases, all within the texture and finish characteristic of the 12th century or earlier. The feature that aids in dating the structure from which the sample was obtained to the 10th-11th century is its style. Specifically, the horseshoe-shaped apse and the centrally positioned external structure gives a chronological placement in the Carolingian era.
Two additional factors provide support for this timeframe. First, the discovery of an early medieval capital, and second, radiocarbon analysis conducted on the constructions and burials. The latter yielded a probable chronology range of 760-980 AD with a confidence level of 92.2%. To sum up, the significance of the Capiate church lies in its contribution to the ongoing debate concerning the dating of structures between the High Middle Ages and the initial appearances of Romanesque architecture [90].

Among the collected samples, four were selected for detailed study, fo-

cusing on those with the most reliable dating information. Specifically, two samples, designated as CT2 and CT3, were extracted from the northwestern corner of the tower. CT2 is strongly associated with a dating range that places it in the first half of the 5th century, while CT3 is estimated to date back to around 570 AD.
An additional sample, CT8, was also from the tower but from the internal arch of the northern perimeter. CT8 is presumed to be even older, certainly predating CT2 and CT3, possibly tracing its origins back to the 2nd century.
From the ancient church, a single sample labelled as CA1 was analysed. This sample was obtained from a buried section of the apse. Conclusions drawn from the analysis suggest that the construction of this particular structure was completed between the 10th and 11th centuries.

6 Handling, protocols and equipment

6.1 Equivalent Dose assessment

The established protocol for mortar preparation and equivalent dose measurement, was rigorously applied [45, 46]. The preparation phase followed Fleming's technique known as the inclusion method [17].
Initially, the top 3-4 mm of the mortar was removed using sandpaper or a file. Subsequently, the treatments previously discussed in section 2.2 were executed. Notably, for mortar treatment, a day-long treatment with H_2O_2 (10%) was employed to eliminate organic matter, followed by a 6-hour immersion in HCl to dissolve carbonates. The feldspathic component was targeted with an application of HF (48%) for approximately 40 minutes. Each acid treatment was followed by thorough washing to restore neutral pH. The complete dissolution of the feldspathic component was validated through IRSL stimulation utilizing the Risø TL-DA-20 reader (at 830 ± 10 nm; maintaining a constant stimulation power of 360 mW/cm^2). An IR signal exceeding 5% was considered acceptable.
The amount of quartz grains obtained is variable.
To determine the equivalent dose, a Single Aliquot Regenerative Dose (SAR) protocol, as designed by Murray and Wintle (2000) [26], was applied (refer to section 2.3). The first measurements were executed using a Multigrain protocol. Grains were fixed onto a 10-mm-diameter stainless steel disk using silicone oil, with an approximately 3 mm covered diameter area, accounting for almost 300 grains. OSL signals were gained using Risø TL-DA-20 readers, equipped with a bialkali photomultiplier tube (EMI 9235QB). OSL emission was detected through a Hoya 7.5 mm U340 optical filter [91, 92].
Before proceeding, a dose recovery test was performed to assess the accuracy

and reliability of the dating procedures. Customized pre-heat, test dose, and OSL measurement time were chosen for each individual sample, while each OSL measurement was conducted at 125°C.
Upon analyzing the Multigrain curves, the decision was to persist with this measurement approach. Although the single-grain protocol is acknowledged as the most effective for dating [51], it was ruled out due to the already faint signal detected in the multigrain aliquots. The single-grain tests did not yield an adequate number of acceptable aliquots for all the sample except one.

Risø reader system

A Risø Reader model TA-20 instrument is used for conducting Thermoluminescence (TL) and Optical Stimulated Luminescence (OSL) measurements. This sophisticated setup features a rotating carousel with 48 individual sample slot, each rotation allowing sample measurement on the individual slot. Within this apparatus, sample heating from ambient to 700°C is facilitated by a thermocouple. For irradiation, a beta source ($^{90}Sr/^{90}Y$) is employed. The source give a dose equal to 0.11 Gy.
Optical stimulation is achieved through interchangeable laser sources. The sample, mounted on an aluminum disc, is positioned within a measurement chamber with a controlled nitrogen flow. Subsequently, the sample is elevated to the measurement position through slots in the carousel by a raised plate, which also serves as a heating element. At this measurement point, both thermal and optical stimulation can be performed. Thermal stimulation is done by gradually increasing the temperature of the heating strip, while optical stimulation is delivered via different light sources focused onto the sample's location. The emitted luminescence is captured by the light detection system. The detection mechanism comprises the detector, a photomultiplier tube (PMT) along with suitable filters. The filters both serve the function of shielding the photomultiplier tube from scattered light from stimulating sources and define a detection window. The photomultiplier tube integrated into the Risø Reader instrument has a peak efficiency around 400 nm, optimizing luminescence detection for both quartz and feldspar. Quartz has strong emission centered at 365 nm (in the near UV), while feldspars have emission centered at 410 nm (violet).

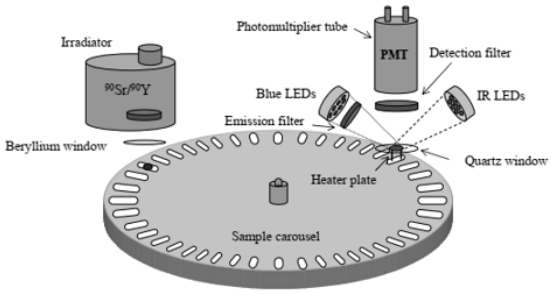

Figure 6.1: Risø measurement system

Directly beneath the PMT, the heating element and elevation system are positioned, effectively conducting sample heating and positioning it for measurement. This heating element, constructed from a high-strength alloy, is managed by a thermocouple for precise control. Operating within a range of 0.1 to 30 K/s, the system is capable of linearly heating the sample up to 700°C. Subsequent cooling is accomplished by a nitrogen flow, safeguarding the element from oxidation during high-temperature procedures. Notably, light-emitting diodes (LEDs) are employed for optical stimulation, offering various advantages including inexpensive, short response times, and are electronically controlled. This electronic control facilitates intensity adjustment and modulation according to the stimulation duration. The LED array is situated between the heating element and the photomultiplier tube, with distance of approximately 20 mm from the diodes to the sample [92].

6.2 Dose rate evaluation

The concentrations of ^{238}U and ^{232}Th were determined through alpha counting using ZnS(Ag) scintillator disks, assuming a Th/U concentration ratio of 3.16 [3]. The value just described is a valid approximation for ceramic bodies. The value is to be regarded as an assumption.
Alpha counting was employed to estimate the alpha radiation's contribution to the annual dose. Approximately 500 mg of the sample was finely grounded

in a mortar, and the resulting powder was spread over a zinc sulfide scintillator screen. Scintillation signals produced by interactions with alpha particles emitted from the sample were detected by a photomultiplier for almost 24 hours. The number of alpha particles emitted per minute (cpm) was computed from these counts. This enabled the determination of alpha-emitting radionuclide concentrations (^{232}Th, ^{238}U, and ^{235}U) within the sample.

Using the radionuclide concentrations, the specific activity was calculated using the equation:

$$A_{Sp} = \lambda \cdot \frac{c}{\mathcal{A}} \cdot N_A \tag{6.1}$$

Here, λ represents the decay constant, c is the concentration (g/kg), $\mathcal{A}$ is the mass number, and N_A is Avogadro's number. With this information, the annual alpha dose from individual radionuclides could be computed by multiplying their specific activity with the corresponding annual dose coefficients. By summing the alpha doses from the three alpha-emitting radionuclides, the annual absorbed alpha dose for the sample was derived. This value, calculated for the dry sample, was subsequently adjusted for moisture using the equation;

$$D = \frac{D_{\alpha,dry}}{1 + 1.5WF} \tag{6.2}$$

where WF is the water content estimate [3]. Please note, as it is an inclusion method, the a-factor is not calculated.

From the alpha counts, the beta dose originating from thorium and uranium radioisotopes was also determined. By using the specific activity of these radionuclides and the annual dose coefficients, the annual alpha and beta doses resulting from the presence of thorium and uranium in the samples were computed, while accounting for the attenuation of beta particles [93].

For assessing dose rates, the ^{40}K content was deduced from the total potassium concentration measured using flame photometry. The chemical preparation of potassium measurement samples followed these steps:

- Accurately weigh 500 mg of the sample.
- Place the sample in a Teflon crucible and add 5 ml of 60% perchloric acid ($HClO_4$) and 15 to 20 ml of 40% hydrofluoric acid (HF).

- Heat the crucible on a graphite plate at around 50-60°C.
- Evaporate the solution until the first white vapors appear.
- Nearly dry the solution.
- Add deionized water and 2.5 ml of 60 percent perchloric acid, and then heat.

If the solution isn't clear, repeat the perchloric acid treatment. If it's clear, bring the solution to a volume of 250 ml with deionized water. To prepare the reading samples, 10 ml of solution was taken and mixed with 10 ml of lithium sulfate (Li_2SO_4), then brought to volume in a 100 ml flask. Flame photometry was used to measure the sample solutions, and the individual potassium concentrations were determined by comparison with a 4% potassium standard. Given the natural abundance of potassium-40 at 0.0117%, the concentration of radioactive potassium in the samples could be determined. With the concentration, the specific activity of potassium was calculated, similar to the previous steps for thorium and uranium. This value was then multiplied by the annual dose coefficients to measure the contribution of potassium-40 to the annual beta dose. The total beta dose was adjusted for moisture as well:

$$D = \frac{D_{\beta,dry}}{1 + 1.25WF} \tag{6.3}$$

The annual gamma dose absorbed by the sample originated from environmental radioactivity present in the accompanying soils. Correction for moisture was applied:

$$D = \frac{D_{\gamma,dry}}{1 + 1.14WF} \tag{6.4}$$

The external gamma contribution, primarily derived from the radioactivity of a 30-cm-diameter sphere centered on the sampling point [3], was determined based on the radioactivity concentrations of the mortars and the surrounding environment [94], using the infinite matrix approximation with updated conversion factors [95]. The contribution of cosmic rays to the final dose rate was factored in based on Prescott and Hutton [96].

7 Result and discussion

In this thesis, mortars from sites described in chapter 5 were dated.
One of the aim of this study was to validate the dating procedures for a set of samples with known ages using the Optically Stimulated Luminescence (OSL) dating method. Two procedures of analysis are proposed to achieve

Location	Sample	Expected age
Zairo Theatre	CPM_84 CPM_119 CCM_7	I cent.
Cannero Castle	MM16	1525-1791
	PM12	1694-1919
	PM15	1409-1444
Sarno Bath	M245	I-II cent.
	M255 M256 M261 M266	XIX cent.
Capiate	CT2	400-450 AD
	CT3	570 AD
	CT8	II cent.
	CA1	X-XI cent

Table 7.1: Expected age for the samples

this result.
Classical analysis in the context of mortar dating refers to the methodologies traditionally employed within this field.
A schematic representation of this conventional approach is provided in the figure 7.1. It's important to note that the only exclusion criteria to these classical analyses are recycling ratio and recuperation values (in oval). While it will be defined as a *new path* the one that involving deconvolution analysis and

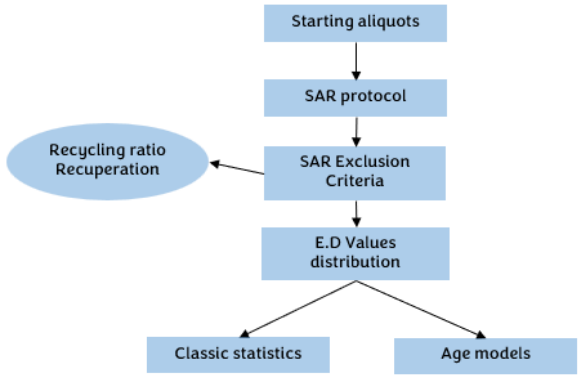

Figure 7.1: Classical path of OSL mortar dating, in the oval the exclusion criteria

Residual Distribution Analysis. The new path is indicated by the figure 7.2. In the diagram, classic protocols with the two exclusion tests are highlighted in a light blue. Meanwhile, the additional steps introduced through deconvolution are depicted in gray. On the other hand, the descriptive analysis of the residual analysis stands out distinctly in orange. Encircled within ovals, the exclusion criteria visually are represented.
As highlight in the chapter 4, the new path involves the establishment of additional selection and filtration criteria to supplement existing one, specifically the recycling ratio and recovery tests. The primary goal of this study is to systematically delve into and determine these criteria.

All laboratory protocols employed in this study were consistent with those previously established and applied by the LAMBDA (Laboratory of Dating and Archaeometry, University of Milan Bicocca) laboratories for other case studies [43, 45, 46].
The samples were subjected to OSL dating using the coarse-grained technique (size: 180-250 μm), with detailed procedures outlined in the section 6.1. The measurement were conducted following the Single Aliquot Regenerative (SAR) protocol. For grain analysis, the Multigrain (MG) method was

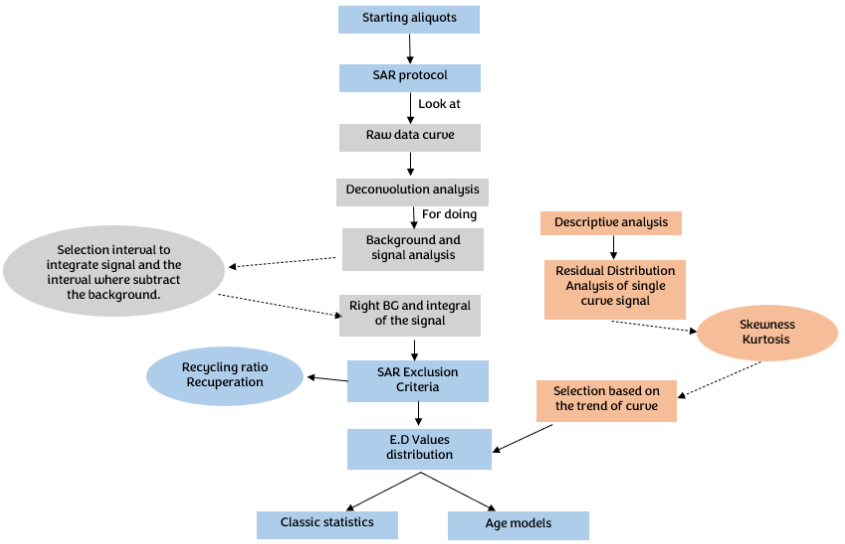

Figure 7.2: The new path proposed with the deconvolution analysis and the descriptive analysis.

employed. Notably, almost none of the samples exhibited an intense luminescence signal, making the application of the single-grain (SG) technique not suitable.

The aliquotes were prepared and misured as described in previous in 6.1 [61, 92]. SAR procedures used in this study are illustrated in figure 7.3. The doses given to the majority samples were 5.5 Gy, 11 Gy, and 16.5 Gy, different doses were choosen in the case of Capiate site. The recycling point corresponded to the value of the first imparted dose and was preceded by a zero-dose recovery test.

For preheating value, were selected temperatures based on the outcomes of the preheating plateau test. These temperatures exhibited a diverse range, spanning from 160°C to 260°C.

In the context of Test Dose, also varied from a minimum of 10 s of beta irradiation to 30s. Corresponding to 1.1 and 3.3 Gy.

The duration of the OSL measurement itself was contingent upon the individ-

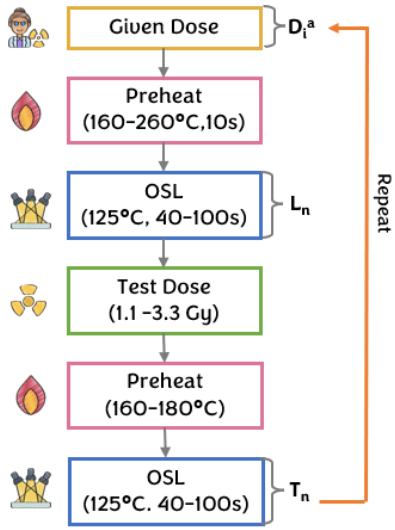

Figure 7.3: SAR protocol applied. Where a) i = 1–4 correspond to D_1 = 0 Gy (Natural), $D_2 - D_4$ Regenerative doses (5.5, 11 and 16.5, Gy), D_5= 0 Gy (Recuperation test), D_6= D_2 (Recycling point).

ual response of each sample, with options of either 40 seconds or 100 seconds employed to ensure accurate data collection. Several statistical methods were employed to calculate the equivalent dose (E.D.).
The term "classic statistic" will be used to denote the mean and the weighted mean. While, the age models are refereed to Central Age Model (CAM), and Minimum Age Model (MAM) (see paragraph 4.2) [54].

7.1 New path discussion

Deconvolution

Figure 7.4 shows a deconvoluted OSL decay curves. Notably, the majority of the raw analyzed curves exhibit a consistently low sensitivity. This phenomenon is hypothesized to be a consequence of the thermal history and origin of the quartz present in the mortar sample. Furthermore, the decay of these OSL signals displays a lack of steepness, particularly in the later stages

Location	Sample	Aliquotes	Preheat (°C)	OSL	Test Dose (Gy)	Cutheat (°C)
Zairo Theatre	CPM_84	49	260	125°C, 100s	1.1	180
	CPM_119	62	240	125°C, 100s	1.1	180
	CCM_7	27	240	125°C, 100s	3.3	180
Cannero Castle	MM16	40	160	125°C, 100s	2.2	160
	PM12	13	260	125°C, 100s	2.2	180
	PM15	36	180	125°C, 100s	3.3	160
Sarno Bath	M245	38	180	125°C, 40s	2.2	160
	M255	2	260	125°C, 40s	2.2	180
	M256	2	260	125°C, 40s	2.2	180
	M261	11	260	125°C, 100s	2.2	180
	M266	6	180	125°C, 40s	2.2	160
Capiate	CT2	48	200	125°C, 40s	2.2	180
	CT3	57	200	125°C, 40s	2.2	180
	CT8	54	200	125°C, 40s	2.2	180
	CA1	37	200	125°C, 40s	2.2	180

Table 7.2: SAR parameter for each sample, where cutheat is to be taken as the second preheat after the test dose

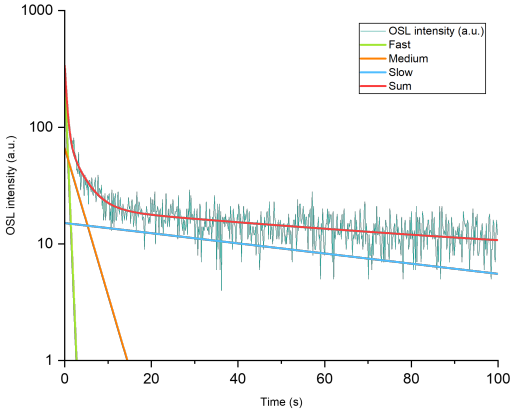

Figure 7.4: Examples of deconvolution analysis of OSL decay curves obtained in the framework of the SAR protocol applied to a general aliquot. In green is the tendency of OSL_f, in orange OSL_m, in Light blue OSL_s. In Red the sum of the three component. Note that the background is not rappresented, so it can justify the difference in the shape in slow component and the total sum at the end of the curve.

of stimulation, suggesting notable scattering, which is likely linked to the medium/low sensitivity of the signal. Almost all the signals in the curves have a medium/low signal sensitivity. This difficulty in reading the signal provides a further motivation for other methods of statistical analysis, which aims to overcome this limitation.

In this thesis, deconvolution analysis for two distinct samples was achieved: CPM_84 from the Zairo Theater and MM16 from the Cannero Castle site.
In each mortar samples, all three components were identified [19]. Subsequently, an analysis of kinetic parameters associated with these OSL components was conducted, allowing for the determination of the recombination lifetime (τ) and the order of kinetics (b). Fitting parameter errors were calculated based on the corresponding Figures Of Merit (FOM).
The results for parameter 'b' consistently fell below the threshold of 1.0001, thereby serving as a robust indicator of the first-order model hypothesis in quartz.
The recombination lifetime, denoted as τ, reflects the origin and history of quartz grains. The observed distribution patterns of τ clearly suggest a complex origin of the mineral. Furthermore, the parameter τ assumes a role in the analysis of OSL signals. It is used in the calculation of the photoionization cross section, represented as σ (in cm^{-2}), for each component, as per the equation below:

$$\sigma = \frac{1}{\tau\phi} \tag{7.1}$$

Here, ϕ represents the flux, measured in $cm^{-2}\ s^{-1}$. In the context of our OSL measurements, blue LEDs operating at a power output of 90% were employed, yielding a calculated flux of $1.9 \cdot 10^{17}$.
Traps with larger cross-section areas at the stimulation wavelength employed in measurements empty rapidly, giving rise to the fast decay component (OSL_f). While, traps with smaller cross sections contribute to the medium and slow decay components, (OSL_m) and (OSL_s), respectively [97].

In addition to parameters such as I_0, the deconvolution analysis provided intensity values for each OSL component. The ratio of each component's integral to the total OSL integral offered insights into the percentage contribution of each OSL component to the overall OSL signal. Consequently, the percent-

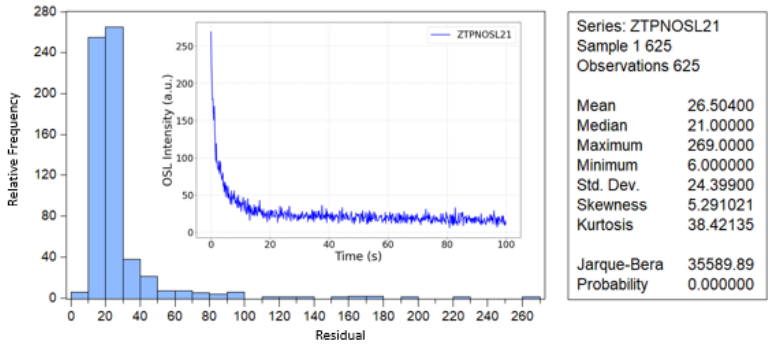

Figure 7.5: Residual Distribution Analysis of one natural OSL decay curve measured in the framework of the present study.

age presence of each component in each aliquot was revealed.
In scenarios characterized by bright OSL signals, where the fast OSL component predominated, this component contributed in excess of 50% to the overall OSL signal. The slow and medium components, alongside their corresponding background signal, constituted the remaining percentage, extending up to 100%. These findings suggested that, beyond the non-steep decay form, the OSL signal was not primarily shaped by the fast OSL component. It is worth noting that as regeneration doses increased, there was a slight shift towards an OSL signal that was more predominantly influenced by the fast component. The contribution of the background signal exhibited variations.

Skewness and kurtosis of natural OSL

Residual analysis was conducted for every individual natural Optically Stimulated Luminescence (NOSL) curve. This analysis leads to the examination of residuals, which is obtained with the equation 4.6. An illustrative representation of these residual distributions is depicted in the histogram shows in figure 7.5. It is important to emphasize that this distribution should be referred as a simulation applicable to the majority (>95%), of the measured natural OSL (NOSL) signals. For each of these residual distributions associated with NOSL, skewness and kurtosis, were computed using equations 4.4 and 4.5 respectively. The skewness and kurtosis values of the "flat" OSL decay curve, as depicted in figure 4.1, serve as the initial rejection thresholds for

the NOSL curves in current study.
Moreover, the skewness and kurtosis values of the ideal OSL decay curve could also be employed as reference values for selecting the most suitable natural OSL decay curves (see figure 4.1).
Thus further selection criteria were imposed. The Equivalent Dose (ED) was computed by excluding rates that yield skewness and kurtosis values falling outside specific intervals. For samples stimulated for 100s, the exclusion criteria for kurtosis was set to values outside the interval centered at 37.89, while for the skewness the threshold was centered at 5.35. These values are chosen based on the Skewness and Kurtosis results of a simulated curve shown in figure 4.1 For samples measured for 40 seconds, a skewness and kurtosis exclusion criterion of 2.14 and 15.15, respectively, was employed. The choice was made by observing a simulated OSL curve with all the desired characteristics. Skewness and Kurtosis values were taken as threshold. The associated uncertainties correspond to the Full Width at Half Maximum (FWHM) of the skewness and kurtosis distributions calculated for each sample.
Remarkably, it is observed that almost all aliquots falling within the skewness range pass both tests of the SAR protocol, specifically the recycling ratio and the recovery test. This observation highlight the utility of these two parameters as indicators of curve trends.
In addition, for the two samples analysed by deconvolution (CPM_84 and MM16), the unacceptable samples for skewness and kurtosis criteria had FOM values greater than 5%. This indicated that the natural OSL decay (NOSL) curves possessed an increased noise-to-signal ratio. After excluding all outliers, it will be shown how the ED and age values change using only the above acceptable rates varied.

In the upcoming sections, an examination will be conducted to assess the variations in Equivalent Dose (ED) values along the two paths: the classical one and the newly proposed path. Following the removal of outliers, an analysis will be presented illustrating the variation in both ED and age values when considering only the acceptable rates, as per the previously defined criteria.

7.2 Zairo Theatre

Three samples (CPM_84, CPM_119, and CCM_7) were collected from the Zairo theater located in Padua, Italy. These samples had varying weights, measuring 20.16 g, 185.27 g, and 208.68 g, respectively. The specific origin of these samples within the excavation site remained undisclosed. In conjunction with sample CPM_84, radioactivity measurements were recorded for a single brick. The table below provides details regarding the radioactive content, internal and external dose rates for mortar samples.

Sample	Water content (%)	^{238}U (ppm; ± 5%)	^{232}Th (ppm; ± 5%)	^{40}K (ppm; ± 3%)	Internal dose rate (mGy/y)	External dose rate (mGy/y)	Dose rate (mGy/y)
CPM_84	18	2.95	9.31	2.1	2.01	1.79	3.19 ±0.15
CPM_119	20	1.15	3.65	1.05	0.94	0.49	1.35 ± 0.07
CCM_7	19	2.46	7.78	1.63	1.61	0.93	2.68 ± 0.11

Table 7.3: radioactive content and dose rate of Zairo Theatre's mortar samples. Water contenent is only W. The dose rate is calculated with the parametres defined by Guerin et.al. [95]

CPM_84

Approximately 2.14 g of quartz was extracted from the sample, and a subsequent evaluation for feldspar contamination was conducted through IR stimulation on irradiated samples within the laboratory setting.

A total of forty-nine aliquots underwent analysis.
For what concerns the classic selection criteria, only nineteen aliquots pass the recycling test criteria (ranging between 0.9 and 1.1). The raw OSL curve trend was mostly non-noisy and characterized by good curve slope (figure 7.6 is an example).
Equivalent dose values were subsequently computed for both the entire set of aliquots and the subset that met the acceptance criteria. Various statistical parameters, including the mean, weighted mean, Central Age Model (CAM), and Minimum Age Model (MAM), were examined in this analysis.

Our results in the classic protocol indicated a different estimate of the expected age for most of the samples, regardless of the statistical model used to calculate the Equivalent Dose. This overestimation was attributed to incomplete bleaching of the quartz grains during the mixing and deposition processes. One evidence can be given by the non-Gaussian distributions of

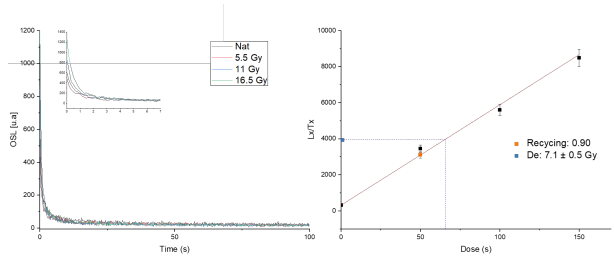

Figure 7.6: A signal and OSL growth values for a CPM_84 aliquot.

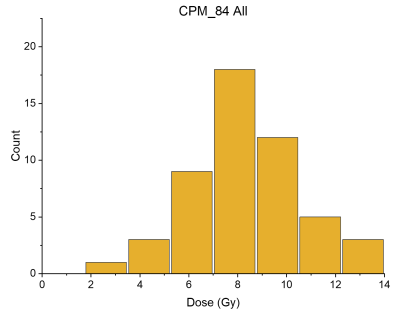

Figure 7.7: Equivalent Dose distribution for all aliquots of CPM_84

the Equivalent Dose values obtained. The distribution of the equivalent dose values is in figure 7.7. Notably, our results revealed a distinct estimation of the anticipated age for most samples, regardless of the statistical model applied for calculating Equivalent Dose. This overestimation was linked to inadequate bleaching of the quartz grains throughout the mixing and deposition phases. By calculating the dose rate for the sample, which is **3.19** $\pm$ **0.15** (mGy/y), it was possible to predict ages using the classical protocol. Only the values that passed the recycling and recuperation tests are shown for ease of understanding (see figure 7.8).

CPM_84 new path results

Figure 7.9 displays examples of deconvoluted OSL decay curves acquired during the analysis done for dating the Zairo Theater. Each plot corresponds to

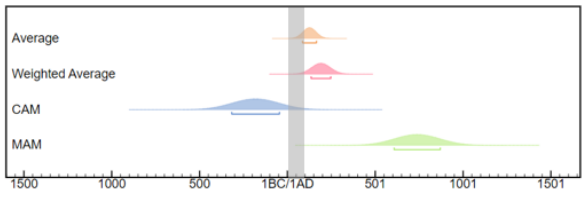

Classical Statistic	Equivalent Dose (ED) (Gy)	Age (Years)	Date
Average	6.04 ±0.12	2320 ± 630	350 AD ± 630
Weighted Average	5.83 ± 0.17	1830 ± 55	190 AD ±55
CAM	7.02 ± 0.43	2200 ± 130	180BC ± 130
MAM	4.09 ± 0.41	1255 ± 135	740 AD ± 135

Figure 7.8: CPM_84 sample age with exclusion critieria proposed within SAR protocol (recycling ratio and recuperation)for each statistical method used. In gray the assumed age period.

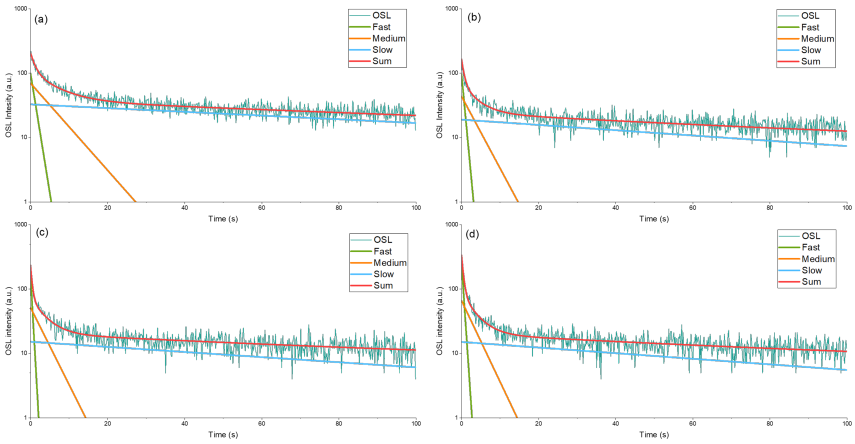

Figure 7.9: Deconvolution analysis of OSL decay curves in CPM_84, which were acquired within the context of the SAR protocol, using the same aliquot. These instances pertain to the following conditions: (a) natural dose, (b) first regenerative dose, (c) second regenerative dose, and (d) third regenerative dose.

a different regenerative dose in accordance with the SAR protocol. As previously discussed, that the majority of these observations relate to OSL signals characterized by generally low sensitivity and exhibit less steep decay patterns. Following deconvolution, information regarding the kinetic parameters of the OSL components, namely τ and b, was obtained. The Figures of

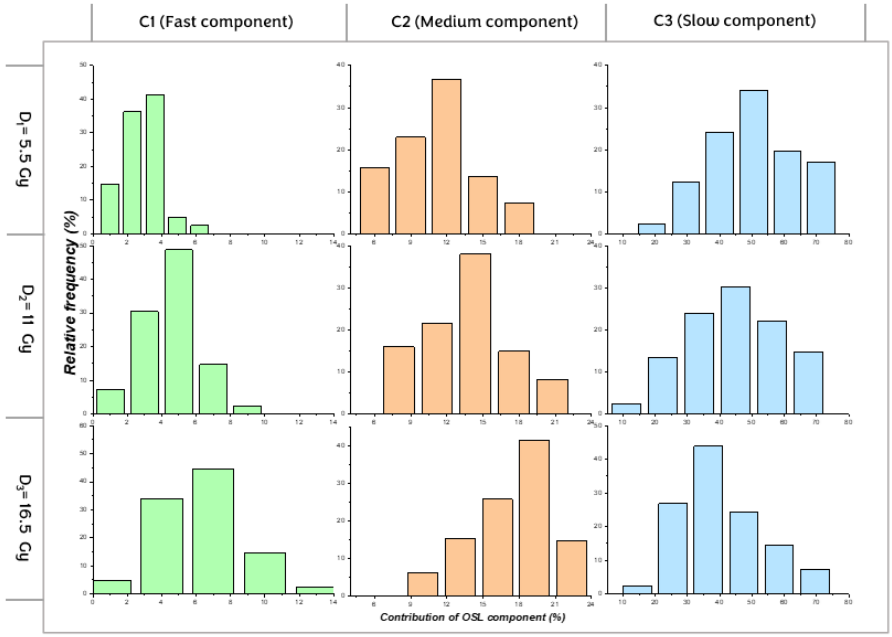

Figure 7.10: Histograms show the distribution of the percentage of the fast, medium, and slow OSL components for every regenerative dose within the SAR protocol framework. The graph correspond to the values acquired through deconvolution analysis for all parameters.

Merit (FOM) calculated for CPM_84 exhibited a range spanning from 3 to 9.5 %. This observed variability can be attributed to the considerable dispersion evident in the decay curves across all OSLs. Parameter b was set at 1.0001.
Furthermore, the deconvolution analysis provided insights into the percentage contributions of each OSL component to the overall measured OSL signal. Figure 7.10 illustrates the distribution of these component percentages for successive dose levels. The contribution of the OSL_f component to the total OSL signal fluctuates between 3 and 7%, as determined by the centroid of each distribution. In contrast, the corresponding values for the OSL_m component range from 9 to 15%, while the OSL_s component's contribution spans from 35 to 50%. Importantly, the maximum percentage contribution does not surpass 14% for the fast component and 24% for the medium component.
In cases characterized by bright OSL signals where the OSL_f component pre-

dominates, the contribution of the fast OSL component to the overall OSL signal exceeds 50%. The fast and medium components, along with the corresponding background signal, account for the remaining percentage up to 100%. These findings suggest that, apart from the non-steep decay pattern, the OSL signal is not primarily dominated by the contribution of the fast OSL component.
Notably, the contribution of the fast and medium OSL components indicates a slight shift towards an OSL signal more dominated by the fast component as regeneration doses increase. Finally, the contribution of the background signal varies from 4 to 9%, with the maximum value occurring at the lowest regeneration dose.

The discussion regarding the choice of an appropriate background region of interest was exclusive to the CPM_84 sample. Unlike the discussion for sample MM16, this particular sample allowed for the completion of the deconvolution analysis with non-elevated Figures of Merit (FOM) values. It is conjectured that the percentage contributions of both the fast and medium OSL components can serve as indicators for the selection of the appropriate background region, especially in cases where deconvolution is not applied.
Drawing upon the ideal scenario of an OSL decay curve dominated by decaying fast OSL component, the corresponding percentage contributions typically exceed 60% for the fast OSL component and approximately 20% for both the slow and medium OSL components [64, 68]. In such cases, it is advisable to subtract the late background when analysing these OSL decay curves. However, in studies where the OSL decay curves lack dominance by a fast OSL component, as evident in this particular case, the contribution of the medium component to the early seconds of decay becomes significant. Consequently, early background subtraction is recommended.
For this sample, three different ED distributions were compared for the choice: (a) the weighted average of EDs determined using the full integral of the fast OSL components after deconvolution; (b) the weighted average of EDs calculated using the first 10 seconds of OSL signal stimulation minus the early background; and (c) similar to case (b) but minus the late background [56, 98]. In all three cases, only the aliquots that met all the imposed selection criteria (SAR, Skewness, and Kurtosis) were considered. The analysis revealed that, for cases (a) and (b), the distributions of ED values closely resembled each

other (differing by less than 0.5 Gy on average). In contrast, the utilization of very high late background subtraction led to an ED distribution that exceeded the average by a substantial margin at 1.5 Gy. Consequently, for the subsequent calculations, the standard background subtraction method, as in case (a), will be consistently applied. The discussion should be deepened and seen on a case-by-case basis; this should be the primary purpose of deconvolution applicability choice.

Turning our attention to the other parameters under investigation, such as τ, an insights is in figure 7.11, which presents the distribution of this parameters. In this figure, histograms representing the recombination lifetimes of each OSL component, categorized by regenerative dose and across the entire set of aliquots. It's noteworthy that τ was employed to examine the corresponding photoionization cross section values, as documented in table 7.4.

σ_1 (cm^{-2})	σ_2 (cm^{-2})	σ_3 (cm^{-2})
$(9.1 \pm 3.3) \times 10^{-16}$	$(4.5 \pm 2.3) \times 10^{-18}$	$(7.9 \pm 2.8) \times 10^{-18}$

Table 7.4: Cross section (σ) values for CPM_84 per each component

As expected, the figure reveals a significant trend: traps with larger cross-sectional areas at the stimulation wavelength utilized in measurements tend to evacuate rapidly, thereby giving rise to the fast decay component. In contrast, traps with smaller cross sections contribute to the emergence of the medium and slow decay components [97].
However, the most crucial observation derived from the graphs in figure 7.11 is the asymmetry present in all the distributions. In many instances, these distributions exhibit a tail skewed towards higher values, a characteristic commonly associated with binomial or log-normal distributions [99]. The physical significance of such a distribution implies the potential existence of two distinct populations within the distribution. It is important to recall that the recombination lifetime parameter τ is reflective of the origin of the quartz grains, and the distribution characteristics strongly indicate a complex origin of the mineral. One plausible hypothesis is that the theater's location stands between two rivers, hinting at a dualistic nature in the populations of quartz grains. Following discussion with the group from the CiRCe department of

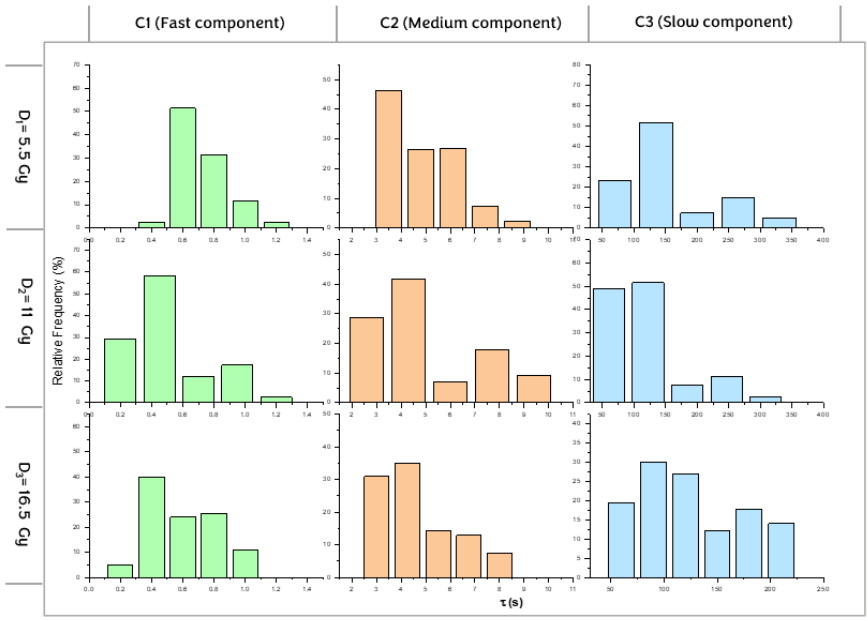

Figure 7.11: Histograms show the distribution of recombination lifetimes for the fast, medium, and slow OSL components associated with each regenerative dose within the SAR protocol framework.

the University of Padua, this dualism was confirmed. Mineralogical observations conducted and being published were able to confirm that the theater sand was most likely from both the Bacchiglione and Brenta rivers.

Shifting attention to the analysis of residuals and the assessment of skewness and kurtosis values, distributions of these parameters were examined, as depicted in figure 7.12. Skewness exhibited a range of values between 3.40 and 7.91, while kurtosis parameters spanned from 20.46 to 86.33. The kurtosis has a distribution with a centroid value of 34.98 and a full width at half maximum (FWHM) of 23.65. On the other hand, the skewness distribution, displayed a centroid of 4.82 and an FWHM of 1.75.
For CPM_84, the calculation of ED involved the exclusion of aliquots that fell outside the predefined intervals: 5.35 ± 1.75 for skewness and 37.89 ± 23.65

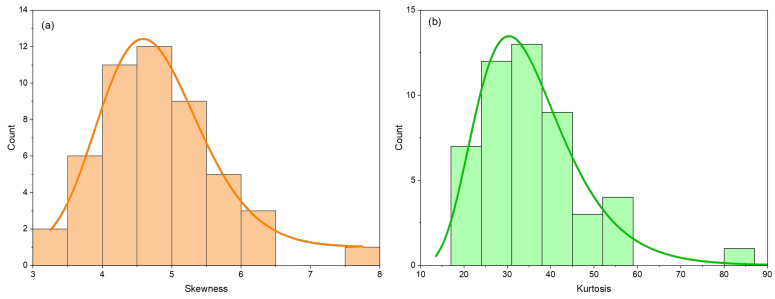

Figure 7.12: Distribution of skewness and kurtosis values over all aliquots.

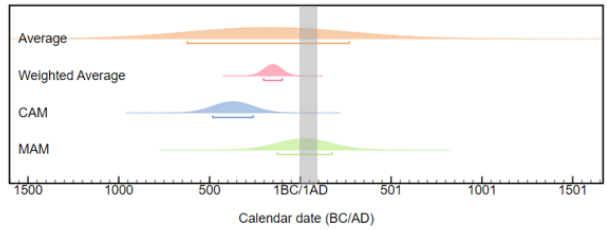

Classical Statistic	Equivalent Dose (ED) (Gy)	Age (Years)	Date
Average	7.00 ±1.42	2200 ± 445	175 BC ± 445
Weighted Average	6.93 ± 0.16	2175 ± 50	150 BC±50
CAM	7.62 ± 0.36	2390 ± 110	365 BC ± 110
MAM	6.37± 0.49	2000 ± 150	25 AD ± 150

Figure 7.13: CPM_84 sample age with exclusion critieria proposed by the new analysis path for each statistical method used. In gray the assumed age period.

for Kurtosis. Notably, only 21 out of the 49 aliquots met the skewness criterion, with a total of 18 aliquots satisfying both skewness and kurtosis criteria. It's important to note that all 18 of these selected aliquots also successfully passed the recycling ratio and recovery test.
Subsequently, ED and age values were derived exclusively from these 18 aliquots, resulting in the ages depicted in figure 7.13.
CPM_84 was involved in the first trial of the new protocol. This resulted in a recently published article attached to this thesis on page 141 [44]

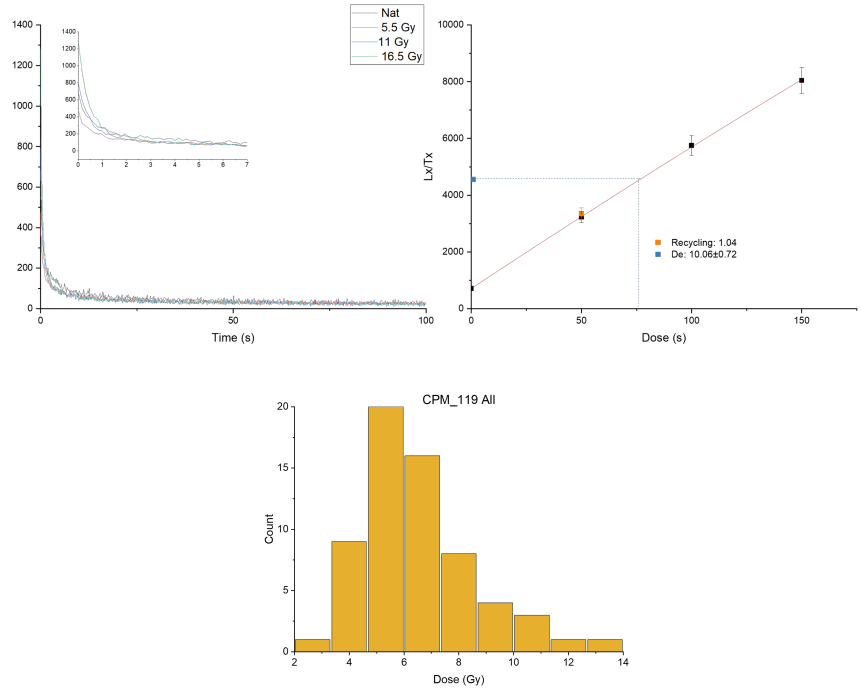

Figure 7.14: A signal and OSL growth values for a CPM_119 aliquot and its ED distribution

CPM_119

Approximately 5.89 g of quartz was extracted from sample CPM_119, and no signals were detected from feldspars. Out of the 62 aliquots analysed, 37 met the selection criteria of the SAR protocol.
For most of the samples, the OSL shine-down trend exhibited minimal noise. The distribution of Equivalent Dose values is asymmetric, and have an average value of approximately 6 Gy. In this particular sample, both classical and new path yielded much older dates than expected. This discrepancy suggests a complex history of quartz deposition and mixing, resulting in incomplete bleaching, a conclusion supported by the shape of the Equivalent Dose value distribution (figure 7.14).
The calculated dose rate value was **1.35** ± **0.07** (mGy/y). Despite some mar-

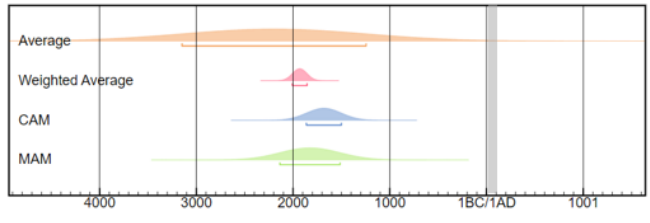

Classical Statistic	Equivalent Dose (ED) (Gy)	Age (Years)	Date
Average	7.00 ±1.42	4220 ± 950	2195 BC ± 950
Weighted Average	6.93 ± 0.16	3950 ± 75	1925 BC ± 75
CAM	7.62 ± 0.36	3710 ± 180	1685 BC ± 180
MAM	6.37± 0.49	3850 ± 310	1825 AD ± 310

Figure 7.15: CPM_119 sample age with exclusion criteria proposed within SAR protocol (recycling ratio and recuperation) for each statistical method used. In gray the assumed age period.

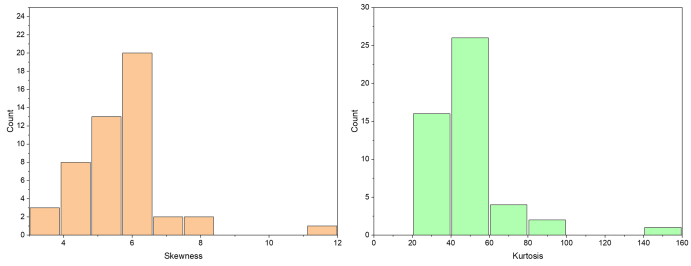

Figure 7.16: Distribution of skewness and kurtosis values over all CPM_119 aliquots

gin of error, the resulting dates, as depicted in the figure, significantly deviate from the expected dates. For the CPM_119 sample, deconvolution analysis was not conducted due to the signals exhibiting low sensitivity and lacking a distinct curve delineating the fast component.
Instead, we focused on selecting Skewness and Kurtosis values, the distribution of which show a Full Width at Half Maximum (FWHM) of 1.37 and 23.26, respectively. Subsequently, we considered Equivalent Dose (ED) values falling within the range of 5.35 ± 1.37 for skewness and 37.89 ± 23.26 for kurtosis. In this instance, following the selection of rates within the skewness

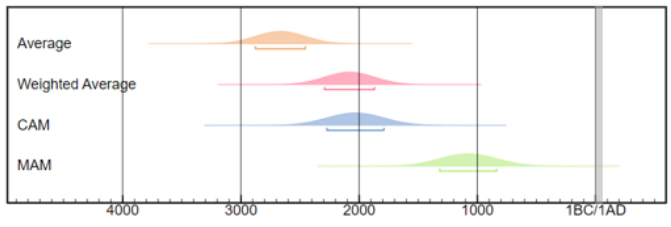

Classical Statistic	Equivalent Dose (ED) (Gy)	Age (Years)	Date
Average	6.31 ±0.38	4690 ± 210	2665 BC ± 210
Weighted Average	5.52 ± 0.28	4100 ± 220	2075 BC ± 220
CAM	6.03 ± 0.32	4055 ± 240	2035 BC ± 240
MAM	4.17± 0.46	3100 ± 245	1075 AD ± 245

Figure 7.17: CPM_119 sample age with exclusion criteria proposed by the new analysis path for each statistical method used. In gray the assumed age period.

and kurtosis parameters, the resulting dates appeared to be even more older. Out of the total only 30 aliquots were selected. Examining the deconvolution of CPM_119 curves could be advantageous, particularly when the choice of the appropriate background has the potential to see different distribution and results of Equivalent Doses (figure 7.17).

CCM_7

Sample CCM_7 is from coring a more massive portion of mortar. About 1.02 g of quartz were extracted. Two chemical attack in HF were required to remove the signal from the feldspars. The material extracted allowed the measurement of only 27 aliquots, 14 of which passed the SAR tests. As can be seen from figure 7.18 the curves for the most part were much noisier than in the previous two samples. The distribution of equivalent dose has values much higher than average. For the age establishment, both the classical and the new path provided dates significantly older than expected but more in accordance than CPM_119 considering the error, with dates that should be expected (figure 7.19).
The calculated dose rate value is high: **2.68 ± 0.11** (mGy/y). For the CCM_7 sample, deconvolution analysis was also omitted because of the low sensi-

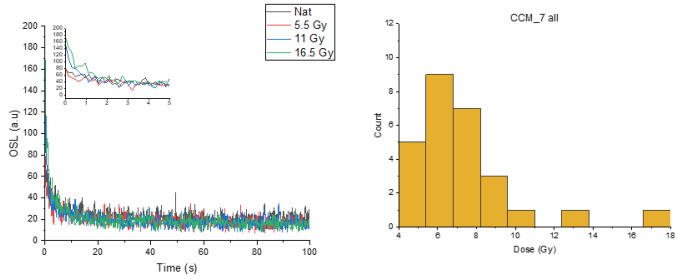

Figure 7.18: A signal and OSL growth values for a CCM*7* aliquot and its ED distribution

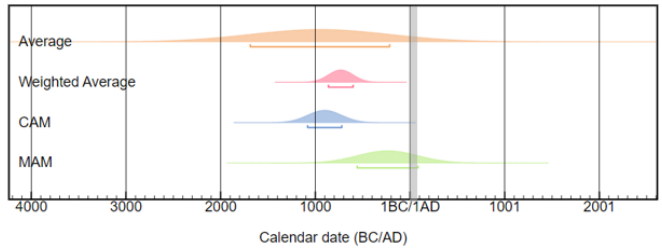

Classical Statistic	Equivalent Dose (ED) (Gy)	Age (Years)	Date
Average	6.80 ± 1.68	2975 ± 735	955 BC ± 735
Weighted Average	6.30 ± 0.30	2755 ± 130	730 BC ± 130
CAM	6.68 ± 0.41	2925 ± 180	900 BC ± 180
MAM	5.16 ± 0.74	2260 ± 320	235 AD ± 320

Figure 7.19: CCM*7* sample age with exclusion criteria proposed within SAR protocol (recycling ratio and recuperation) for each statistical method used. In gray the assumed age period.

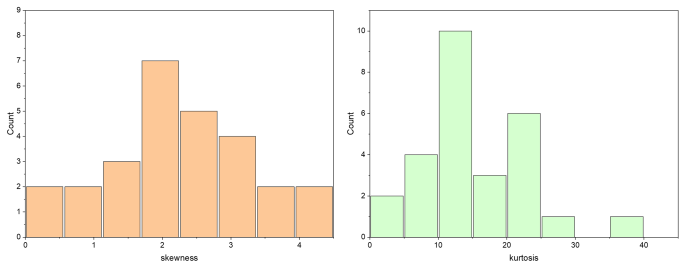

Figure 7.20: Distribution of skewness and kurtosis values over all CCM_7 aliquots

tivity of the signals and the lack of a distinct curve delineating the fast component. Instead, the selection of skewness and kurtosis values was carried out. The distribution of these values showed a maximum width in the middle (FWHM) of 1.31 and 10.75, respectively. Next, equivalent dose (ED) values in the range of 5.35$\pm$ 1.31 for skewness and 37.89 $\pm$ 10.75 for kurtosis were considered, as shown in figure 7.20. In this context, after rate selection within the skewness and kurtosis parameters, the resulting dates appeared even older. Only 13 aliquots were selected out of the total.

7.3 Cannero Castle

Three samples were from Cannero Castles site, specifically identified as MM16, PM15, and PM12. This historical site has undergone extensive analysis by Inter-Departmental Research Centre for the Study of Cement Materials and Hydraulic Binders (CIRCe) affiliated with the University of Padua [81]. Throughout the course of the research campaign, the various structural phases were explored that had been implemented over time within the castle's construction. It is noteworthy that the three mortars in question originated from distinct sections of the castle, each added during different historical periods. Furthermore, these samples underwent radiocarbon dating, a commonly employed dating method that, in the case of mortars, is known to present challenges related to carbonate isolation due to the inherent carbonation phase [40, 41].
The radiocarbon dating yielded a notably broad range of ages for the samples, although these results remained consistent with the known construction his-

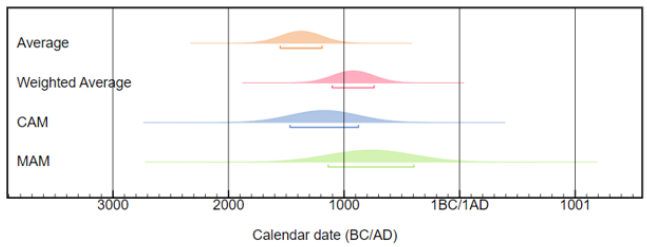

Classical Statistic	Equivalent Dose (ED) (Gy)	Age (Years)	Date
Average	7.76 ± 0.42	3395 ± 180	1370 BC ± 180
Weighted Average	6.72 ± 0.42	2940 ± 180	925 BC ± 180
CAM	7.3 ± 0.62	3195 ± 295	1171 BC ± 295
MAM	6.37 ± 0.84	2790 ± 370	765 BC ± 370

Figure 7.21: CCM_7 sample age with exclusion criteria proposed by the new analysis path for each statistical method used. In gray the assumed age period.

Location	Sample	Expected age
Cannero Castle	MM16	1525-1791 AD
	PM12	1694-1919 AD
	PM15	1409-1444 AD

Table 7.5: Expected ages of Cannero Castles' samples referred to ^{14}C results

tory of the site (see table 7.5. The sampled materials have weights spanning from 55.92 g to 15.65 g. The radioactive content analysis was only on the samples themselves, providing no information into the environmental context. Regarding the environment in which the castles are situated, they are situated approximately 300 meters from the nearest shores of Lake Maggiore, in northen Italy. Consequently, they can be characterized by exceedingly humid, with a significant presence of water that should be considered in the analyses.

MM16

Sample MM16 was from the eastern section of the castle, specifically from the tower's courtyard, where an intriguing graffito with the inscription "1522" was discovered (see figure 5.2). This sample stands out as the biggest among

Sample	Water content (%)	^{238} U (ppm; ± 5%)	^{232} Th (ppm; ± 5%)	^{40} K (ppm; ± 3%)	Internal dose rate (mGy/y)	External dose rate (mGy/y)	Dose rate (mGy/y)
MM16	18	2.00	6.33	1.21	1.24	0.73	1.75 ±0.09
PM12	23	1.72	5.43	3.57	2.65	1.11	1.50 ± 0.07
PM15	32	1.89	5.96	1.10	1.14	0.68	3.08 ± 0.15

Table 7.6: radioactive content, internal and external dose rate of Cannero Castles' mortar samples. he dose rate is calculated with the parametres defined by Guerin et.al. [95]

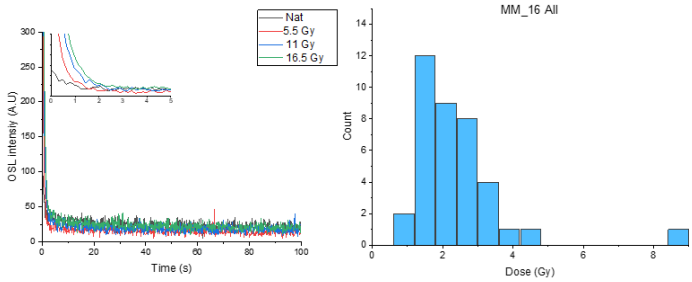

Figure 7.22: A signal and OSL growth values for a MM16 aliquot and its ED distribution

those that from the site, weighing approximately 55.92 g. During the chemical attack process, approximately 1.90 grams of quartz were extracted. Two rounds of treatment with hydrofluoric acid (HF) were necessary due to the presence of feldspars IR signal.
From the obtained material, 40 aliquots were get. Remarkably, slightly more than half of these aliquots passed the recovery and recycling test, amounting to a total of 21 successful aliquots.
Unfortunately, the samples exhibited very low natural signal, resulting in notably noisy curves in most instances. Moreover, with the exception of a single outlier, the distribution of equivalent dose values consistently fell within the range of 1-5 Gy. However, the shape of this distribution hints at a complex history of mortar bleaching. When relying solely on the SAR exclusion criteria, the dates obtained for MM16 appeared to be older than initially anticipated, accompanied by a considerable degree of uncertainty.

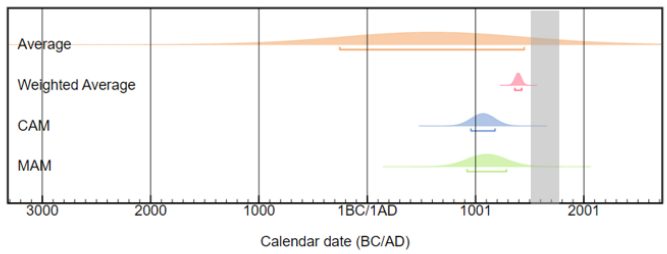

Classical Statistic	Equivalent Dose (ED) (Gy)	Age (Years)	Date
Average	2.5 ± 1.5	1425 ± 850	600 AD ± 850
Weighted Average	1.11 ± 0.05	630 ± 30	1395 AD ± 30
CAM	1.68 ± 0.19	955 ± 110	1070 AD ± 110
MAM	1.62 ± 0.31	920 ± 180	1105 AD ± 180

Figure 7.23: MM16 sample age with exclusion criteria proposed within SAR protocol (recycling ratio and recuperation) for each statistical method used. In grey the assumed age period.

MM16 new path results

Sample MM16 was selected for deconvolution due to its abundance of aliquots, making it an ideal candidate for analysis. However, the process proved to be quite challenging, as the samples exhibited poor signal quality. In certain instances, even the add-in component of the Excel, Solver, utilized to make deconvolution observation, failed to identify a definitive solution. Remarkably, only 14 out of the 40 aliquots yielded deconvolutions, and none of these possessed a Figure of Merit (FOM) $<$15%. This unequivocally suggests that the fitting procedure was inadequate.

Nevertheless, some insights can still be obtain from the data. The dominant components of the curve were undoubtedly the slow component, followed by the medium component. The former consistently constituted approximately 70% of the curve, while the medium component contributed between 10% and 20%. Notably, the fast component exhibited lower percentages compared to what was observed in the CPM_84 sample, with signal variations ranging from 0.5% to a maximum of 5%.

In general, figure 7.25 reveals a trend in percentage contribution similar to that of CPM_84, although constrained by the limited data set under consid-

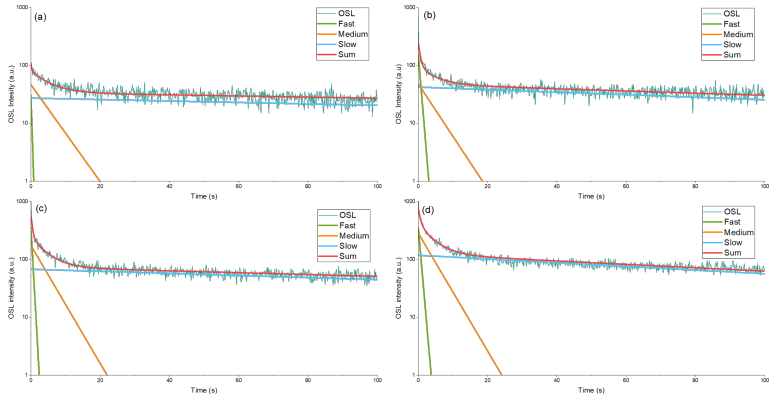

Figure 7.24: Deconvolution analysis of OSL decay curves in MM16, which were acquired within the context of the SAR protocol, using the same aliquot. These instances pertain to the following conditions: (a) natural dose, (b) first regenerative dose, (c) second regenerative dose, and (d) third regenerative dose.

eration. Significantly, again the signal was not affected predominantly by the fast component.
Given these outcomes, it was not feasible to get in a meaningful discussion regarding the choice of background subtraction, whether early or late.
However, commenting on the results concerning other parameters presents its own challenges. It is highly probable that, unlike the Padua sample, the quartz in this particular sample originates from a single source, namely the beach at Cannero Riviera. This would imply a distinct trend in the τ parameter. Remember that τ also serves as an indicator of the population distribution, and although the trend appears to be more in line with a normal or log-normal distribution, it remains challenging to confirm definitively. We anticipate further attempts at deconvolution, with modifications to the SAR protocol measurement parameters, in pursuit of more conclusive results.

The results obtained through skewness and kurtosis filtering are considerably more comforting. This selection not only improved the accuracy of the ages, approaching them closely with the expected values, but it also demonstrated a high level of agreement across all the chosen statistical methods. Notably, the distribution exhibited a distinctive trend, leaning towards higher values. The Full Width at Half Maximum (FWMH) values were 0.79 for skewness and 15.0 for kurtosis. To understand the selection intervals, simulated

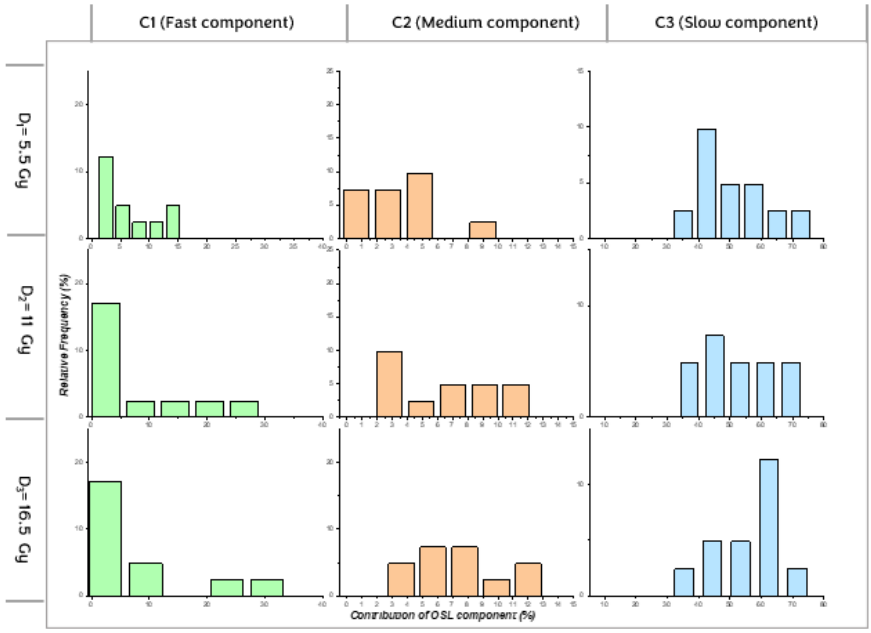

Figure 7.25: Histograms show the distribution of the percentage of the fast, medium, and slow OSL components for every regenerative dose within the SAR protocol framework. Correspond to the values acquired through deconvolution analysis for all parameters in MM16

values were used for an ideal curve $\pm$ the FWMH (see figure 4.1). Surprisingly, only 12 rates met the criteria for acceptance, and out of these, 6 also successfully passed the SAR recovery tests.
This samples underscores the significance of starting with a large number of aliquots, as multiple selection criteria led to a reduced and non-statistically significant dataset. The resulting age results are visualized in the accompanying figure 7.27.

PM_12

Sample PM12, originating from the westernmost section of the castle, is presumed to be the most recent. Radiocarbon measurements have produced results that extend back only as far as the 20th century, suggesting it likely dates

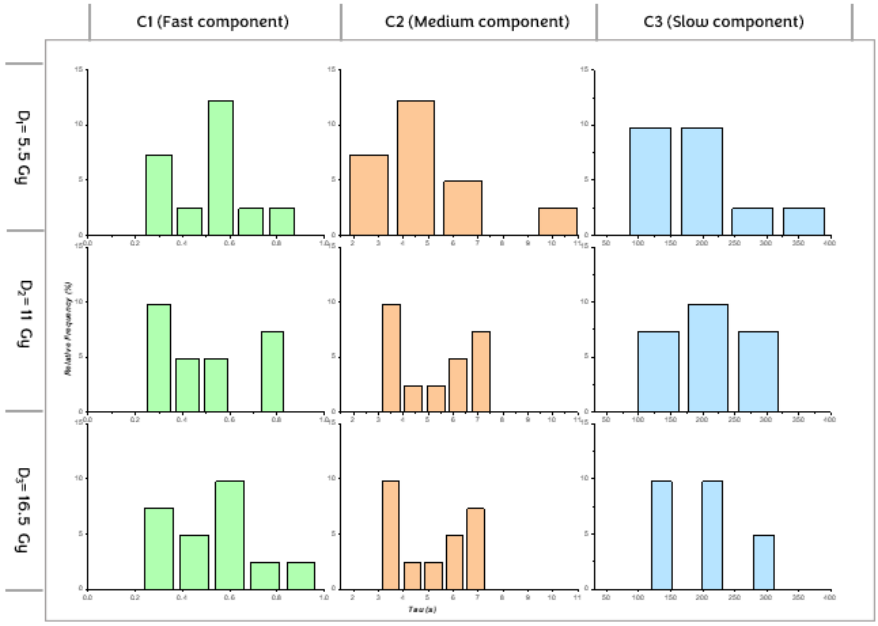

Figure 7.26: Histograms show the distribution of recombination lifetimes for the fast, medium, and slow OSL components associated with each regenerative dose within the SAR protocol framework for MM16 sample.

to the period preceding the fortress's complete abandonment.
This particular sample posed challenges in terms of quartz selection, as signals from feldspars persisted despite multiple chemical treatments and particle size selection. However, this led to the attempt of use Infrared Stimulated Luminescence (IRSL) dating alongside the ongoing OSL dating.
The discussion will continue to encompass both OSL and IRSL dating approaches. The parameters chosen for IRSL measurements are presented in the figure 7.28, involving three regenerative doses of 3.3 Gy, 6.6 Gy, and 9.9 Gy. Out of the isolated quartz fraction, 13 aliquots were subjected to IRSL analysis, while 11 underwent OSL analysis. In the former case, only one aliquot was excluded due to its recycling ratio of 0.8, whereas all 11 OSL rates were acceptable. Unfortunately, additional aliquots could not be analysed due to the substantial reduction in analysable material caused by chemical treatments.

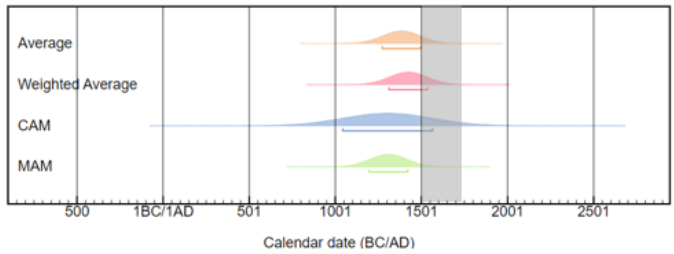

Classical Statistic	Equivalent Dose (ED) (Gy)	Age (Years)	Date
Average	1.2 ± 0.2	640 ± 110	1385 AD ± 110
Weighted Average	1.12 ± 0.25	595 ± 110	1425 AD ± 110
CAM	1.45 ± 0.45	720 ± 260	1305 AD ± 260
MAM	1.44 ± 0.20	715 ± 110	1310 AD ± 110

Figure 7.27: MM16 sample age with exclusion criteria proposed by the new analysis path for each statistical method used. In gray the assumed age period.

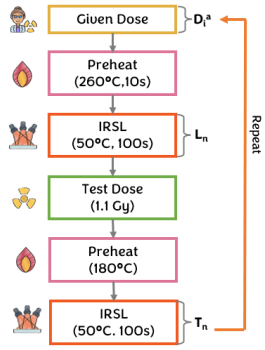

Figure 7.28: SAR protocol applied for IRSL. Where a) i = 1–4 correspond to D_1 = 0 Gy (Natural), $D_2 - D_4$ Regenerative doses (3.3, 6.6 and 9.9, Gy), D_5= 0 Gy (Recuperation test), D_6= D_2 (Recycling point)

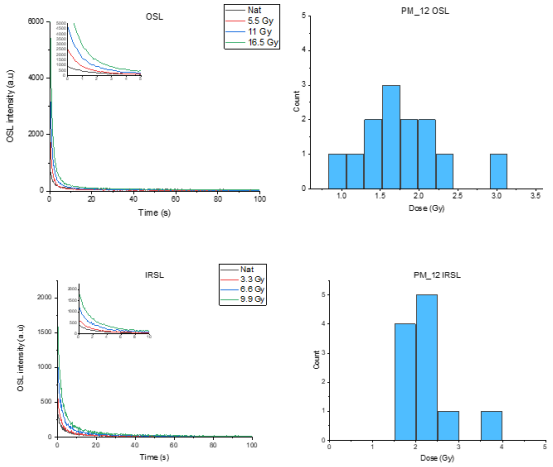

Figure 7.29: A signal and OSL growth values for a PM12 aliquot and its ED distribution, both for OSL and IRSL

Nevertheless, both OSL and IRSL curves displayed good shine-downs in their signals. IRSL distribution of ED values in IRSL exhibited a more concentrated pattern around a single value. Conversely, ED values measured during OSL exhibited a more distribution, almost Gaussian trend. This suggests the likelihood of the mortar's history being characterized by a significant degree of bleaching.

Despite the favourable signals and ED distribution, the calculated ages do not align with the radiocarbon values. However, there is greater agreement with the time frame encompassing the construction of the castle up to its initial abandonment (as indicated by the yellow interval in figure 7.30). The mortar appears to correspond more closely to this broader period than to a more recent one. This result holds true for both OSL and IRSL measurement methods and their respective selections. Regarding the selection based on skewness and kurtosis, all rates successfully passed this criteria as well. The specified range for OSL included skewness between 5.35 ± 1.4 and kurtosis 37.89 ± 16.71, while for IRSL, it encompassed skewness between 5.35 ± 1.48 and kurtosis 37.89 ± 9.6. Once again, these chosen statistical methods appear to converge more effectively following this selection process.

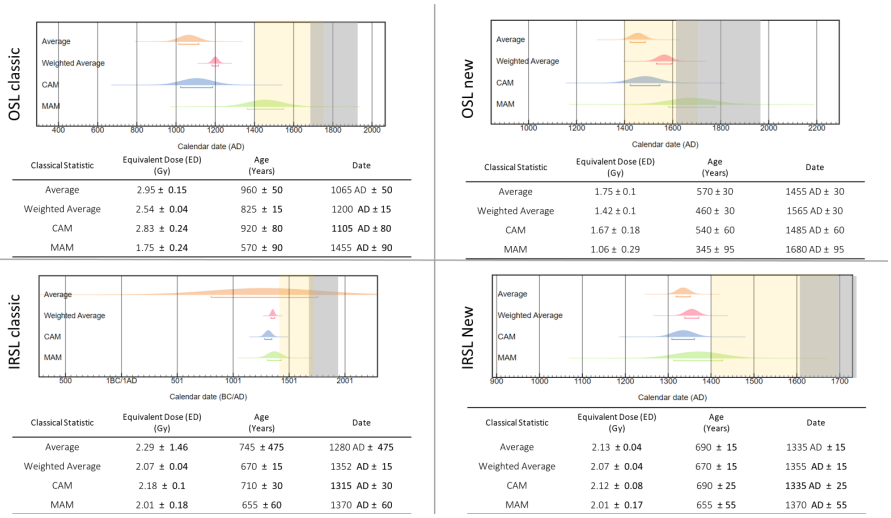

Classical Statistic	Equivalent Dose (ED) (Gy)	Age (Years)	Date
Average	2.95 ± 0.15	960 ± 50	1065 AD ± 50
Weighted Average	2.54 ± 0.04	825 ± 15	1200 AD ± 15
CAM	2.83 ± 0.24	920 ± 80	1105 AD ± 80
MAM	1.75 ± 0.24	570 ± 90	1455 AD ± 90

Classical Statistic	Equivalent Dose (ED) (Gy)	Age (Years)	Date
Average	1.75 ± 0.1	570 ± 30	1455 AD ± 30
Weighted Average	1.42 ± 0.1	460 ± 30	1565 AD ± 30
CAM	1.67 ± 0.18	540 ± 60	1485 AD ± 60
MAM	1.06 ± 0.29	345 ± 95	1680 AD ± 95

Classical Statistic	Equivalent Dose (ED) (Gy)	Age (Years)	Date
Average	2.29 ± 1.46	745 ± 475	1280 AD ± 475
Weighted Average	2.07 ± 0.04	670 ± 15	1352 AD ± 15
CAM	2.18 ± 0.1	710 ± 30	1315 AD ± 30
MAM	2.01 ± 0.18	655 ± 60	1370 AD ± 60

Classical Statistic	Equivalent Dose (ED) (Gy)	Age (Years)	Date
Average	2.13 ± 0.04	690 ± 15	1335 AD ± 15
Weighted Average	2.07 ± 0.04	670 ± 15	1355 AD ± 15
CAM	2.12 ± 0.08	690 ± 25	1335 AD ± 25
MAM	2.01 ± 0.17	655 ± 55	1370 AD ± 55

Figure 7.30: Results and age comparison for each method (IRSL and OSL) and for each selection criterion (classic and new). In grey the assumed radiocarbon age and in yellow the construction age of the entire structure.

PM_15

Sample PM15 was collected from the eastern section of the main garden. This area is believed to be one of the earliest constructed, as it dates back to the 15th century when the small island was initially conquered by the Mazzarditi family and later by the Borromeo family.

This sample yielded the most precise date range achieved through radiocarbon measurements. The results concurred with the hypothesis of construction occurring between 1409 and 1444.

Once again, a significant signals were derived from feldspar. The isolated quartz fraction was sieved into multiple fractions. Experimentation with various grain sizes was essential to determine the optimal configuration for our instrument and SAR protocol parameters. This mortar sample was one of our initial attempts at dating.

The fractions were categorized as follows: 80-180 µm, 180-250 µm, and $>$ 250 µm, resulting in 44, 36, and 17 aliquots, respectively, for preparation and measurement. Upon starting of the analyses, the intermediate fraction emerged as the preferred choice. The selection criteria were based on the number of

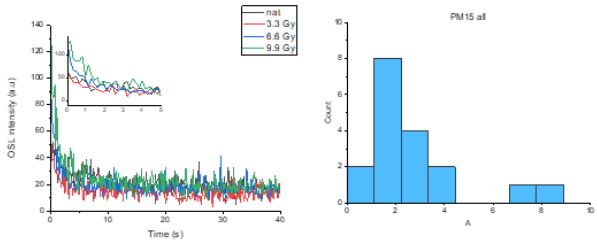

Figure 7.31: A signal and OSL growth values for a PM15 aliquot and its ED distribution

aliquots exhibiting excellent recuperation and recycling ratios. Consequently, the particle size range of 180-250 µm was chosen for all subsequent aliquots. 23 aliquots passing SAR tests within this selection.
For this pilot test, the sample underwent a 40s OSL stimulation, with plans to adjust the stimulation time in future samples. The signal exhibited a notable degree of noise. Moreover, aside from two values outside the distribution, the average ED value was around 1.5 Gy. Utilizing a weighted average approach and the Minimum Age Model (MAM) criterion, the results of the classical SAR protocol closely aligned with both the assumed dates derived from radiocarbon dating and our prior knowledge of the site's historical background. However, when applying the additional criteria of skewness and kurtosis for selection, we encountered a similar issue as with sample MM16, resulting in an insufficient number of aliquots (only 7). Nonetheless, these dates displayed a close correspondence with each other and enhanced the agreement with the expected construction date. In this particular case, the selection intervals for skewness and kurtosis were adjusted for the 40-second stimulation, with the chosen range being 2.14 ± 0.63 for skewness and 15.15 ± 4.73 for kurtosis.

7.4 Sarno bath - Pompeii

The site of Sarno baths in Pompeii yielded a total of five samples, representing different groups as detailed in section 5.3. Among these samples, only one, labelled as M245, is of ancient origin and dates back to the period of reconstruction that followed the earthquake in Pompeii in 63 AD. The remaining

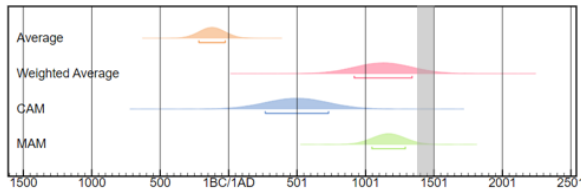

Classical Statistic	Equivalent Dose (ED) (Gy)	Age (Years)	Date
Average	3.22 ± 0.14	2145 ± 95	120 BC ± 95
Weighted Average	1.34 ± 0.31	895 ± 210	1130 AD ± 210
CAM	2.29 ± 0.35	1525 ± 230	500 AD ± 230
MAM	1.28 ± 0.18	855 ± 120	1170 AD ± 120

Figure 7.32: PM15 sample age with exclusion criteria proposed within SAR protocol (recycling ratio and recuperation) for each statistical method used. In grey the assumed age period.

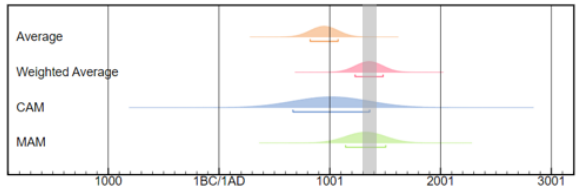

Classical Statistic	Equivalent Dose (ED) (Gy)	Age (Years)	Date
Average	1.61 ± 0.19	1075± 125	950 AD ± 125
Weighted Average	1.00 ± 0.19	670 ± 125	1356 AD ± 125
CAM	1.51 ± 0.36	1005 ± 345	1015 AD ± 345
MAM	1.05 ± 0.42	700 ± 180	1325 AD ± 180

Figure 7.33: PM15 sample age with exclusion criteria proposed by the new analysis path for each statistical method used. In gray the assumed age period

Location	Sample	Expected age
Sarno Bath	M245	I-II cent. CE
	M255 M256 M261 M266	Restoration after 1630 AD

Table 7.7: Expected ages of Pompei samples

samples are considerably more recent, according their composition, characterized by the presence of materials like leucite, suggesting a post quem date after the 17th century. These samples exhibit remarkably high radioactivity levels, most likely attributed to the specific geographical location from which they were sourced. No data is available regarding the radioactivity values of the surrounding environment, and it was assumed to be similar to that of the samples.

Sample	Water content (%)	^{238}U (ppm; ± 5%)	^{232}Th (ppm; ± 5%)	^{40}K (ppm; ± 3%)	Internal dose rate (mGy/y)	External dose rate (mGy/y)	Dose rate (mGy/y)
M245	14	5.58	17.63	2.62	2.95	1.89	4.55 ±0.22
M255	19	4.81	15.21	3.57	3.88	1.89	6.64 ± 0.33
M256	23	8.89	28.38	3.57	2.88	2.93	6.16 ± 0.30
M261	17	7.06	22.32	4.31	4.35	2.59	6.06 ± 0.30
M266	23	6.22	19.65	2.86	3.25	2.10	4.57 ± 0.23

Table 7.8: radioactive content, internal and external dose rate of Sarno Bath mortar samples.he dose rate is calculated with the parametres defined by Guerin et.al. [95]

Unfortunately, out of the five samples, we were only able to extract datable material from one, M245. In the case of the other Pompeii samples, our attempts to obtain quartz were unsuccessful. Even after subjecting them to extraction using the heavy liquid method, the resulting material proved to be of poor quality and exhibited a dark colour, making it definitively non-attributable to quartz mineralogy. Based on the XRPD analysis conducted in collaboration with the University of Padua research team, it was evident that in nearly all the samples, the quartz content registered at less than 1% [86]. Meanwhile, the amorphous phase and K-feldspar were notably abundant.
Sample M261 also presented an abundance of micas, which proved challenging to completely remove.

Method	ED (Gy)	ED err (Gy)	Age (year)	Date	Error
Weighted Mean	5.5	0.2	1265	*760*	80
Mean	8.5	0.9	1950	*70*	*250*
MAM	4.3	0.8	990	1030	210

Table 7.9: Age results after Single Grain analysis on M245

Sample M266 contained very limited quartz, and only six aliquots were suitable for analysis, with four of them meeting the acceptability criteria. Despite these limitations, the weighted averaging of its equivalent doses yielded a dating result of 1560 AD $\pm$ 110.

M245

Being one of the first samples of the M245 study as PM15 served to calibrate the parameters of the SAR protocol. Due to the limited amount of available material, it was not possible to make a mineral size selection.
M245 also stood as the sole specimen analysed using the single-grain technique. Out of the 3800 grains examined, only 30 met the criteria for acceptability. Nevertheless, the results obtained from this single-grain analysis are presented in the table 7.9. Subsequently, the Multigrain analysis was continued. Out of the 39 aliquots subjected to testing, 10 did not pass the SAR protocol criteria. However, it's noteworthy that the results remained consistent with the initial assumptions.

7.5 Capiate

The Capiate site was the last to be analysed. Due to the characteristics observed from the first OSL measurement, it was decided to proceed with a 125°C stimulus for only 40s. Additionally, four distinct radiation doses were imparted: 4.4, 8.8, 13.2, and 17.6 Gy.
Among the collection of fourteen samples extracted from the site, four specific samples were selected for analysis. These particular samples were chosen due to their higher degree of date certainty, established a priori. The radioactive content analysis was only on the samples themselves, providing no information into the environmental context.

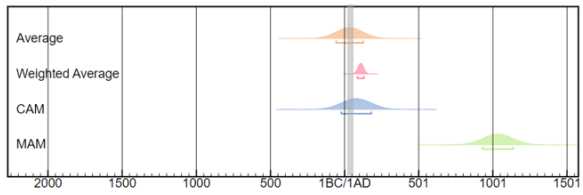

Classical Statistic	Equivalent Dose (ED) (Gy)	Age (Years)	Date
Average	866 ± 0.35	1990 ± 90	35 AD ± 90
Weighted Average	8.33 ± 0.38	1915 ± 20	110 AD ± 20
CAM	8.47 ± 0.45	1945 ± 100	80 AD ± 100
MAM	4.31 ± 0.43	990 ± 100	1035 AD ± 100

Figure 7.34: M245 sample age with SAR exclusion criteria for each statistical method used. In gray the assumed age period

Sample	Sampling Point	Weight	Expected age
CT2	Tower	550g	First half of 5th century
CT3	Tower	1550g	Approx. 570 AD
CT8	Tower arching	31g	2nd century
CA1	Church Apse	101.8g	X-XI century

Table 7.10: Expected ages and sampling point of Capiate samples

Generally, a substantial quantity of quartz was readily obtained from the Capiate samples.

Sample	Water content (%)	^{238}U (ppm; ± 5%)	^{232}Th (ppm; ± 5%)	^{40}K (ppm; ± 3%)	Internal dose rate (mGy/y)	External dose rate (mGy/y)	Dose rate (mGy/y)
CT2	13	0.90	2.85	1.1	0.91	0.43	1.32 ±0.06
CT3	15	0.68	2.15	1.38	1.04	0.44	1.41 ± 0.07
CT8	16	1.32	4.18	1.05	0.98	0.53	1.44 ± 0.07
CA1	19	3.01	9.52	1.16	1.44	0.97	2.19 ± 0.10

Table 7.11: radioactive content, internal and external dose rate of Capiate's mortar samples. he dose rate is calculated with the parametres defined by Guerin et.al. [95]

CT2

A total of 48 aliquots were analysed for sample CT2. It came from the portion of the tower that should date back to the first half of the fifth century.
Of the 48 aliquots, most were suitable for the SAR protocol recycling and recovery tests, 32 to be precise.

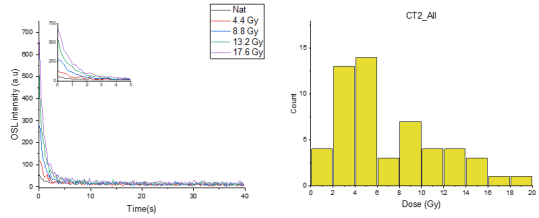

Figure 7.35: A signal and OSL growth values for a CT2 aliquot and its ED distribution

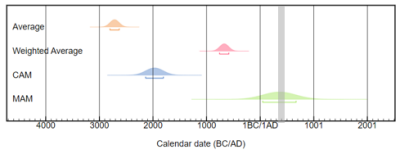

Classical Statistic	Equivalent Dose (ED) (Gy)	Age (Years)	Date
Average	6.26 ± 0.11	4735 ± 85	2715 BC ± 85
Weighted Average	3.56 ± 0.11	2695 ± 85	670 BC ± 85
CAM	5.28 ± 0.22	3995 ± 165	1970 BC ± 165
MAM	2.2 ± 0.41	1665 ± 310	360 BC ± 310

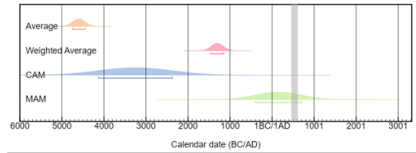

Classical Statistic	Equivalent Dose (ED) (Gy)	Age (Years)	Date
Average	8.75 ± 0.2	6620 ± 150	4595 BC ± 150
Weighted Average	4.39 ± 0.2	3325 ± 150	1300 BC ± 150
CAM	6.97 ± 0.88	5275 ± 1880	3250 BC ± 1880
MAM	2.48 ± 0.73	1875 ± 550	150 ± 550

Figure 7.36: CT2 sample age with exclusion criteria proposed within SAR protocol (recycling ratio and recuperation) on the left, and new path on right for each statistical method used. In grey the assumed age period.

The OSL growth curve increased with dose, but the natural signal was not very intense. The distribution of the calculated equivalent dose values had a maximum around 4 Gy. The log-norm trend suggests a sample that was not well bleached.

As far as the ages are concerned, both the newly proposed method with the selection of Skewness and Kurtosis and the classical method lead back to much older dates. Only the MAM method agrees across the two protocols. Skewness and Kurtosis values are respectively 2.14 ± 0.87 and 15.15 ± 4.12.

CT3

A total of 57 aliquots from sample CT3 were subjected to dating analysis. Among these, 34 met the criteria established by classical methods for acceptability. Furthermore, the skewness and kurtosis criteria demonstrated a high level of acceptability, with 17 out of the 23 selected aliquots falling within the specified intervals (2.14 ± 0.69 and 15.15 ± 3.53). Sample CT3, originating

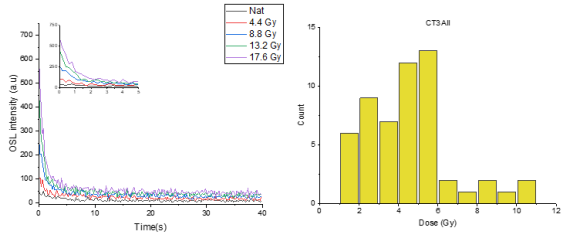

Figure 7.37: A signal and OSL growth values for a CT3 aliquot and its ED distribution

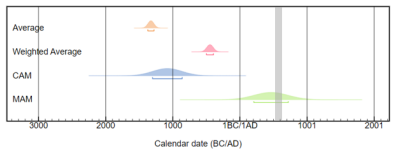

Classical Statistic	Equivalent Dose (ED) (Gy)	Age (Years)	Date
Average	4.72 ± 0.07	3345 ± 50	1325 BC ± 50
Weighted Average	3.48 ± 0.07	2470 ± 50	445 BC ± 50
CAM	4.38 ± 0.31	3105 ± 220	1080 BC ± 220
MAM	2.2 ± 0.36	1560 ± 255	465 ± 255

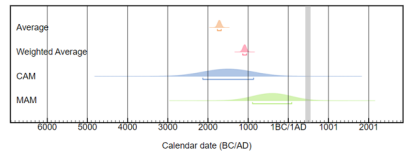

Classical Statistic	Equivalent Dose (ED) (Gy)	Age (Years)	Date
Average	5.26 ± 0.07	3740 ± 45	1715 BC ± 45
Weighted Average	4.67 ± 0.07	3110 ± 45	1085 BC ± 45
CAM	5.29 ± 0.42	3520 ± 630	1495 BC ± 630
MAM	3.64 ± 0.73	2420 ± 485	400 BC ± 485

Figure 7.38: CT3 sample age with exclusion criteria proposed within SAR protocol (recycling ratio and recuperation) on the left, and new path on right for each statistical method used. In grey the assumed age period.

from the same tower as CT2 but from a later period, is dated to approximately 570 AD. However, its luminescence properties, including shine-down and the distribution of Equivalent Dose (ED) values, exhibit noisy signals and potentially present dating challenges. In fact, in this case, the sample appears to yield older dates, potentially dating back to before the Common Era.

CT8

CT8 is the oldest sample from the Capiate site. It was taken from the inner arches of the north side of the tower. These archways are thought to be an imprint of earlier 2nd century construction. Despite the challenging nature of CT8's measurements, 54 aliquots were analysed. However, the recuperation and recycling tests yielded values falling outside the acceptable range, resulting in the analysis of only 30 aliquots. The natural signals remained remarkably low.

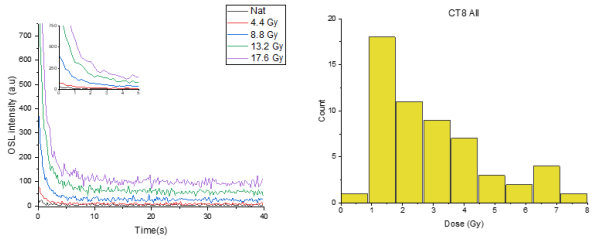

Figure 7.39: A signal and OSL growth values for a CT8 aliquot and its ED distribution

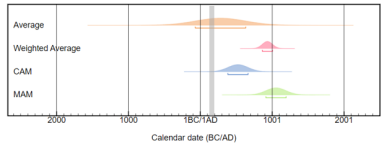

Classical Statistic	Equivalent Dose (ED) (Gy)	Age (Years)	Date
Average	2.51 ± 0.51	1740 ± 350	282 ± 350
Weighted Average	1.58 ± 0.09	1090 ± 70	935 ± 70
CAM	2.18 ± 0.2	1510 ± 140	525 ± 140
MAM	1.40 ± 0.2	970 ± 140	1055 ± 140

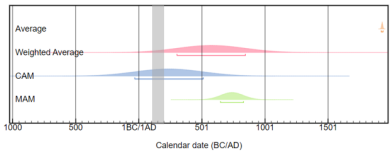

Classical Statistic	Equivalent Dose (ED) (Gy)	Age (Years)	Date
Average	2.61 ± 0.12	95 ± 5	1930 ± 5
Weighted Average	1.83 ± 0.34	1450 ± 270	575 ± 270
CAM	2.25 ± 0.34	1645 ± 270	240 ± 270
MAM	1.62 ± 0.11	1285 ± 90	740 ± 90

Figure 7.40: CT8 sample age with exclusion criteria proposed within SAR protocol (recycling ratio and recuperation) on the left, and new path on right for each statistical method used. In grey the assumed age period.

The dose distribution graph, deviating from normal expectations, hints at a complex history for the quartz in this samples. Paradoxically, this sample, which one would expect to be the oldest, appear to be the youngest in terms of its luminescence properties. This phenomenon leads us to speculate that at some point in a more recent history, was reset to zero. It probably underwent exposure to light, possibly during the various renovation phases of the tower structure.

Interestingly, the analysis results remained consistent when employing a selection method based on the criteria proposed in the new approach. Out of the selected curves, 11 were found to be suitable, and all of them were among the aliquots that already met the SAR criteria for acceptability.

The Skewness and Kurtosis intervals were determined to be as follows: 2.14 $\pm$ 0.39 and 15.15$\pm$ 3.33.

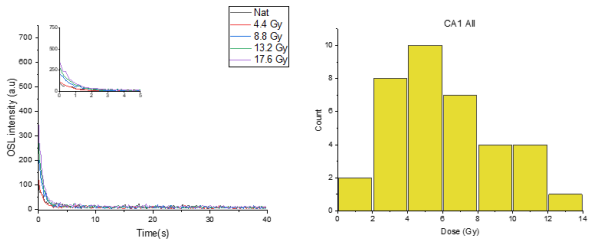

Figure 7.41: A signal and OSL growth values for a CA1 aliquot and its ED distribution

CA1

CA1 represents the sole sample examined from the small church of Capiate, specifically taken from its apse. It is believed that the church underwent extensive renovation, making this particular sample stand out as a potential marker of a new construction phase. The prevailing assumption places its origins in the 10th-11th century, largely due to the architectural style.
Out of the 37 aliquots studied, 20 failed to meet the SAR criteria. These curves exhibited significant slope and seemingly robust signals, but it's apparent that the quartz in the sand used for constructing the church's apse did not undergo adequate bleaching. Consequently, the dating results consistently pointed to much older ages. There is, however, one glimmer of optimism among these findings, namely the MAM when applying classical criteria, proposing a date of 845 AD $\pm$ 290 years. Notably, the selection based on skewness and kurtosis (2.14 $\pm$ 1.39 and 15.15 $\pm$5.08) only yielded 4 suitable aliquots. Unfortunately, this approach did not yield statistically significant results.
With the addition of seven more samples collected in the apse of the church, an intriguing comparative analysis looks set to take place.

8 Conclusion on mortars

This study has led a profound reevaluation of mortar dating and its feasibility. Our investigative path, firmly rooted in the theory of Optically Stimulated Luminescence, has produced innovative perspectives through the in-depth study of the raw OSL curve. Shifting the attention to the raw data allowed to propose innovative and non-trivial solutions for OSL mortar dating.
As we conclude this dissertation, after an in-depth analysis of 15 mortar samples, we can draw some conclusions about the method.
Mortars represent a complex system, with each sample revealing unique characteristics, even within the same sampling site. These distinctions arise not only from variations in construction techniques, which might have evolved over different historical phases, but also from the initial choice of raw materials. In the context of dating, the choice of sand, and consequently, the quality of quartz, becomes a key factor, as it can influence the viability of the dating process.
The intrinsic nature of quartz, particularly its treatment during the mortar preparation phase, remains a mystery for those of us attempting to date these mortars centuries later. The challenge of understanding the mechanisms of bleaching stands as a barrier to achieving precise dating results. Therefore, our research focus is directed toward overcoming this obstacle. The path chosen is that of statistical analysis, which makes it possible to differentiate suitable signals from unsuitable ones and to identify grains with the ideal characteristics.
A general observation emerged: the OSL shine-down curve often has a relatively low intensity and is not dominated predominantly by the fast component, a prerequisite for accurate dating. To overcome these limitations, we started developing a novel measurement protocol. This protocol can be struc-

tured as a sequence of steps aiming to become routine in the context of OSL dating of mortars.
If the material is unaffected by the presence of other mineral phases besides quartz, a specific protocol with pre-determined measurement parameters, including preheating temperatures, duration, and stimulation time, should be thoughtfully considered. This step must be constructed *ad hoc* for each specific sample.
These attributes introduce substantial complexities when applying the Single Aliquot Regeneration (SAR) protocol routinely. It becomes evident that the tests outlined in the protocol often prove inadequate for the initial selection, underscoring the necessity for additional criteria. The criteria we propose are focused on the shape of the curve and the raw signal characteristics, based on statistical analysis.
The choice of skewness and kurtosis values as rejection criteria was somewhat arbitrary, derived from the extremes of the OSL decay curves, i.e. an ideal OSL curve and a flat OSL curve. This particular exception was obtained through simulations. However, another objective of this study was to underscore the potential of skewness and kurtosis as novel additions to the acceptance criteria for OSL decay curves. The descriptive statistics we've chosen represents just one possibility for exploring curve shapes. Numerous other statistical indices remain available for further investigation. It is our conviction that these analyses, including methods like Residual Distribution Analysis (RDA) on raw natural signals, could serve as additional filters and criteria for rejecting unsuitable aliquots.
To further advance our methods, we must strengthen our approaches with new studies and research. Furthermore, it would be wise to establish new benchmarks for the physically meaningful skewness and kurtosis of our data.
Building on the aforementioned steps, the final phase involves statistical analysis, which can be performed using conventional method (e.g., average and weighted average) or tailored techniques like age models. Achieving an agreement among the results obtained in this phase serves to validate the choices made earlier.
Although not exhaustively explored in this thesis, there is a hypothesis that selecting the appropriate region of interest within the signal integral, whether late or early, could potentially benefit from the deconvolution of OSL curves.

Parameters such as the percentage of each OSL component to the overall signal and the distribution of resolved equivalent doses for each component are promising. Such an approach would lead to a different distribution of Equivalent Dose values.
In summary, we can delineate five fundamental steps to follow in mortar dating:

1. Measurement of stimulated luminescence signals within the framework of a specialized protocol, including the determination of measurement parameters like preheating temperatures and duration, stimulation time, and more.

2. Selection of the appropriate signal interval and its integration with background subtraction.

3. Construction of a dose-response curve.

4. Calculation of the equivalent dose (ED) and the assessment of associated uncertainties selecting predefined rejection criteria.

5. Statistical Analysis, employing various age models, to arrive at a conclusive understanding of the results.

The proposed path is easily identified in the figures 7.1 and 7.2. As shown, statistical analysis can be included in steps 2 and 4.

To conclude we think that building an international database of mortars OSL decay curves could serve as a primary solution for comprehending which curve characteristics warrant analysis. We believe that the use of machine learning algorithms can represent a fundamental step forward in the selection and analysis of mortar dating methods. This study should be regarded as a step in check whether statistical processing can effectively mitigate the error introduced by do not knowing the characteristic of the bleaching phase.
The initial results are encouraging. We want to stress out that they were obtained from a limited number of aliquots that did not have statistical significance following the selection process. Therefore, it is our firm conviction that our efforts should be redirected towards expanding the cohort of mortars subjected to this method. This expansion should be complemented by a deeper

exploration of the benefits associated with deconvolving the raw OSL signal. First and foremost, a thorough investigation of the benefits derived from deconvoluting the raw OSL signal must take precedence. With this in mind, we maintain a strong conviction that our primary focus should shift towards be redirected towards expanding the number of mortars subjected to this method.

Part II

Vitrified Forts

9 Story of a vitrified enigma

The term ”vitrified forts” denotes the remnants of ancient stone fortifications, wherein the individual rock fragments and boulders composing these structures have undergone a process of fusion and bonding due to intense heat, seemingly occurring on-site (an example is shown in figure 9.1).

The enigma of the vitrified forts has tickled the curious, stimulated speculation as well as held a certain fascination since the late 18th century. However, it is in the Scottish lands that the most significant chapters of this historical investigation take place. Without a doubt, the landscape of the northern British peninsula claims the highest concentration of vitrified forts in all of Europe. The startling revelations emerging from this research have consistently captured attention and ignited deep reflection since the first reports of these sites emerged. John Williams, a mining engineer charged with surveying properties confiscated in the wake of the 1745 Jacobite rebellion in the Scottish High-

Figure 9.1: Two examples to understand what vitrified forts are:
a) Vitrified rock at Dunagoil fort, Scotland. Photo credit: Rod Collier
b)The hillfort Broborg. The photograph is from Sjöblom et.al article. It was made available by Riksantikvarieämbetet (The Swedish National Heritage Board) [100]

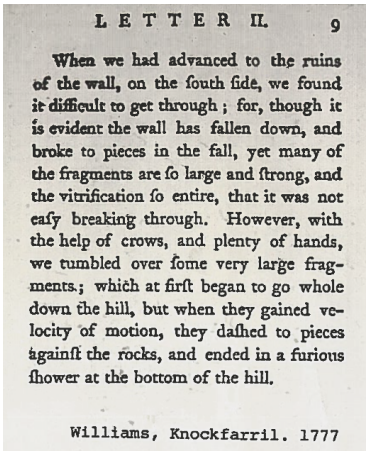

LETTER II. 9

When we had advanced to the ruins of the wall, on the ſouth ſide, we found it difficult to get through; for, though it is evident the wall has fallen down, and broke to pieces in the fall, yet many of the fragments are ſo large and ſtrong, and the vitrification ſo entire, that it was not eaſy breaking through. However, with the help of crows, and plenty of hands, we tumbled over ſome very large fragments; which at firſt began to go whole down the hill, but when they gained velocity of motion, they daſhed to pieces againſt the rocks, and ended in a furious ſhower at the bottom of the hill.

Williams, Knockfarril. 1777

Figure 9.2: Extract of Williams' letter in 1777

lands, gave a first description of vitrified forts. He described the many forts in the Inverness area in a letter, and what he saw left him in deep incredulity (see figure 9.2).

It was Williams himself who took the initial samples, and upon examination, they struck him as a blend of molten material conjoined with glassy or partially melted rock. At first, the idea of fire as a binding agent was discarded. For a long period of time, the idea of these materials being fused together without the aid of conventional cement did not find widespread acceptance. It took similar cases to give credence to Williams' observations.

During the 1820s, the Scottish Highlands and their captivating landscapes, including the enigmatic vitrified forts, became favored destinations for the grand tours. Consequently, the Scottish forts captured the interest of more erudite minds. The theses supporting the deliberate use of fire solely for vitrification gained prominence and remained prevalent throughout the 19th century. However, alternative theories, such as fire serving as a signal of impending attack or resulting from rituals or domestic fires, especially in light of new discoveries, persisted and were not entirely discarded.

> *In the month of September last (1826), when becalmed in my cutter in the Kyles of Bute, I accidently landed on the most northerly of the*

> *Burnt Isles, a small group that stretches across the Kyle or narrow channel between Bute and Argyleshire. From the appearance of a ridge nearly covered with turf, I imagined at first that kelp had been formerly burnt here, but on examining it more narrowly I discovered that it was caused by the remains of a vitrified fort* [101].

Here is reported the first official documents on vitrified forts from James Smith, a member of the Royal society of Edinburgh, on his Notice of an undescribed Vitrified Fort, in the Burnt Isles, in the Kyles of Bute.

In the last year of 19th century, the questions surrounding vitrified forts continued. Fresh excavations yielded new discoveries and unearthed additional sites. However, the primary doubt persisted: understanding the purpose behind the construction of these enigmatic walls. Observations also began to unveil variations in their constructions. While some forts exhibited vitrification solely in their interiors, others showed it exclusively at their bases. Meanwhile, sites like Arka Unskel show extensive vitrification extending over walls towering more than 2 meters high. In Aberdeenshire, a different pattern emerged, with only vitrified blocks scattered among the findings.
In 1898, Christinson catalogued the forts that had been identified at that time. The count stood at approximately 50, and more were yet to be uncovered. Notably, discoveries from France and Germany contributed to the growing of knowledge [102]. However, doubts about their origin still remain, laying a veil of mystery over these ancient walls.

Careful observations ultimately revealed that the distinguishing feature of the vitrified forts was a complex mix of partially molten rock fragments, bonded by other fused and entirely vitrified components. Additionally, clear evidence had already emerged, affirming the presence of both wood with impressions of poles and charred wood within these walls.
The initial systematic investigations were undertaken by M'Hardy, who in 1906 relayed his findings to the Royal Society [103]. His pioneering analyses initially suggested that the vitrified materials and their source rocks shared a common origin, marking a crucial point in the search for answers. This exploration was primarily concentrated near Arisaig (NE from Glasgow), where the placement of vitrified sections appeared to align with the positions of neighbouring forts, forming a visual connection. M'Hardy advance a theory that these vitrified areas may have functioned as locations for beacon fires, serving

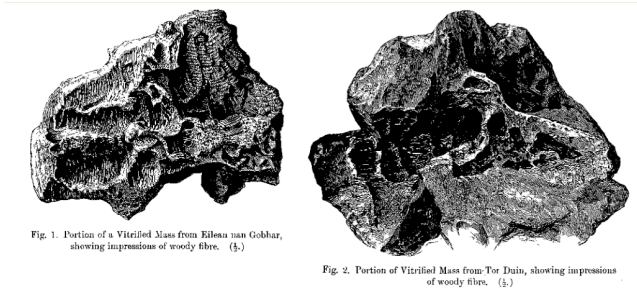

Fig. 1. Portion of a Vitrified Mass from Eilean nan Gobhar, shewing impressions of woody fibre. (½.)

Fig. 2. Portion of Vitrified Mass from Tor Duin, shewing impressions of woody fibre. (½.)

Figure 9.3: Drawings of M'Hardy's report to Society.

as a means of communication between disparate forts, and potentially leading to the phenomenon of vitrification.
Consequently, numerous experiments were conducted in an effort to replicate vitrification under open-air conditions. However, despite varied fuel selections, including straw and peat, as well as adjustments to ignition methods and exposure durations, the desired vitrification remained difficult to reach in open-air settings. It became evident that true vitrification could only be achieved through the deliberate restriction of ventilation and control over the burning rate. Even then, after a 18-hour process, only a small portion of the material was vitrified. Thus "warning fire" was discarded as a motivation.

In 1927, an article in Nature unveiled fresh insights into the vitrified forts of Buteshire, situated 70 kilometers west of Glasgow. This article, authored by an unknown researcher [104], asserted that both the contents within these forts and the forts themselves were undeniably pre-Roman in origin.

The pioneer in comprehensively exploring vitrified forts was Professor Childe, from the University of Edinburgh. Between 1934 and 1937, Childe starts an extensive investigation at the Finavon Hill site, located 80 kilometers south of Aberdeen. During his inquiry, a fortification wall was unearthed, displaying structural damage. By looking the mineralogical phases discovered, Childe's investigations succeeded in establish, for the first time, the temperature range of vitrification, between 1100 and 1500°C.
In the meanwhile, another site under investigation, Rahoy, exhibited continuity of vitrification, even within the rocks themselves. Childe and his colleagues achieved a milestone by successfully reconstructing an authentic vit-

rified fort. They constructed this model using rocks found in proximity to the excavation site and incorporated visible wooden poles. In 1937, Childe and Thorneycroft ingeniously replicated the effects of vitrification [105–107].
Later on, samples underwent a series of focused and meticulous analyses. Atomic absorption analysis unequivocally confirmed that all examined samples utilized locally sourced rocks that were then subjected to vitrification [108]. Mineralogical analysis corroborated that the achieved temperature range fell within 1100-1150°C. Notably, at 1200°C, the evidence illustrated that the samples had indeed melted. These findings lent substantial support to the validity of the construction model, which relied solely on rocks and timber.
As the culmination of research spanning from the early half of the century to the 1970s, a prevailing theory emerged: vitrified forts represented an alternative method of fortification construction. These structures were no longer perceived as planned constructive or destructive processes but were, in essence, precursors to the timber-framed walls employed during assaults.
In the following years, the debate on vitrified forts was revitalized, fuelled by studies conducted on Swedish forts [100, 109]. The arguments advanced in this discourse were effectively condensed into three plausible theories:

Incidental Theory: the vitrified material found in these forts could be the result of using volcanic lava or pumice in construction inadvertently. Alternatively, vitrification is perceived as an unintended consequence arising from activities such as signal fires, bonfires, fireplaces, or forges.

Constructive Theory: It suggests that deliberate efforts were made to create vitrification. This involved mixing appropriate rocks with a molten substance, such as wood or coal, and subjecting them to intense heat. This process might have occurred on-site or within purpose-built furnaces, with the resulting vitrified material being utilized to fortify the ramparts. The primary motive behind this approach was to enhance the structural integrity of the fortifications, thus making them more robust.

Destructive Theory: these forts featured walls lined with wood that were set on fire, either by adversaries during war or accidentally, perhaps due to a lightning strike. Under specific conditions, the ensuing conflagration generated enough heat to melt the building material. The outcome of

this unfortunate event was the partial, if not complete, destruction of the fortification.

In sum, the debate continues to center around these three intriguing theories, each of which offers a unique perspective on the origin and purpose of vitrification. The enigma surrounding this phenomenon continues to lack a definitive solution, and researchers remain actively involved in the search for answers. The study remains vibrant and ongoing, with examination of newly discovered highly vitrified structures extending to southern regions of Europe [100, 110–113].

Not only the scientific world, news of this mystery has also spread to news outlets such as articles write on National Geographic [1] and the BBC [2].

9.1 Dating the Vitrified Forts

Opinions regarding the dating of vitrified forts underwent a transformation with the acquisition of new information. Prior to M'hardy's contributions, these structures were classified in an ambiguous "Pre-Roman" British era. Childe's exhaustive work subsequently led to the belief that all fort walls were erected by 200 BC, subsequently used for defence against the Roman incursion during the conquest of Gaul (58-50 BC). This attribution relied on comparisons with objects discovered near the excavation sites. Interestingly, many of these objects were subsequently reclassified from the British Bronze Age, further altering the age estimations for the construction of vitrified forts.

The initial attempts at dating the forts directly involved the utilization of the radiocarbon method. However, uncertainties and doubts afflicted these early efforts, such as calibrating the radiocarbon timeline and determining the amount of radiocarbon present in such ancient times. Notably, during the early years of radiocarbon surveys, the technique was not yet fully understood.

Here, the significant work of Professor David Sanderson comes into focus. His analysis of vitrified forts employing thermoluminescence played a

[1] https://www.nationalgeographic.com/history/article/160303-archaeology-history-forts-vitrification

[2] https://www.bbc.com/news/uk-scotland-highlands-islands-43813824

pivotal role in advancing and comprehending this technique [3, 30, 31]. His research assumed that the walls were constructed by individuals employing combustible materials within the structural framework, with vitrification being a consequence of fire. This utilization of fire and wall framing was likely an outgrowth of Celtic building traditions during the Bronze Age.

To determine the age, TL dating employed a variety of methods, including quartz extraction, feldspar analysis, and the fine-grain method. An initial and noteworthy observation comes out: the samples exhibited anomalous fading—an intriguing phenomenon with implications for signal loss, which will be explored in more detail in a subsequent discussion. Remarkably, the findings from Scottish sites exhibited internal consistency, and revealed a significantly extended temporal range. [114–117].

Alternative methods for dating have been tried on the vitrified wall at the Misericordia, Serpa, Portugal, Late Bronze Age site. A pioneering study on archaeomagnetic dating is presented. Archaeomagnetism is a dating method that relies on the magnetic properties of materials to establish their age by following changes in the Earth's magnetic field over time. The absolute date 842-652 BC fits very well with the known chronology for the second phase of the Late Bronze Age south-west. This study remains one of the few attempts to date with archaeomagnetism on vitrified forts [118]. Research into the thermoluminescence of vitrified material extracted from the ramparts of various site situated in central and western Europe has uncovered discrepancies in the results obtained. These differences prompted a quest to investigate the upper temperature threshold for TL dating of vitrified material, as it is well-established that inadequate heating can yield erroneous TL ages, typically toward antiquity [119, 120]. However, a lesser known and thus yet unexplored territory in this field is the exact temperature range at which vitrification begins.

An examination was undertaken at the Broborg archaeological site. This multifaceted investigation encompassed both petrographic analyses and concurrent TL measurements. The outcome of this comprehensive study has unveiled a notable trend: as the firing temperatures exceeded the 900°C threshold, the determined ages of the vitrified material exhibited a remarkable pattern of becoming progressively younger. This intriguing correlation underscores a pivotal discovery – the lower the apparent age of the sample, the

higher the proportion of glass content within it.
In essence, this groundbreaking research offers invaluable insights into the relationship between firing temperatures and TL dating outcomes for vitrified materials. It illuminates the crucial role played by the temperature at which vitrification starts, and highlight the complexity of TL dating in archaeological contexts marked by vitrified material [121].

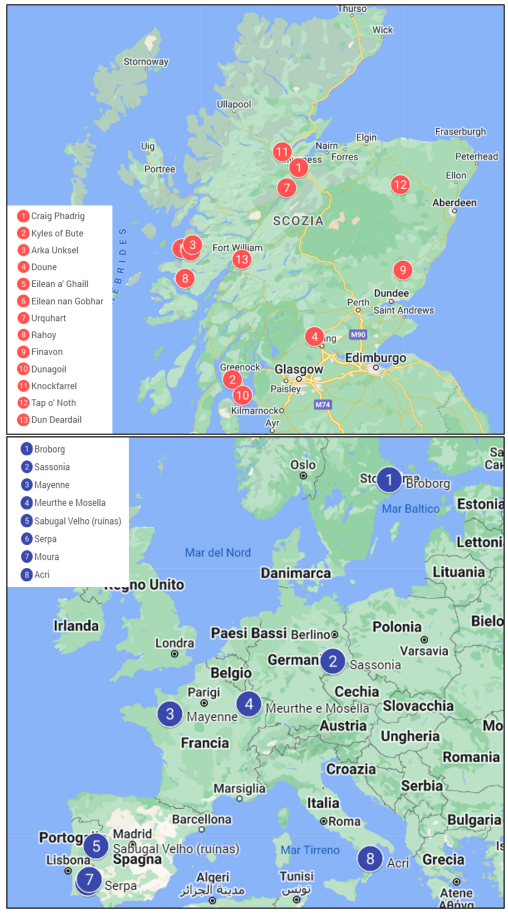

Figure 9.4: Map of the major vitrified forts of Scotland and Europe

10 Dating glassy material

Thermoluminescence (TL) dating of glass has encountered a significant challenge. The necessary conditions for successful application, including strong luminescent sensitivity and signal stability over time, are related to the specific energy level structure found in insulating solids or semiconductors. Unfortunately, this structure does not adapt well to the disordered and amorphous structure of glass.
However, exploring the dating of glassy materials has always been a interesting line of research. Glass is composed mainly of silica (SiO_2), a form of quartz. In addition, throughout its history, glass has been subjected to treatments that have reset the TL and OSL traps, essentially setting them back to zero. This resetting event, along with the ability to store radiation, makes glass ideally suited for luminescence dating techniques.
Nevertheless, it is important to note that the amorphous nature of glass presents a challenge for dating.

Archaeological artefacts often include glassy materials, that makes their dating useful for reconstructing site history. In addition, understanding the evolution of glass production technology would improve our understanding of different cultures. Numerous attempts to date glassy materials have often given disappointing results [114, 122]. Various methods have been employed to attempt to date glass. These include the extensive TL studies on volcanic glass conducted by Berger in the 1980s. Unfortunately, because of substantial analytical errors, up to 20-25%, due to intensity, anomalous fading, and poor inter-aliquot reproducibility, this attempt was abandoned [123]. Recently, promising research has rekindled interest in this study area [124].

The most encouraging breakthroughs in glassy material dating have been observed in the study of mosaic tiles [125–128]. Mosaic tiles have shown in-

creased sensitivity to TL and linear growth. This better dosimetric performance, compared with normal glass, is believed to be related to the presence of chromophore ions [128].

Recently, contemporary retrospective dosimetry studies are increasingly considering glass components as potential tools for measuring incident radiation [129, 130]. Various methodologies have been formulated to estimate hypothetical doses of commercial glass, and some have been applied to cultural artefacts as well [131]. One successful approach, *Pre-bleached with blue LED*, isolated the most thermally stable TL signal whatever the nature of the glass. This allowed fading curves to be determined for each sample analysed, taking into account the anomalous fading and light sensitivity typical of ancient mosaic tesserae TL signals [130, 131].

10.1 Anomalous fading

Anomalous fading is an unintentional occurrence that impacts both OSL and TL. It manifests in certain minerals where there is a dependence between luminescence intensity and the time elapsed since irradiation. The term 'anomalous' is used because it leads to the unexpected release of trapped electrons. Specifically, electrons that should remain trapped at room temperature are released sooner than expected, often within a few days. Unfortunately, this renders the trapped electrons unsuitable for accurate dating. Ideally, electrons should remain trapped for at least 20 times the age of the sample.
The significance of anomalous fading in TL dating was first highlighted by Wintle in 1973, leading to the inclusion of anomalous fading tests in measurement protocols [132]. Interestingly, anomalous fading is also observed in OSL, with the defects responsible being similar to those found in TL.
Anomalous fading outcomes vary depending on the time since irradiation but remain consistent regardless of the type of ionizing radiation. Importantly, the presence of anomalous fading does not affect the shape of the glow curve. Consequently, a model based on tunneling mechanisms was proposed to explain this phenomenon [3]. Aitken's 1985 model introduced a logarithmic law to describe the decay of the signal:

$$\ln \frac{T}{T_C} \tag{10.1}$$

Where T_C is an arbitrary time.
The tunneling model was developed using data gathered from feldspars, and it is uncertain whether it can be applied successfully to other materials, particularly glasses, due to their amorphous structure. In essence, the recombination rate is inversely proportional to the time period analyzed T^{-1}, allowing for the description of luminescence intensity as specified by the equation:

$$I = I_C \left(1 - k \ln \frac{T}{T_C}\right) \tag{10.2}$$

Considering this intensity I_c without fading at an arbitrary time (T_C).

When dealing with archaeological materials, it is crucial to consider that they are continually exposed to natural radiation, and the absorbed dose exhibits a proportional relationship with age. However, by integrating equation 10.2 it is possible to establish T as the true age in contrast to T_F, which represents the age of fading:

$$\frac{T_F}{T} = 1 - k \left[\ln \frac{T}{T_C} - 1\right] \tag{10.3}$$

10.2 Pre-bleached with blue LED protocol

The field of accident dosimetry has advanced significantly in recent years due to growing concerns about the potential dispersion of radioactive nuclides into the environment. In this context, having an accurate knowledge of the radiation dose to which a human has been exposed is of crucial importance for administering appropriate medical treatments. This need has driven the effort to find a material that can effectively absorb doses, thus allowing accurate personal dosimetry.
Interestingly, the screens of our cell phones have emerged as good candidates to fulfill this role. Measurement of accumulated radiation dose can be achieved by a number of techniques. One remarkable approach is the pioneering work of Discher and Woda, who designed the already cited "pre-bleached with blue LED" protocol, offering a promising method for quantifying absorbed doses in cellphone's screen [130].

After conducting initial calculations for the zero dose and ensuring the reproducibility of the signal shape, the dosimetric characteristics of the screens were studied. Woda and Discher observed that the reproducibility of the zero dose signal began impossible after the first thermoluminescence cycle. Moreover, the signal displayed anomalous fading, as described by Huntley [133], persisting beyond 200 °C, which is typically where the most stable traps are expected to occur over time. The study of the portion to be integrated is done with a fitting of the curve. The fit was a generalized hyperbolic function to the pre-bleached TL data. The fit equation is the following number 10.4.

$$y(t) = \frac{a}{(1 + b \cdot t)^c} \tag{10.4}$$

In light of these challenges, it is important to isolate the most stable portion of the signal and mitigate fading. The innovative "pre-bleached with blue LED" approach involved g the samples subjected to 500 seconds of blue light, which not only corrected for the influence of both the screen's own light and ambient light, but also allowed to isolate the most stable segment of the curve. Consequently, this method enabled to conduct dosimetry studies exclusively on the components that were difficult to bleach.
The entire protocol is shown in figure 10.1, where the thermoluminescence growth step can be repeated several times.

As noted in the section 10, dating glassy materials presents significant challenges. However, the "pre-bleached with blue LED" procedure offers a potential solution to address, or at least mitigate, these difficulties when dating such materials. The article authored by Galli et al. [131] delves into the application of this "pre-bleached with blue LED" technique for dating mosaic tesserae discovered at the *qasr* (winter residence) of Khirbat al-Mafjar, an Islamic caliphs' palace situated in the Jericho plain. Among various glass materials, mosaic tesserae exhibited already promising outcomes in TL dating.
The tesserae undoubtedly underwent fading of their TL signals due to exposure to light. The study successfully demonstrated the efficacy of the prebleaching process in identifying and emphasizing the most stable segment of the thermoluminescence curve. In this specific scenario, the tiles exhibited robust emission characteristics, resembling the continuous energy traps ob-

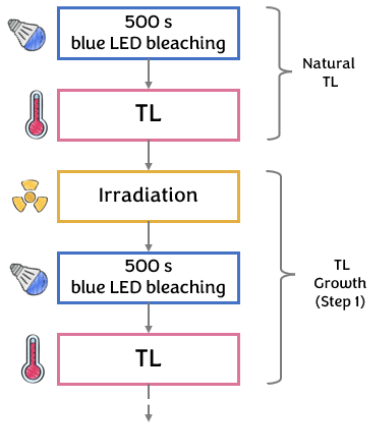

Figure 10.1: Pre-Bleach with Blue LED protocol, the step with TL growth is repeated.

served in the glassy components of mobile phones. Moreover, the samples encountered issues related to anomalous fading, a phenomenon distinct from accidental dosimetry.
In accidental dosimetry, the ionizing event is instantaneous, intense (significantly higher than natural sources), and temporally defined. However, this does not hold true for the dose received from cultural property samples. Managing the loss of anomalous signals can be recovered by determining the elapsed time interval. Nevertheless, this study achieved favourable results by combining the approach proposed by Discher and Woda with the fading study of feldspars suggested by Huntley [130, 133].
Recalling that archaeological materials are consistently exposed to radiation, it is essential to take into account the conclusion of Huntley and Lamothe on the fading effect [133]. They introduced a concept using the principle of superposition of effects: the influence of one specific source does not alter the impact of other potential sources. Specifically, if it is assumed that the distribution of these sources remains constant within the environment, then the cumulative effect over a defined time period can be consider as the sum of an

indefinite number of individual contributions. This behavior can be mathematically characterized by the equation 10.2. Importantly, it should be noted that $\frac{T_{Fad}}{T}$, $\frac{I_{Fad}}{I}$, or $\frac{D_{Fad}}{D}$ are all directly proportional quantities.
Therefore, the integral of the eq. 10.2 can be used as an equation to calculate the time actually elapsed with respect to the fading time:

$$\frac{T_{Fad}}{T} = \frac{1}{T} \int_0^T \frac{I(T-t')}{I_0} dt' = \frac{1}{T} \frac{A}{B(1-C)} \left[(1+BT)^{1-C} - 1\right] \tag{10.5}$$

This will prove to be the starting point for new applications on vitrified materials.

11 Serravuda's Vitrified Forts

Interest in the vitrified rocks of Mt. Serravuda (926 m.s.l) traces back to as early as 1970 when Prof. Mario Bertolani (University of Modena and Reggio Emilia), in collaboration with dott. Franco Foggia, authored the pioneering article on Italian vitrified forts [134]. This unique geological phenomenon was discovered approximately 3 kilometres north-west of the town of Acri, situated in the province of Cosenza. The region, known as Serravuda or Serra di Buda, is defined by a series of rounded peaks. The presence of an intentionally leveled summit, with a mysterious glassy structure at its forefront, immediately captures attention. Its surface dimensions measure 32 meters from East to West, and 25 meters from North to South, exhibiting a distinct elliptical shape.

The intriguing aspect of this find lies in the fact that the vitrified rocks were

Figure 11.1: in (a) the assumption of the reconstructed wall and how the village was organized, also in section. In (b) the location of Mount Serravuda in the Calabria region. In (c) the reconstruction of the location of the wall in relation to today's excavation. *(Thanks to Prof. Sighinolfi of the University of Modena and Reggio Emilia for photos and material).*

consistently present along the northern perimeter of the flat surface, extending uninterrupted for over 50 meters. Fragments of melted rock are abundant on the hill, particularly on its slopes, while less significant rock alterations from heating can be observed in the central portion. For precise location reference, consult figure 11.1.
Regarding their extension into the ground, a crust with a thickness of at least 50-90 centimeters was discover, beneath which a layer of heat-oxidized rocks extends to a depth of 25-60 centimeters. The molten crust appears as a cohesive monolithic mass, and the larger fragments seem densely compacted upon initial inspection. The entire structure rests upon debris characterized by a blackened surface. Interestingly, at a depth of approximately 1.40-1.50 meters, the rocks stop to exhibit changes in their nature induced by heat.
On the western side of the summit, three wooden crosses were discovered, likely signifying the presence of a sacred area within the settlement. Notably, these vitrified rocks are conspicuously absent on the southern side of the summit.

An excavation conducted in this area yielded pottery fragments dating back to the *Brutii* settlement, an ancient Italic people who undoubtedly inhabited the region during the 2nd-3rd centuries BC of Indo-European origin, the Brutii are part of all the populations later defined as Italic. Their name finds its origins in Brettia, the pioneering woman who led an army. This fearless warrior led her people in a triumphant revolt against the Greeks, during which all neighboring tribes united in a league. In commemoration of this alliance, they established the city of *Consentia*, *"Consensus"*, which would become present-day Cosenza. Throughout history, the Brutii have been remembered as a people of remarkable strength and martial prowess, motivated by an irrepressible desire for freedom. Even in Roman times they rebelled several times against the usurper. They were defeated a first time by the Romans in 275 BC and completely subjugated in 270 BC. Twice they attempted to rise against their oppressors, once aligning with Hannibal and later joining forces with Spartacus.They were only granted Roman citizenship in 29 BC, after their last uprising.

Several years following the initial identification of this geological formation, the Department of Geosciences at the University of Modena-Reggio Emilia has started a new investigation. This effort seeks to address a crucial question:

were these rocks intentionally vitrified by human activity, or was their transformation a result of a natural phenomenon?
If indeed attributed to human activity, the research will focus on understand the precise mechanisms behind the heating process.

From a geological perspective, the Sila plateau, where Mt. Serravuda stands, is primarily composed of granitoids. The wall structure exhibits a varied lithological composition, with a combination of debris and rocks bound together by vitrified cement. Conversely, at the center of the area under examination, migmatites were found, which also belong to the granitoid family. On the slopes, gneisses and amphibolites are present.
In terms of rock composition, all the rock fragments that have undergone heating exhibit a similarity to the parent bedrock. The consequences of this heating event exhibit a spectrum of outcomes, vary from simple oxidation reactions causing surface, complete reddening of rock fragments to their partial, or near-total melting resulting in the formation of glassy cement.
A noteworthy discovery in most of the heated samples is the presence of newly formed mineral phases such as mullite, cristobalite, tridymite, hercynite, and magnetite. These phases are closely associated with the mineral reactions triggered by the application of high-temperature heat ($\geq$ 1200°C). In the case of hypersilica rocks, particularly quartzite pebbles, it is plausible that cristobalite may have originated from quartz during solid-state transition reactions. These reactions can lead to substantial melting of the initial material even at relatively moderate temperatures, typically in the range of 900-1000°C. This phenomenon may provide an explanation for the substantial volumes of glassy materials observed and the prominent presence of mullite in the Serravuda samples.
Historical records suggest that the mountain might have had volcanic origins. Furthermore, there exists historical evidence of a significant fire that occurred in the area during the late 17th century.

11.1 Analyzed Material

The materials examined in this study were gathered during two field expeditions conducted in 2018 and 2019 at the Department of Geoscience (UniMoRe).

These materials can be categorized into three distinct types:

- *Substrate Rock*: These rocks possess a whitish to light-colored aspect and are characterized by their composition of migmatoid rocks, comprising quartz, plagioclase, and granitoid minerals.

- *Rock Fragments*: These fragments exhibit a dark-black, vitreous (glassy) aspect. It comprise a variety of materials, including samples showing surface reddening and minor internal fracturing, as well as samples that have undergone intense heating, resulting in significant alterations. The lithologies of these rock fragments display an extremely diverse range, reflecting those of the underlying metamorphic crystalline rocks. They can be further classified into two distinct origin groups: one from of loose fragments, and the other sampled from cemented blocks.

- *Vitreous cement*: These show unique morphological features as prominent veins measuring between 5 to 10 centimeters. They are responsible for the cementation of rock fragments. Within this category of materials, there are a densely black glass with minimal bubble inclusions, or a pumice glass with abundant crystalline inclusions. Both of these materials have plagioclase and quartz inside.

Chemical and mineralogical analysis

The composition of the rocks within the vitrified body generally aligns with the characteristics of Mount Serravuda's rocks. The chemical and mineralogical analyses performed were scanning microscope observations (SEM), mineral composition analysis by X-ray powder diffraction (XRPD), and mass spectroscopy analysis in University of Modena and Reggio Emilia laboratories.
Consequently, it was found that the rocks on top of Mount Serravuda have a granitoid origin with a high alkali content, whereas the rocks on the flank are notably rich in iron. Upon a detailed chemical analysis of major and trace elements, the rocks exhibited a remarkable compositional homogeneity.
The chemical- mineralogical data for the substrate rocks in the Serravuda area suggest two primary chemical source systems among the samples under analysis:

1) A hypersilic system (quartz >70-80%, feldspar + felsic phyllosilicates 20-30%)

2) A granitoid system (quartz <70%, feldspar Na + felsic phyllosilicates 30%).

Some rock fragments analysed were chemically and isotopically indistinguishable from the granitoid rocks supporting Serravuda's vitrified structure. However, the vitrified cements were rich in strontium and iron, with the iron content determining rock characteristics like compactness, presence of bubbles, crusts, and veins. Additionally, the presence and percentage of rare earth elements (REE) were distinctive for the samples, highlighting the contrasting compositions of the substrate rocks and rock fragments within the vitrified structure. The rock fragments that constitute the structure exhibited much more variable REE contents.

A significant challenge in comprehending the data from this study, and consequently in formulating hypotheses about the nature of the heating event responsible for the rock vitrification, stems from the limitations of the analytical methods employed. These methods provided information solely about the overall mineralogy and chemistry of the vitrified rocks, without revealing insights into the individual mineral phases present within the vitrified material. This limitation does not allow the quantitative discussion of the reactions of mineral phases that occurred during the high temperature heating event, making it challenging to identify the reactants and products involved in specific reactions.

Another issue arises from the marked heterogeneity observed among the heated rock fragments. This variability limits the ability to make precise assessments of the actual melt rate and its composition, which raises questions about the controllability of the heating process.

To deduce the temperatures reached during the heating of Serravuda rock, the presence and relative abundance of high temperature siliceous phases can be observed. For instance, in the case of Serravuda, the presence of cristobalite can provide some indications of the maximum temperatures achieved during the heating event. In fact, verification for the presence of high-temperature forming phases such as cristobalite, mullite, corderite, and hercinite lead to the conclusion that the material definitely reached temperatures around 1000-1100°C.

On the other hand, observations with an optical microscopic led to the categorization of outcrops on the hilltop into two distinct groups:

(a) The first group comprises samples that *have never been subjected to a sufficiently high temperature* during the heating process to induce significant melting. Consequently, they exhibit extensive macro or micro fractures and deformation, along with noticeable surface reddening caused by oxidation reactions, which are visible to the naked eye. These samples all belong to the hyper silicate chemical group, as mentioned earlier, and after heating they essentially retain the mineralogy of the initial materials.

(b) The remaining analysed samples not only suffered from the previously mentioned dynamic effects, such as intense fracturing and macro-micro fracturing, but also underwent alterations in the rock structure. During the heating process, a series of mineral phase reactions occurred, resulting in a mineral composition different from that of the starting materials. These samples, *subjected to various degrees of partial melting*, fall within the chemical domains of granitoid group, with a predominance of phyllosilicates.

To conclude: The mineral composition of the Serravuda samples suggests they originated locally from granitoids, amphibolites, and gneisses. The minerals identified were used as indicators of geothermal conditions. The XRPD results obtained from partially vitrified samples imply that the heating temperature did not go above 1100°C. The mineral combination of these partially vitrified rocks, in conjunction with the glassy material, indicates that the fort's walls were constructed using slabs derived from nearby metamorphic rocks, with the addition of granitic rocks to enhance both the structural strength and insulation of the fort's walls [113].

11.2 Origin discussion

The vitrified fort at Mount Serravuda could be a product of the period characterized by the rapid development of defensive fortifications in various regions of Sannio, Lucania, and Bruttium during the late Iron Age, specifically in the

5th-4th centuries BC. Many of these fortifications were built in response to the tumultuous and unstable period that preceded the Romanization of Italy [135].
However, following the investigations carried out and reported in the section 11.1, it is good to discuss and summarize three points before adding the thermoluminescence data: the transport of the rocks, the purpose behind the structure's construction, and the process that led to vitrification.
Regarding the origin of the rocks, petrographic data has revealed they originated from the hill flanks. The size should not have been prohibitive for transportation. It is likely that these rocks were already in the form of debris due to natural weathering. Once collected, they were transported a few meters in distance and also in height.

The purpose behind vitrification and the construction of the wall has been a subject of extensive debate. Initially, one hypothesis suggested that these rocks were slag or remnants from pottery kilns. Another theory advance that they were residues of metallurgical activities for alloy production. The first hypothesis was supported by the discovery of Bronze Age pottery at the summit of the mound. However, the pottery kilns hypothesis is unlikely due to the absence of suitable clay deposits in the surrounding areas. Only kaolinites are present, but not at volumes that would suggest that an organized and repeated activity could have taken place in the area. The hypothesis is therefore to be discarded not only because of the scarcity of source material but especially because of the size of the vitrified rocks. Moreover, the lack of significant concentrations of elements like zinc, cobalt, nickel, copper, and cadmium rules out metallurgical activities. Therefore, the prevailing hypothesis leans toward the structure serving as a defensive fortification. This conclusion is strengthened by the fact that its arched shape naturally provided a strategic advantage. "Wall circuses," characteristic of the Iron Age in Italy, but starting before, including the southern regions, were known in the area. If this hypothesis holds true, it is noteworthy that among the defensive fortifications in Italy, including the subalpine regions, Serravuda stands out as the only fortified structure to undergo vitrification, affecting both its external and internal surfaces.

Regarding the source of heating, various hypotheses have been proposed, encompassing both natural and extraterrestrial possibilities. These include

that the heating could have resulted from a forest fire, a lightning strike, or even an extraterrestrial event like a meteorite impact. However, recent findings from the study conducted by Elmi allow us to dismiss the possibility of forest fire as the cause [113]. The temperatures generated by even an extensive fire would not have been sufficient to produce the mineralogical phases observed through XRPD analysis.
The mineralogical phases identified are consistent with changes induced by a lightning strike, particularly considering the presence of quartz microdeformation and the associated temperatures that could have been reached. Nevertheless, it is worth noting that the vitrified rocks are too wide in size to be explained by a single lightning strike.
The meteorite hypothesis, while not definitively ruled out, gains some credibility from a specific sample (SE6) that raises questions due to the presence of cohesite associated with cristobalite. Cohesite, a rare polymorph of silica, typically forms from quartz subjected to dynamic compression under pressures exceeding approximately 2 GPa. Cohesite is an exceptionally uncommon mineral found in terrestrial materials only within unusual high-pressure metamorphic rocks (eclogites) or as a result of extraterrestrial impacts. In theory, the energy released during lightning strikes can lead to dynamic compression and the formation of high-pressure mineral phases like cohesite. However, it is important to emphasize that further analysis, including additional samples and comprehensive studies encompassing geophysics and mineralogy, is necessary to substantiate this meteorite hypothesis in the Serravuda case. As of now, the prevailing consensus is that the vitrification resulted from human activities, indicating anthropogenic action as the most likely cause.

Uncertainties persist regarding the human involvement in this event. The fundamental question revolves around whether the fire was a deliberate, well-managed act, or if it arose incidentally as a consequence of enemy intrusion and destruction.
Evidence supporting the notion of intentional ignition is apparent in the provided figure 11.2. It reveals distinct marks resembling poles and charcoal within a vitrified block. This discovery leads to the hypothesis that combustible material was intentionally put into the structure and ignited. During the proposed historical period, it is reasonable to assume that the fuel used was either wood or charcoal. However, it's important to note that fossil char-

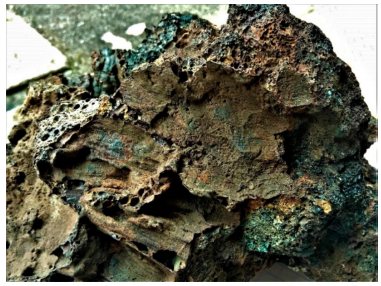

Figure 11.2: A block of vitrified rock, with the imprint of a wooden pole or timber from Elmi et.al. [113].

coal was not available in the Calabria region during that time.
In summary, we can categorize the vitrified forts at Mount Serravuda as the product of a deliberate, controlled human action involving the utilization of wood as the primary fuel source. The findings at Serravuda are very similar to those discovered in European vitrified forts, both in terms of mineral composition and the processes involved. However, what sets the Serravuda forts apart is their unique choice of materials. These materials were transported only a short distance, possibly handpicked for their superior thermal properties, resulting in vitrification at relatively low temperatures. It is not unreasonable to consider this material selection deliberate. However, we lack sufficient information to definitively establish whether the local inhabitants possessed this specialized knowledge.
What is know is that settlements have been present in this area since 4000 BC. Additionally, the discovery of pottery indicates that the hill was regularly frequented. Nevertheless, the dissimilarity between this fortification and the typical ”wall circuses” in the region does not necessarily rule out the possibility that Serravuda was inhabited by people who were not permanent residents. One hypothesis is that a Celtic population, migrating from regions where such vitrified forts are more common, may have encountered and interacted with the local inhabitants. It is worth noting, however, that episodes of such extensive migration are sporadic and often lack documentation, weakening this hypothesis.
To solidify our understanding, further confirmation is required. Thermoluminescence analysis may provide valuable insights and bolster the hypotheses we have put forth thus far.

12 Dating Serravuda's Vitrified Forts

12.1 Material & methods

During the Mt. Serravuda campaign, a total of 24 samples were collected and subjected to thorough analysis. Among these samples, fourteen underwent thermoluminescence dating. Furthermore, the samples were categorized based on their typology (see table 12.1).

Elmi et al. have provided a comprehensive description of the sampling site and a detailed account of the macroscopic characteristics observed in the samples [113].

The unselected samples had to go through a careful, grain size-based grinding process in a stainless steel mortar in order to be prepared for measurements. Figure 12.1 shows how the initial dimensions of the samples can be seen. The entire procedure was carried out in the dim red light of the laboratory.
Grain size selection is necessary due to the characteristics of the instrument used for irradiation and measurement.

Typology	**Sample code**
Substrate Rock	SE9
Heated or partially vitrified rock fragments	SE2, SE6, SE7, SE12,SE13, SV1 3P, SV 4C, SV5, SV6
Vitreous cements	SV 1A,SV 1B, SV 1 3V, SV 4V

Table 12.1: Serravuda's samples analyzed in this thesis

Sample	Sampling location	Lithology	Description
		Substrate Rock	
SE9	NE flank of Serravuda Hill	Gneiss	Reddish, minor fractured, No melting evidence
		Heated or Partially Vitrified Rock Fragments	
SE2	Top hill	Granitoid	Dark, intense fractures, vitreous material
SE6	Top hill	Granitoid	Dark, intense fractures, No melting evidence
SE7	Top hill	Gneiss	Dark,intense fractures, No melting evidence
SE12	Top hill	Granitoid	Dark gray, intense fractures No melting evidence
SE13	Top hill	Quartzite	Reddish, covered by fusion crust
SV 13P	Cement block SV	Granitoid	Light colored, intense fractures, vitreous crust
SV 4C	Cement block C	Gneiss	Black vitreous veins in fractures
SV5	Cement block C	Amphibolite	Dark gray, strongly fractured, No melting evidence
SV6	Cement block C	Amphibolite	Light gray, strongly fractured reddish coating
		Vitreous Cement	
SV 1A	Cement block SV	Glass	light colored, no information on melting
SV 1B	Cement block SV	Glass	Dark, vitreous material
SV 13 V	Cement block SV	Glass	Dark, vitreous material
SV 4V	Cement block c	Glass	Dark, vitreous material

Table 12.2: The sampling site, principal macroscopic characteristics, and the lithological attributes assigned to the studied samples.

The selection was in the interval of < 125 μm, 125-250 μm and 250-500 μm. Figure 12.2 show the samples after the grain selection (125-250 μm). As can be seen from the figure 12.2 macroscopically ground samples have different colours and aspects. Many are dark in colour. All measurements were performed utilizing a Risø TL/OSL DA-20 system, which is equipped with a ^{90}Sr-^{90}Y beta source, delivering an irradiation dose rate of 0.11 Gy s^{-1} (± 3%). For more details of the instrumentation may refer to the section 6.1 .

Thermoluminescence (TL) measurements were recorded at a rate of 2°C/s. To capture emissions, a bialkali photomultiplier tube (EMI 9235QB) in conjunction with a 7.5-mm Hoya U-340 filter, selectively transmitting in the 280-380 nm region, with maximum transmittance (57%) at 330 nm, was employed.

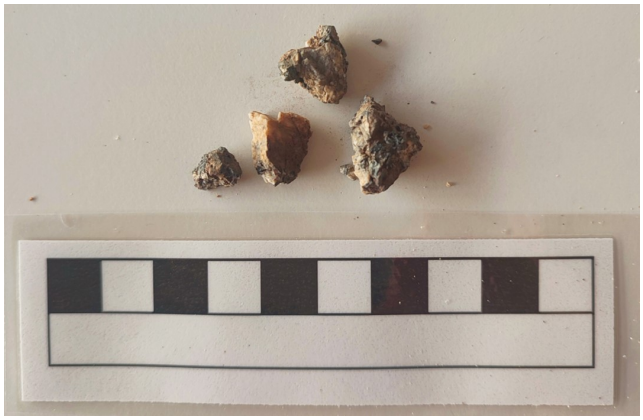

Figure 12.1: Sample size before grain size selection

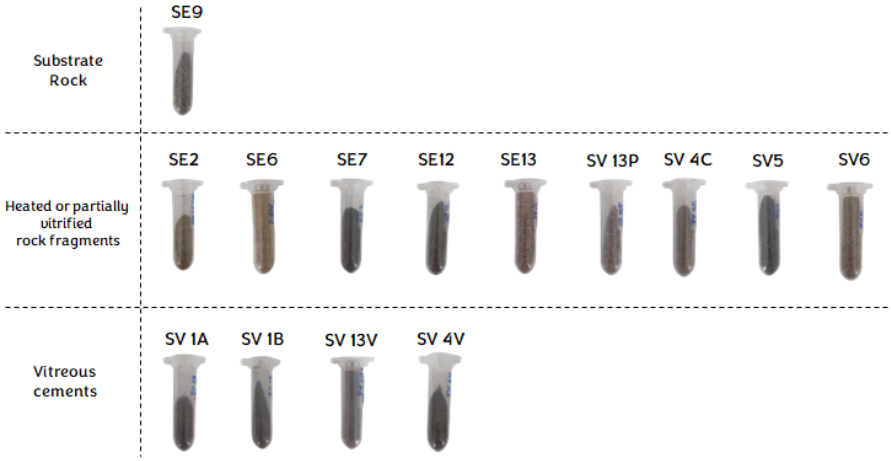

Figure 12.2: Samples analyzed in this thesis selected by grain size and typology.

Sample	Water content (%)	^{238} U (ppm; ± 5%)	^{232} Th (ppm; ± 5%)	^{40} K (ppm; ± 3%)	Internal dose rate (mGy y^{-1}; ± 5%)	External dose rate (mGy y^{-1}; ± 5%)
SE9	7	0.37	20.75	1.21	1.52	0.46
SE2	7	0.06	1.08	1.22	0.83	0.46
SE6	7	0.09	1.03	1.22	0.83	0.46
SE7	7	0.15	0.42	1.22	0.82	0.46
SE12	7	0.26	1.29	1.22	0.87	0.46
SE13	7	0.43	17.32	1.22	1.47	0.46
SV 13P	7	0.19	4.67	1.22	0.98	0.46
SV 4C	7	0.04	0.21	1.22	0.79	0.46
SV5	7	0.14	1.95	1.22	0.87	0.46
SV6	7	0.22	0.39	1.22	0.83	0.46
SV 1A	7	0.37	5.91	2.01	1.53	0.49
SV 1B	7	1.59	12.02	2.01	1.93	0.49
SV 13V	7	0.47	7.94	2.01	1.60	0.49
SV 4V	7	0.27	1.01	2.01	1.34	0.49

Table 12.3: Dose rate measurements' result

The excitation source for illumination was a blue LED array (470 ± 30 nm), with a constant stimulating power of 54 mW cm^{-2}. The determination of the "a" value was facilitated through the utilization of a 37 MBq ^{241}Am calibrated external alpha source, delivered a dose rate of 14.8 Gy min^{-1}.

The Geosciences Department of UniMoRe (University of Modena and Reggio Emilia) conducted a radioisotopes evaluation, assessing the values of ^{40}K, ^{238}U, and ^{232}Th through ICP-MS analysis.
To determine the water saturation level, a sample fragment equivalent in size to figure 12.1 was put in water for 24 hours, then weighed and subsequently dried in an oven before being weighed again. The resulting water content was determined to be 7%.
For calculating the contribution of soil to the dose rate, the average ppm of radionuclides for each category was considered. The external gamma contribution was primarily based on the radioactivity of a 30-cm-diameter sphere centered at the sampling point [3]. This contribution was estimated for each sample by considering its radioactivity and that of its surroundings, using the infinite matrix approximation with updated conversion factors [95]. Additionally, a 0.16 mGy y^{-1} contribution from cosmic rays was included. To view specific values, please refer to Table 12.4. This value is tabulated and derived according to the sample extraction zone [95]

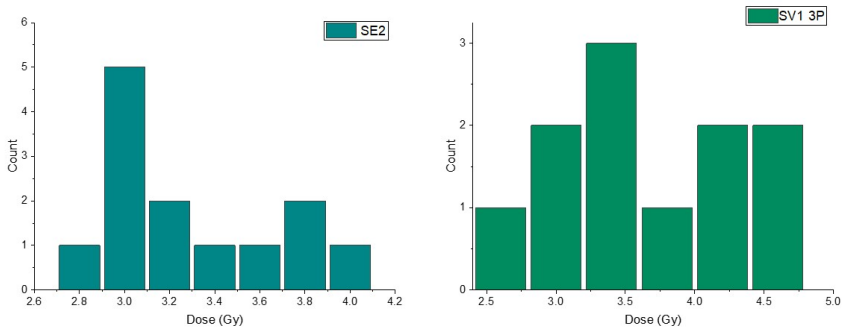

Figure 12.3: ED distribution of sample SE2 and SE13

12.2 Equivalent Dose assessment

To measure the Equivalent Dose (ED), the protocol "pre-bleached with blue LED" was applied as illustrated in chapter 10.2 [130].
The equivalent dose values for the samples fall within the range of 2.7 to 4.3 Gy. However, two samples, SE9 and SE6, exceed this range with equivalent doses of 150 Gy and 136 Gy, respectively. Notably, for all the samples equivalent dose values are consistent with the expected age of the sample.
Furthermore, a distribution of dose values for each sample was constructed. In figure 12.3 is reported the one for sample SE2 and SE13.

The measurement protocol, as outlined in figure 12.4, involved three irradiations at dose of 5.5, 11, and 16.5 Gy, respectively. Signal integration was conducted within the 85-140 channel, corresponding to a temperature range of 150°C to 250°C. Furthermore, thermoluminescence measurements were taken up to 450°C at a heating rate of 2°C/s.

The growth patterns of the curves exhibited linearity across all samples. While, the trends in the glow curves displayed variability depending on the sample's characteristics. In figure 12.5, the glow curve trend for sample SE2 is shown, revealing indications of vitrification. SE13, on the other hand, which was only reddish but was in the same category of heated or partially vitrified rocks.

Sample	Equivalent Dose (ED) (Gy)	Dose Rate (mGy y^{-1})
SE9	150.0 ± 39.0	2.09 ± 0.05
SE2	3.28 ± 0.36	1.41 ± 0.05
SE6	136.0 ± 19.0	1.40 ± 0.05
SE7	2.73 ± 0.06	1.40 ± 0.05
SE12	3.60 ± 0.08	1.44 ± 0.05
SE13	2.93 ± 0.18	2.04 ± 0.05
SV 13P	3.99 ± 0.55	1.40 ± 0.05
SV 4C	4.10 ± 0.28	1.37 ± 0.05
SV5	3.10 ± 0.42	1.44 ± 0.05
SV6	4.26 ± 0.02	1.41 ± 0.05
SV 1A	3.43 ± 1.52	2.12 ± 0.05
SV 1B	4.16 ± 0.34	2.52 ± 0.05
SV 13V	3.50 ± 0.26	2.18 ± 0.05
SV 4V	3.68 ± 0.03	1.43 ± 0.05

Table 12.4: Equivalent Dose (E. D.) and Dose Rate Results

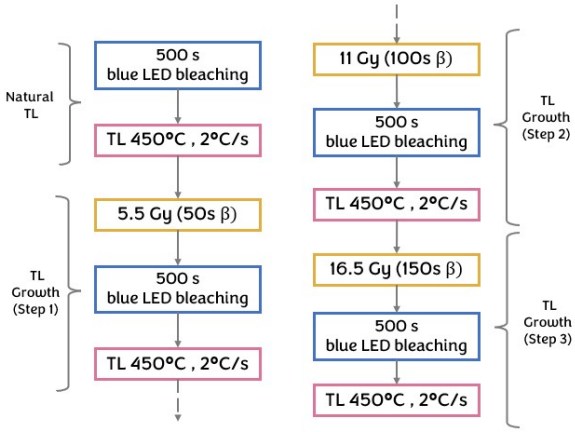

Figure 12.4: "pre-bleached with blue LED" Protocol used on the vitrified forts of Serravuda

Sample SE9, distinguished by a substantial natural thermoluminescence component (depicted in black), stands as the sole representative within the subcategory of substrate rocks.
For instance, sample SV 1A serves as an illustrative example of glass cements' trend.

When examining natural TL glow curves (figure 12.6), five similar trends are identified, two of which were distinct among the heated or partially vitrified rocks. Notably, these trends did not correlate with the presence or absence of heating signs or other background characteristics of the rocks.
In contrast, a comparison of natural TL glow curves associated samples from the same block, such as SV4V and SV4C, as well as SV13V and SV13P. Remarkably, despite their differing natures, SE9 and the two associated samples SV1A and SV1B all exhibited a significant increase of TL natural glow curve after reaching 200°C.

Additionally, using conventional thermoluminescence, we assessed the samples' pattern of glow curves. The steps involved are shown below in figure 12.7. We highlight the comparison between some glow curves of the samples with the "pre-bleached with blue LED" method and a classical thermoluminescence protocol (figure 12.8).

12.3 Fading correction

To address the issue of fading, corrections in the reconstructed archaeological dose data were assessed. The phenomenon and theory were addressed in chapter 10, but for the reader's clarity, the equations and reference steps will be given.
Specifically, only four samples: SE2, SE13, SV13P, and SV5 exhibited fading. It should be noted that not all aliquots showed such pronounced fading.
The correction was implemented using a custom code developed in Matlab.

In the chapter 10, two correction models were presented: the Huntley and Lamorthe model, and the Discher and Woda model [130, 133]. To resume, the former model delineates the luminescence behavior when a sample has been subjected to a single exposure to ionizing radiation within a defined timeframe. This behavior conforms to a logarithmic decay pattern, as illustrated by the equation in 10.2, with the I_C, k, T_C values representing constants deter-

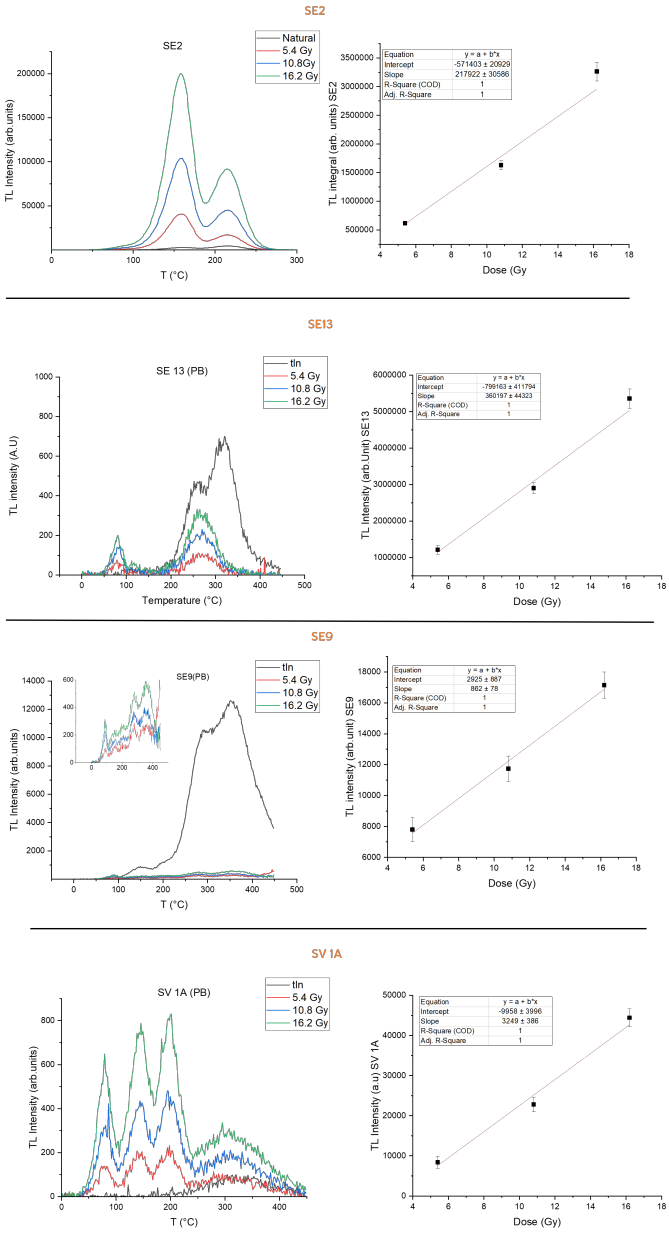

Figure 12.5: TL signal growth as a function of applied beta dose (5.5, 11, 16.5 Gy) for samples SE2 SE13 SE9 and SV1A. Also shown are the curves of TL as a function of imparted dose

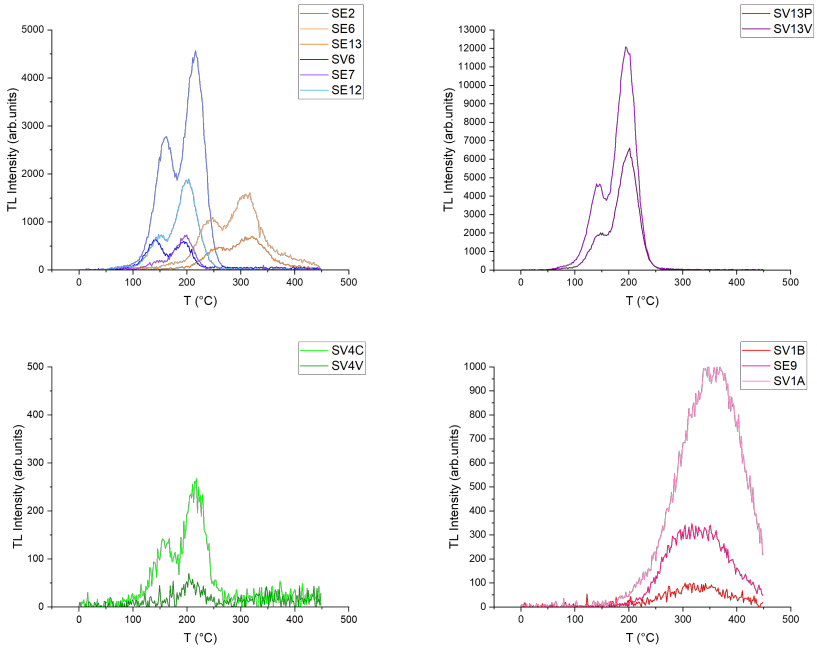

Figure 12.6: Comparison of natural TL curves for each sample typology.

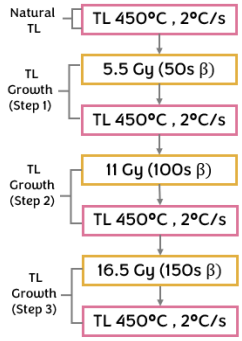

Figure 12.7: TL classical protocol applied for comparison to ”pre-bleached with blue LED”

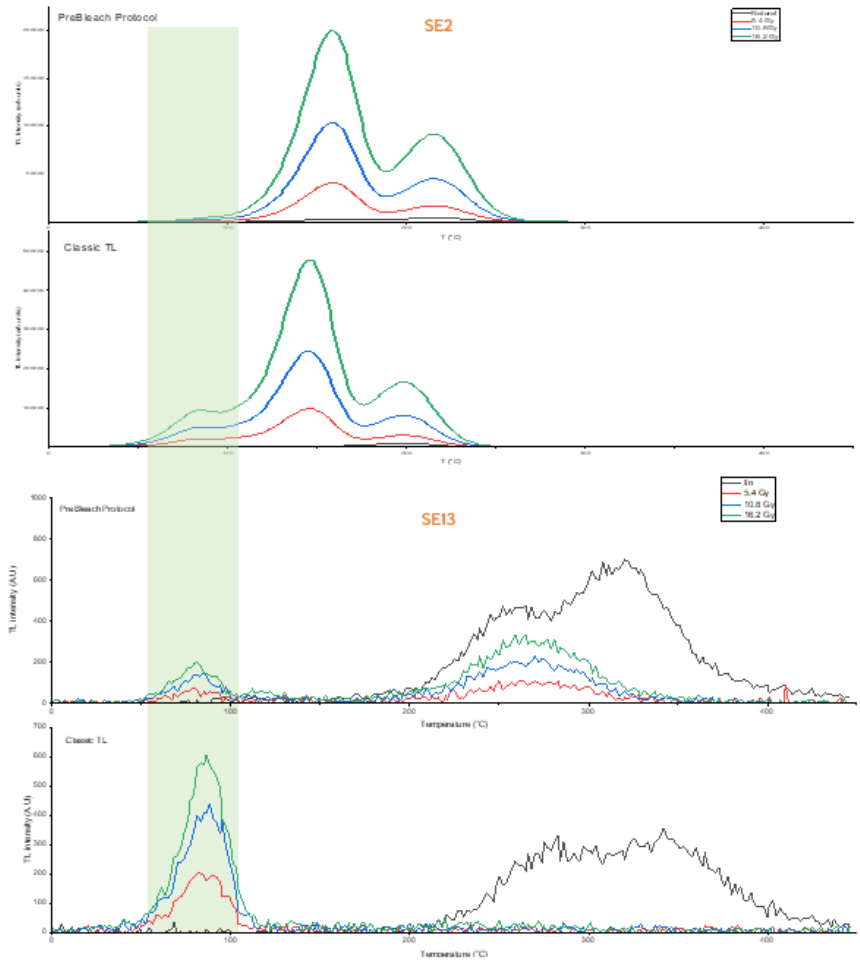

Figure 12.8: Comparison of signal growth curves of samples SE2 and SE13 with the "pre-bleached with blue LED" protocol and a TL protocol. Highlighted the isolation of the most stable part of the signal.

mined through interpolation.

$$I = I_C \left(1 - k \ln \frac{T}{T_C}\right)$$

In this case study, is excluded that exposure to ionizing radiation is isolated to an event, instead is recognized as a continuous process. Consequently, the principle of superposition of effects is considered. This allows to assume that various types of ionizing radiation do not interfere each other. When radiation remains constant over time, each moment can be considered the origin point of a logarithmic decay. Thus, by integrating the Huntley and Lamorthe model equation, the accurate fading-adjusted age can be derived.

$$\frac{T_F}{T} = 1 - k \left[\ln \frac{T}{T_C} - 1\right]$$

It is important to note that this model applies solely to feldspars and is not suitable for amorphous materials. Moreover, its applicability is not exactly valid in cases where t $\rightarrow$ 0 or t $\rightarrow$ to ∞.

Discher and Woda's method is experimental. The data acquired from their study of cell phone displays, involves empirical calculations that yield hyperbolic functions and the obtaining parameters A, B, and C. The effectiveness of this equation is demonstrated in the referenced chapter 10.2 [130].
The final correction approach involves exploring the applicability of Discher and Woda's model to amorphous materials, as demonstrated in the mosaic tiles [131]. However, we still keep to the fundamental principle of superposition of effects illustrated by Huntley and Lamorthe.

In our study, the fading trend was examined for all samples for more than a month and more than an aliquot. The fitting was based on the equation provided below.

$$y(t) = \frac{a}{(1 + b \cdot t)^c}$$

Each part of figure 12.9 show the Equivalent Dose (normalized) in relation to fading time for each sample.

By integrating the normalized dose over time and substituting the A, B, C parameters, the age corrected for fading for the four samples is obtain.

$$\frac{T_{Fad}}{T} = \frac{1}{T} \int_0^T \frac{I(T - t')}{I_0} dt' = \frac{1}{T} \frac{A}{B(1 - C)} \left[(1 + BT)^{1-C} - 1\right]$$

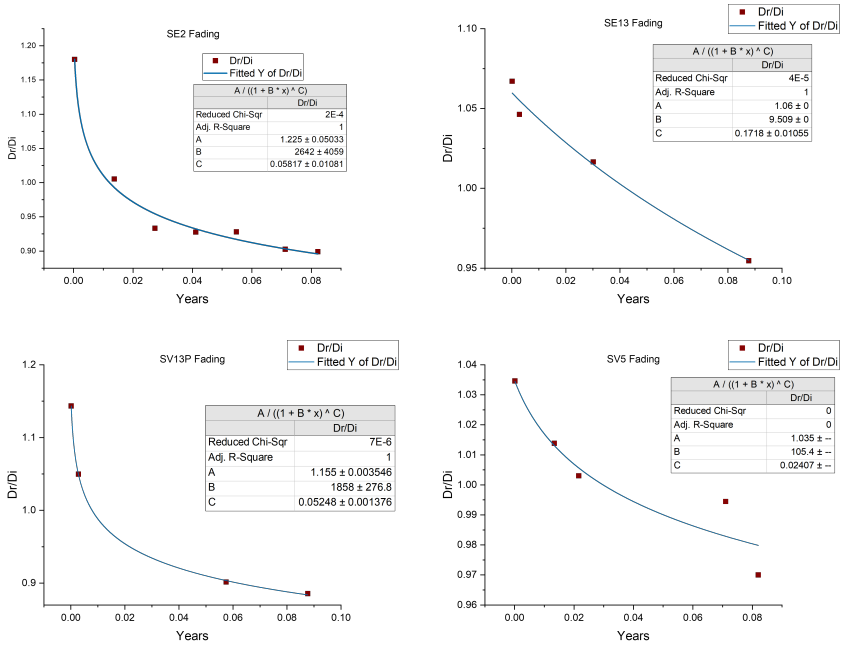

Figure 12.9: Fading curve of samples SE2, SE13, SV13P and SV5. Experimental data are normalized against the imparted dose of 8.25 Gy. The first point is obtained immediately after the first minute, then the first few hours until the 35 days of fading is reached.

12.4 Results & discussion

Aliquots of the samples exhibiting fading were subject to correction through the integration method detailed in the preceding section. This correction effectively recalibrates the initial ages, yielding a range of distinct age adjustments, which are comprehensively tabulated in table 12.5. It is worth noting that not all aliquots present such a strong fading.

After conducting an assessment of Equivalent Dose using "pre-bleached with blue LED" protocol and subsequently calculating the dose rate, we were able to determine the age of the samples by applying the age equation, as show in equation 2.1. Uncertainties in these age calculations were computed in accordance with the principles of error propagation (see table 12.6).

Sample	Apparent Age (Years)	Corrected Age (Years)	Date
SE2	2330 ± 255	4630 ± 510	$2605BC \pm 510$
SE13	1440 ± 90	2670 ± 165	$645BC \pm 165$
SV 13P	2860 ± 395	3860 ± 530	$1835BC \pm 530$
SV5	2145 ± 290	2960 ± 400	$935BC \pm 400$

Table 12.5: Age correction after fading

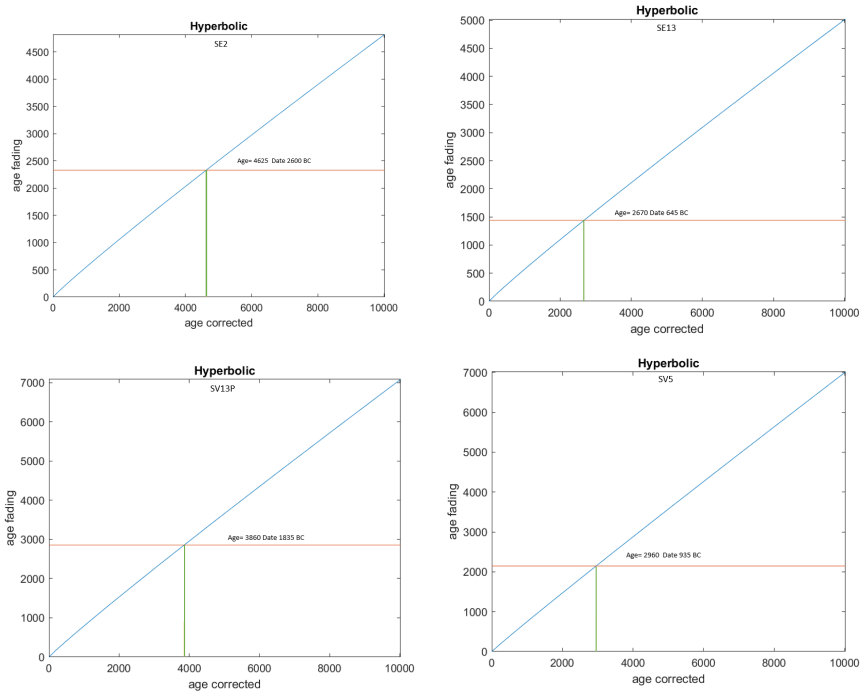

Figure 12.10: Correction of age affected by fading. The conjunction point leads to the corrected age obtained from the equivalent dose

Among the samples examined, **SE9** from the substrate rock category stands out as having likely remained unaltered by heating processes. The calculated age places it within a specific geological epoch. Situated on the north-est slopes of Mount Serravuda, SE9 was employed as the foundation rock upon which the wall was constructed. The available data strongly suggests that SE9

Sample	**Age** (Years)	**Date** (BC)
SE9	71820 ± 18625	69800 ± 18625
SE2	4230 ± 510	2605 ± 510
SE6	96930 ± 13540	94910 ± 13542
SE7	1955 ± 40	70AD ± 40
SE12	2490 ± 60	470 ± 60
SE13	2670 ± 165	645 ± 165
SV 13P	3860 ± 530	1835 ± 530
SV 4C	2980 ± 205	965 ± 205
SV5	2960 ± 400	935 ± 400
SV6	3030 ± 15	1010 ± 15
SV 1A	1455 ± 715	570 AD± 715
SV 1B	1650 ± 135	370 AD ± 135
SV 13V	1610 ± 120	415± 120
SV 4V	2565 ± 25	545 ± 25

Table 12.6: Age result on vitrified forts after fading correction

may not have undergone the processes of heating and vitrification.

Another noteworthy specimen that appears to have escaped the effects of heating is **SE6**. The mineralogical composition of this sample, as previously discussed by Elmi, suggest questions regarding the exact processes that led to vitrification [113]. The presence of cohesite in association with cristobalite, combined with the absence of any signs of heating, leads us to speculate that this sample might be an extraterrestrial body, possibly impacted near the site long before the presence of any civilization. For lack of knowledge regarding the sample's specific location within the wall, we can only speculate as to why it did not undergo heating during the vitrification process.

In contrast, samples **SV1A** and **SV1B**, indicated as vitrified cements, have ages that after year 0. These samples exhibit clear similarities in their heating histories. Their use as cements within the wall itself suggests the hypothesis that they were added at a later stage, likely for purposes of repair or reinforcement of the wall structure. As the exact time of the site's abandonment remains uncertain, is only a conjecture that the wall underwent some form of remodelling.

Conversely, the two samples categorized as glass cements (**SV 13V** and **SV 4V**) present an entirely distinct chronology. Their initial classification was based on visual appearance, but upon further examination via thermoluminescence and comparison with samples extracted from the same block, it becomes evident that SV 13P and SV 4C diverge from their potential use as cements added subsequent to the wall's construction.

The majority of the remaining samples appear to have experienced some degree of heating, even if with variable ages, generally fall within the time frame in which there is certainty of settlement presence in the area (after 4000 BC). In particular, two samples, **SE7** and **SV 13V**, show very young ages. However, it should be noted that SV 13V, upon closer analysis, include sample SV 13P, which, interestingly, turns out to be the oldest among them. While for the SE7 sample, a discussion is ongoing to understand whether its very dark colour can somehow limit its luminescence. In the case of sample **SE2**, its accurate age for fading is evident. It's noteworthy, however, that the non-fading-corrected aliquots indicated an age of approximately 2330 years, which aligns the sample's dating more closely with the other samples, placing it around 305 BC.

A comprehensive chronological distribution in relation to the Bronze Age is graphically presented in the accompanying figures 12.11 and 12.12.

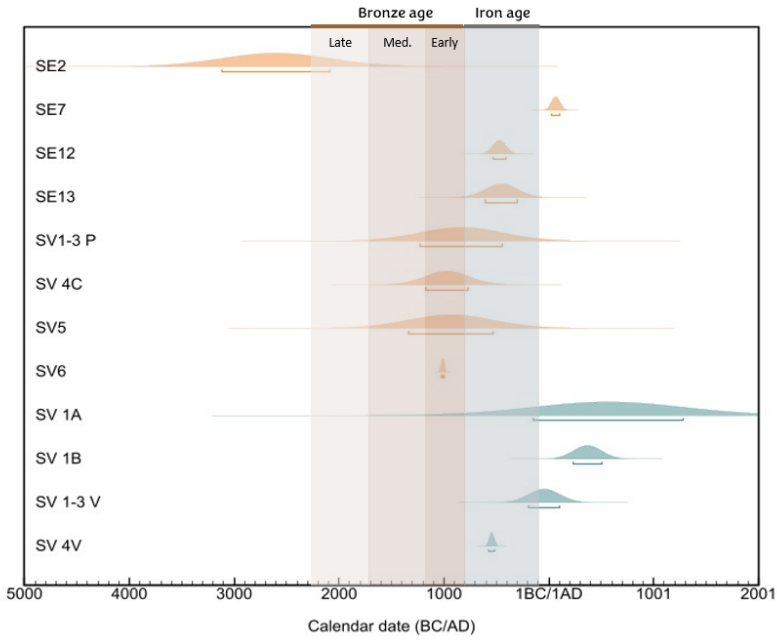

Figure 12.11: Final date ranges in correspondence to the Bronze and Iron Ages in southern Italy. In orange are samples belonging to the category of heated or partially vitrified rocks. In light blue the vitreous cements.

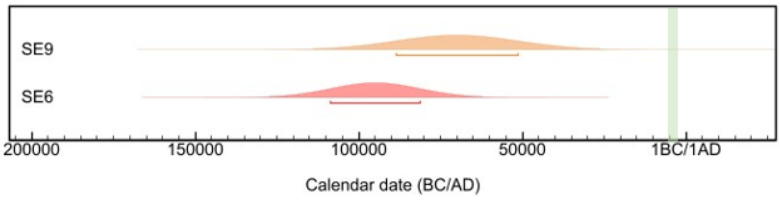

Figure 12.12: Final date ranges for samples SE6 and SE9. Highlighted in green is the civilization period of the area.

13 Conclusion on Vitrified Forts

The research on vitrified forts aimed to shed light on whether the processes leading to their formation were driven by human activity or natural occurrences. These vitrified materials were unearthed on the slopes of Mount Serravuda, in Acri, Cosenza, located in the Calabria region. The forts seem to protect an ancient occupation site, with initial findings dating back to 4000 BC. Petrographic, lithographic, and chemical analyses conducted by the University of Modena and Reggio Emilia provided initial insights into the origin of these artifacts.
Petrographic examinations of the rocks revealed the presence of minerals that form at temperatures exceeding 1100°C. The question of whether this heating was deliberate or accidental is a matter of ongoing debate. The collected samples were categorized into groups based on their lithological characteristics and, more significantly, their roles within the vitrified walls. These groups are vitreous cements, rocks that had been subjected to heating or partial vitrification, and substrate rocks. Preliminary analyses suggest that these samples likely to demostrate the anthropogenic activities, possibly involving the insertion of wooden pales within the structure.

Thermoluminescence analysis was conducted with the aim of support the initial hypotheses and reinforcing the thesis regarding ancient activities. Dating glassy materials gives numerous challenges due to their unique structural properties.
This thesis has demonstrated how a protocol like ”pre-bleached with blue LED”, originally designed for different purposes, can be effectively adapted for dating applications. After its successful application in dating glass mosaic tiles, the protocol also yielded promising results in determining the age of vitrified forts discovered on Mount Serravuda. The protocol facilitated the

isolation of the most stable portion of the thermoluminescence glow curve. Among the fourteen samples subjected to analysis, four required corrections due to the presence of the fading effect. These corrections were meticulously applied using a specialized protocol tailored to glassy materials, which had been rigorously tested and customized for this specific purpose.
We can confidently assert that the majority of the samples had undergone significant heating events. Many of these samples can be dated to a period extending back at least 3000 years, strongly indicating their origins during a period when clear signs of settlement were evident in the analysis area.

Thermoluminescence analysis provided valuable dating information regarding the heating events and further substantiated the viability of the "pre-bleached with blue LED" protocol as a potential tool for dating glassy materials. The proposed protocol holds promise for accurately dating vitrified materials, avoiding the pitfalls encountered by traditional thermoluminescence dating, which has sometimes yielded results too recent or too old in cases of vitrified forts samples.

14 Publications and other activities

1. Saleh, M.; Polymeris, G.S.; Panzeri, L.; Tsoutsoumanos, E.; Ricci, G.; Secco, M.; Martini, M.; Artioli, G.; Dilaria, S.; Galli, A. Analysis probes and statistical parameters affecting the OSL ages of mortar samples; a case study from Italy in *Radiation Physics and Chemistry*, 214, 2024.

2. Tsoutsoumanos, E.; Saleh, M.; Konstantinidis, P.G.; Altunal, V.; Sahare, P.D.; Yengigil, Z.; Karakasidis, T.; Kitis, G.; Polymeris, G.S. Nanostructured TLDs: Studying the impact of crystalline size on the Thermoluminescence glow-curve shape and electron trapping parameters in *Radiation Physics and Chemistry*, 212, 2023. doi: 10.1016/j.radphyschem.2023.111067

3. Panzeri, L.; Galli, A.; Maspero, F.; Saleh, M.; Martini, M. The activities of the LAMBDA (Laboratory of Milano Bicocca University for Dating and Archaeometry): What's new? in *Journal of Physics: Conference Series*, 2204(1), 2022. doi: 10.1088/1742-6596/2204/1/012047

4. Saleh M.; Validation with Raman spectroscopy of lapis lazuli provenance study in *Il Nuovo Cimento*, 44C, 24, pp. 1-10, 2021. doi: 10.1393/ncc/i2021-21024-7

5. Saleh M.; TL, OSL and IRSL dating on ancient ceramics in the context of the European project nEU-MED in *Ancient TL*, 38(2), 2020.

6. Saleh M.; Bonizzoni L.; Orsilli J.; Samela S.; Gargano M.; Gallo S.; Galli A. Application of Statistical Analyses for LapisLazuli Stone Provenance Determination by XRL and XRF. In *Microchemical Journal 154*, 2020, p. 104655. issn: 0026265X. doi: 10.1016/j.microc.2020.104655

Meeting and conference

1. $25^{th} - 30^{th}$ June 2023, Copenhagen, 17th International Luminescence and Electron Spin Resonance Dating conference (LED) - M. Saleh, G. Sighinolfi, A. Galli; The "Pre-bleach with blue LEDs" protocol: A unique TL dating on Italian vitrified forts. [Poster]

2. $19^{th} - 21^{th}$ April 2023, Messina, XII Congresso Nazionale AIAr -M. Saleh, L. Panzeri, G.S. Polymeris, E. Tsoutsoumanos, G. Ricci, M. Secco, G. Artioli, S. Dilaria, M. Martini, A. Galli; The impact of statistical analysis in OSL mortar dating. [Speaker]

3. $26^{th} - 28^{th}$ September 2022, Ankara, Turkey, 6th APLED- Asia Pacific Conference on Luminescence and Electron Spin Resonance Dating - M. Saleh, G.S. Polymeris, L. Panzeri, E. Tsoutsoumanos, G. Ricci, M. Secco, G. Artioli, S. Dilaria, M. Martini, A. Galli; Analysis probes and statistical parameters affecting the OSL ages of mortar samples - a case study from Italy [Speaker]

4. $6^{th} - 8^{th}$ October 2022, Kalamata, 7th ARCH RNT Archaeological Research and New Technologies -M. Saleh, L. Panzeri, G.S. Polymeris, E. Tsoutsoumanos, G. Ricci, M. Secco, G. Artioli, S. Dilaria, M. Martini, A. Galli; Beyond bleaching in OSL mortar dating: statistical data treatment on northen Italy samples. [Speaker]

5. $28^{th} - 23^{th}$ July 2021, Napoli Italy, XI Congresso Nazionale AIAr - M.Saleh, L.Bonizzoni, J.Orsilli, A.Galli; Lapislazuli Stones provenance by XRL and XRF: A check of the method through Raman spectroscopy. [Poster]

6. 18^{th} December2020, Milano Italy, A Conservation Carol 2020 La diagnostica: punto di incontro nel mondo dei beni culturali - Character: organizing committee.[Workshop]

7. $14^{th} - 16^{th}$ September 2020, Milano Italy, 106° Congresso Nazionale Società Italiana di Fisica (SIF) - M.Saleh, Studio di provenienza di Lapislazzuli con analisi XRF, XRL e Raman. [Speaker]

Awards/grants

1. Special mention at 106° Congresso Società Italiana di Fisica

Research abroad

June-December 2022
Period Abroad at NCSR Demokritos - Institute of Nanoscience and Nanotechnology, Athens, Greece
Supervisor: Professor G.S. Polymeris

Teaching activities, third mission

1. Tutoring for the course "Advanced physical techniques for cultural heritage" - Università degli studi di Milano, Supervisor: prof. Nicola G. Ludwig, Flavia M. Groppi Garlandini. (accademic years: 2020-2021, 2021-2022, 2022-2023)

2. Professor of chemistry and physics at Professional Training Centre Giuseppe Terragni - Afol Monza Brianza in the course of wooden cultural heritage restoration technician (academic year: 2022-2023)

3. Speaker in extracurricular activities (PCTO) in Secondary school classes Project 'Ambassadors of Science' - Milan Bicocca University (academic year: 2022-2023)

4. Ph.D Seminars School of Science organization - University Milano Bicocca (January - November 2023)

5. 19th April 2020 - Speaker for the "Pills of the Future" project promoted by the Salesian Institute - Second Level Secondary School "Ernesto Breda" and "Enrico Falck" Centro di Formazione Professionale.

6. I was elected representative of the students of my Ph.D Cycle. My representation developed into doctoral school academic board

Following this section will show the articles in order of publication as indicated

Bibliography

[1] A. G. Wintle. Fifty years of luminescence dating. *Archaeometry*, 50(2):276–312, April 2008.

[2] Geoff Duller. *Luminescence Dating : Guidelines on using luminescence dating in archaeology*. English heritage, September 2008.

[3] M.J. Aitken. *Thermoluminescence dating*. London: Academic Press, 1985.

[4] L. Bøtter-Jensen, S. W. S. McKeever, and A. G. Wintle. *Optically stimulated luminescence dosimetry*. Elsevier, Amsterdam ; Boston ; London, 1st ed edition, 2003. OCLC: ocm52696099.

[5] G. Artioli, M. Secco, and A. Addis. The Vitruvian legacy: Mortars and binders before and after the Roman world. In Gilberto Artioli, editor, *The contribution of mineralogy to cultural heritage*, pages 151–202. Mineralogical Society of Great Britain & Ireland, 1 edition, August 2019.

[6] L. Hobbs and R. Siddal. Cementitious materials of the ancient word. *The Finnish Society of Sciences and Letters*, 128:35–60, 2011.

[7] Gino Mircole Crisci, Marco Franzini, Marco Lezzerini, Tiziano Mannoni, and Maria Pia Riccardi. Ancient mortars and their binder. *Periodico di Mineralogia*, page 11, 2004.

[8] Lynne C. Lancaster. Mortars and plasters—How mortars were made. The literary sources. *Archaeological and Anthropological Sciences*, 13(11):192, November 2021.

[9] John Hale, Jan Heinemeier, Alf Lindroos, Lynne Lancaster, and Åsa Ringbom. Dating Ancient Mortar. *American Scientist*, 91(2):130, 2003.

[10] Olga Cazalla, Carlos Rodriguez-Navarro, Eduardo Sebastian, Giuseppe Cultrone, and Maria Jose Torre. Aging of Lime Putty: Effects on Traditional Lime Mortar Carbonation. *Journal of the American Ceramic Society*, 83(5):1070–1076, December 2004.

[11] Maria Goreti Margalha, António Santos Silva, Maria Do Rosário Veiga, Jorge De Brito, Richard James Ball, and Geoffrey Charles Allen. Microstructural Changes of Lime Putty during Aging. *Journal of Materials in Civil Engineering*, 25(10):1524–1532, October 2013.

[12] R. Chen and S.W.S. McKeever. *Theory of Thermoluminescence and Related Phenomena*. World Scientific, 1997.

[13] M. Martini and F. Meinardi. Thermally stimulated luminescence: New perspectives in the study of defects in solids. *La Rivista del Nuovo Cimento*, 20(8):1–71, August 1997.

[14] D. W. Zimmerman. Thermoluminescence Dating Using Fine Grain from Pottery. *Archaeometry*, 13:29–52, 1971.

[15] M.J. Aitken. *An Introduction to Optical Dating. The Dating of Quaternary Sediments by the Use of Photon-Stimulated Luminescence*. Oxford University Press, Oxford, 1998.

[16] D. J. Huntley, D. I. Godfrey-Smith, and M. L. W. Thewalt. Optical dating of sediments. *Nature*, 313(5998):105–107, January 1985.

[17] S.J Fleming. Thermoluminescent Dating: Refinement of the Quartz Inclusion Method. *Archaeometry*, 12(2):133–143, 1970.

[18] Frank Preusser, Detlev Degering, Markus Fuchs, Alexandra Hilgers, Annette Kadereit, Nicole Klasen, Matthias Krbetschek, Daniel Richter, and Joel Q. G. Spencer. Luminescence dating: basics, methods and applications. *E&G Quaternary Science Journal*, 57(1/2):95–149, August 2008.

[19] R.M. Bailey, B.W. Smith, and E.J. Rhodes. Partial bleaching and the decay form characteristics of quartz OSL. *Radiation Measurements*, 27(2):123–136, April 1997.

[20] J.S. Singarayer and R.M. Bailey. Further investigations of the quartz optically stimulated luminescence components using linear modulation. *Radiation Measurements*, 37(4-5):451–458, August 2003.

[21] A.G. Wintle and A.S. Murray. A review of quartz optically stimulated luminescence characteristics and their relevance in single-aliquot regeneration dating protocols. *Radiation Measurements*, 41(4):369–391, April 2006.

[22] R.M Bailey. The slow component of quartz optically stimulated luminescence. *Radiation Measurements*, 32(3):233–246, June 2000.

[23] B.W. Smith and E.J. Rhodes. Charge movements in quartz and their relevance to optical dating. *Radiation Measurements*, 23(2-3):329–333, April 1994.

[24] A.S. Murray and A.G. Wintle. Isothermal decay of optically stimulated luminescence in quartz. *Radiation Measurements*, 30(1):119–125, February 1999.

[25] L. Bøtter-Jensen, S. Solongo, A.S. Murray, D. Banerjee, and H. Jungner. Using the OSL single-aliquot regenerative-dose protocol with quartz extracted from building materials in retrospective dosimetry. *Radiation Measurements*, 32(5-6):841–845, December 2000.

[26] A.S. Murray and A.G. Wintle. Luminescence dating of quartz using an improved single-aliquot regenerative-dose protocol. *Radiation Measurements*, 32(1):57–73, February 2000.

[27] A.S. Murray and A.G. Wintle. The single aliquot regenerative dose protocol: potential for improvements in reliability. *Radiation Measurements*, 37(4-5):377–381, August 2003.

[28] Andrew S. Murray and Richard G. Roberts. Determining the burial time of single grains of quartz using optically stimulated luminescence. *Earth and Planetary Science Letters*, 152(1-4):163–180, November 1997.

[29] Christian Goedicke. Dating mortar by optically stimulated luminescence: A feasibility study. *Geochronometria*, 38(1):42–49, March 2011.

[30] M.J. Aitken, M.S Tite, and J. Reid. Thermoluminescent dating of ancient ceramics. *Nature*, 202:1032–1033, 1964.

[31] M. J. Aitken, D. W. Zimmerman, and S. J. Fleming. Thermoluminescent Dating of Ancient Pottery. *Nature*, 219(5153):442–445, August 1968.

[32] S. J. Fleming. *Thermoluminescence Techniques Archaeology*. Oxford University Press, 1979.

[33] C. Goedicke, K. Slusallek, and M. Kubelik. Thermoluminescence Dating in Architectural History: Venetian Villas. *Journal of the Society of Architectural Historians*, 40(3):203–217, 1981.

[34] I. Liritzis, P. Guibert, F. Foti, and M. Schvoerer. The temple of Apollo (Delphi) strengthens novel thermoluminescence dating method. *Geoarchaeology - An International Journal*, 12(5):479–496, 1997.

[35] G. Hutt, H.Y. Göksu, I. Jaek, and M. Hiekkanen. Luminescence dating of Somero sacristy, SW Finland using the 2103C TL peak of quartz. *Quaternary Science Reviews*, 2001.

[36] Marco Martini, Emanuela Sibilia, Silvia Croci, and Mauro Cremaschi. Thermoluminescence (TL) dating of burnt flints: problems, perspectives and some examples of application. *Journal of Cultural Heritage*, 2(3):179–190, September 2001.

[37] Elina Aidona, George S. Polymeris, Pierre Camps, Despina Kondopoulou, Nikos Ioannidis, and Konstantinos Raptis. Archaeomagnetic versus luminescence methods: the case of an Early Byzantine ceramic workshop in Thessaloniki, Greece. *Archaeological and Anthropological Sciences*, 10(4):725–741, June 2018.

[38] Anna Galli, Emanuela Sibilia, and Marco Martini. Ceramic chronology by luminescence dating: how and when it is possible to date ceramic artefacts. *Archaeological and Anthropological Sciences*, 12(8):190, August 2020.

[39] M. Martini and E. Sibilia. Absolute dating of historical buildings: the contribution of thermoluminescence (TL). *Journal of Neutron Research*, 14(1):69–74, March 2006.

[40] Irka Hajdas, Alf Lindroos, Jan Heinemeier, Åsa Ringbom, Fabio Marzaioli, Filippo Terrasi, Isabella Passariello, Manuela Capano, Gilberto Artioli, Anna Addis, Michele Secco, Danuta Michalska, Justyna Czernik, Tomasz Goslar, Roald Hayen, Mark Van Strydonck, Laurent Fontaine, Mathieu Boudin, Francesco Maspero, Laura Panzeri, Anna Galli, Petra Urbanová, and Pierre Guibert. Preparation and Dating of Mortar Samples—Mortar Dating Inter-Comparison Study (MODIS). *Radiocarbon*, 59(6):1845–1858, December 2017.

[41] Roald Hayen, Mark Van Strydonck, Laurent Fontaine, Mathieu Boudin, Alf Lindroos, Jan Heinemeier, Åsa Ringbom, Danuta Michalska, Irka Hajdas, Sophie Hueglin, Fabio Marzaioli, Filippo Terrasi, Isabella Passariello, Manuela Capano, Francesco Maspero, Laura Panzeri, Anna Galli, Gilberto Artioli, Anna Addis, Michele Secco, Elisabetta Boaretto, Christophe Moreau, Pierre Guibert, Petra Urbanova, Justyna Czernik, Tomasz Goslar, and Marta Caroselli. Mortar Dating Methodology: Assessing Recurrent Issues and Needs for Further Research. *Radiocarbon*, 59(6):1859–1871, December 2017.

[42] C. Goedicke. Dating historical calcite mortar by blue OSL: results from known age samples. *Radiation Measurements*, 37(4-5):409–415, August 2003.

[43] Laura Panzeri. Mortar and surface dating with Optically Stimulated Luminescence (OSL): Innovative techniques for the age determination of buildings. *Il Nuovo Cimento C*, 36(4):205–216, July 2013.

[44] Miriam Saleh, Georgios S. Polymeris, Laura Panzeri, Efstathios Tsoutsoumanos, Giulia Ricci, Michele Secco, Marco Martini, Gilberto Artioli, Simone Dilaria, and Anna Galli. Analysis probes and statistical parameters affecting the OSL ages of mortar samples; a case study from Italy. *Radiation Physics and Chemistry*, page 111298, September 2023.

[45] L. Panzeri, M. Caroselli, A. Galli, S. Lugli, M. Martini, and E. Sibilia. Mortar OSL and brick TL dating: The case study of the UNESCO world heritage site of Modena. *Quaternary Geochronology*, 49:236–241, February 2019.

[46] L Panzeri, A. Galli, F Maspero, M Saleh, and M Martini. The activities of the LAMBDA (Laboratory of Milano Bicocca university for Dating and Archaeometry): what's new? *Journal of Physics: Conference Series*, 2204(1):012047, April 2022.

[47] Giuseppe Stella, Luis Almeida, Lilia Basílio, Stefania Pasquale, Jorge Dinis, Miguel Almeida, and Anna M. Gueli. Historical building dating: A multidisciplinary study of the Convento de São Francisco (Coimbra, Portugal). *Geochronometria*, 45(1):119–129, July 2018.

[48] N. Zacharias, B. Mauz, and C. T. Michael. Luminescence Quartz Dating of Lime Mortars. A First Research Approach. *Radiation Protection Dosimetry*, 101(1):379–382, August 2002.

[49] Anna Gueli. Historical buildings: Luminescence dating of fine grains from bricks and mortar. *Il Nuovo Cimento B*, 125(506):719–729, July 2010.

[50] Giuseppe Stella, Dorotea Fontana, Anna Gueli, and Sebastiano Troja. Historical mortars dating from OSL signals of fine grain fraction enriched in quartz. *Geochronometria*, 40(3):153–164, September 2013.

[51] Petra Urbanová, Elisabetta Boaretto, and Gilberto Artioli. The State-of-the-Art of Dating Techniques Applied to Ancient Mortars and Binders: A Review. *Radiocarbon*, 62(3):503–525, June 2020.

[52] Laura Panzeri, Michela Cantù, Marco Martini, and Emanuela Sibilia. Application of different protocols and age-models in OSL dating of earthen mortars. *Geochronometria*, 44(1):341–351, December 2017.

[53] Petra Urbanová and Pierre Guibert. Methodological study on single grain OSL dating of mortars: Comparison of five reference archaeological sites. *Geochronometria*, 44(1):77–97, April 2017.

[54] R. F. Galbraith, R. G. Roberts, G. M. Laslett, H. Yoshida, and J. M. Olley. Optical dating of single and multiple grains of quartz from jinmium rock shelter, Northern Australia: part i, experimental design and statistical models. *Archaeometry*, 41(2):339–364, August 1999.

[55] R.F. Galbraith and R.G. Roberts. Statistical aspects of equivalent dose and error calculation and display in OSL dating: An overview and some recommendations. *Quaternary Geochronology*, 11:1–27, August 2012.

[56] Alastair C. Cunningham and Jakob Wallinga. Selection of integration time intervals for quartz OSL decay curves. *Quaternary Geochronology*, 5(6):657–666, December 2010.

[57] Guillaume Guérin, Benoit Combès, Christelle Lahaye, Kristina Thomsen, Chantal Tribolo, Petra Urbanova, Pierre Guibert, Norbert Mercier, and Hélène Valladas. Testing the accuracy of a Bayesian central-dose model for single-grain OSL, using known-age samples. *Radiation Measurements*, 81, April 2015.

[58] K.J. Thomsen, A.S. Murray, and L. Bøtter-Jensen. Sources of variability in OSL dose measurements using single grains of quartz. *Radiation Measurements*, 39(1):47–61, January 2005.

[59] Pierre Guibert, Claire Christophe, Petra Urbanová, Guillaume Guérin, and Sophie Blain. Modeling incomplete and heterogeneous bleaching of mobile grains partially exposed to the light: Towards a new tool for single grain OSL dating of poorly bleached mortars. *Radiation Measurements*, 107:48–57, December 2017.

[60] Guillaume Guérin, Christelle Lahaye, Maryam Heydari, Martin Autzen, Jan-Pieter Buylaert, Pierre Guibert, Mayank Jain, Sebastian Kreutzer, Brice Lebrun, Andrew S. Murray, Kristina J. Thomsen, Petra Urbanova, and Anne Philippe. Towards an improvement of optically stimulated luminescence (OSL) age uncertainties: modelling OSL ages with systematic errors, stratigraphic constraints and radiocarbon ages using the R package BayLum. *Geochronology*, 3(1):229–245, April 2021.

[61] Kristina J. Thomsen, Andrew Murray, and Mayank Jain. The dose dependency of the over-dispersion of quartz OSL single grain dose distributions. *Proceedings of the 13th International Conference on Luminescence and Electron Spin Resonance Dating, 10–14 July, 2011, Toruń, Poland*, 47(9):732–739, September 2012.

[62] M. Jain, A.S. Murray, and L. Bøtter-Jensen. Characterisation of blue-light stimulated luminescence components in different quartz samples: implications for dose measurement. *Radiation Measurements*, 37(4-5):441–449, August 2003.

[63] Zhixiong Shen and Andreas Lang. Quartz fast component optically stimulated luminescence: Towards routine extraction for dating applications. *Radiation Measurements*, 89:27–34, June 2016.

[64] G. Kitis and V. Pagonis. Computerized curve deconvolution analysis for LM-OSL. *Radiation Measurements*, 43(2-6):737–741, February 2008.

[65] J H Choi, G A T Duller, and A G Wintle. Analysis of quartz LM-OSL curves. *Ancient TL*, 24:13, 2006.

[66] G.S. Polymeris, S. Çoskun, E. Tsoutsoumanos, P. Konstantinidis, E. Aşlar, E. Şahiner, N. Meriç, and G. Kitis. Dose response features of quenched and reconstructed, TL and deconvolved OSL signals in BeO. *Results in Physics*, 25:104222, June 2021.

[67] D. Afouxenidis, G. S. Polymeris, N. C. Tsirliganis, and G. Kitis. Computerised curve deconvolution of TL/OSL curves using a popular spreadsheet program. *Radiation Protection Dosimetry*, 149(4):363–370, May 2012.

[68] George Kitis, George Polymeris, Nafiye Kiyak, and Vasilis Pagonis. Preliminary results towards the equivalence of transformed continuous-wave Optically Stimulated Luminescence (CW-OSL) and linearly-modulated (LM-OSL) signals in quartz. *Geochronometria*, 38(3):209–216, September 2011.

[69] Ş. Kaya-Keleş, G.S. Polymeris, and N. Meriç. A component resolved study on the stable signal of Merck -quartz: Tentative correlation among TL peaks, OSL components and EPR signals. *Nuclear Instruments and Methods in Physics Research Section B: Beam Interactions with Materials and Atoms*, 458:44–56, November 2019.

[70] Garo Balian and Nelson Eddy. Figure-of-merit (fom), an improved criterion over the normalized chi-squared test for assessing goodness-of-fit of gamma-ray spectral peaks. *Nuclear Instruments and Methods in Physics Research Section B: Beam Interactions with Materials and Atoms*, 145:389–395, 1977.

[71] Vasilis Pagonis, Nathan D. Brown, Jun Peng, George Kitis, and George S. Polymeris. On the deconvolution of promptly measured luminescence signals in feldspars. *Journal of Luminescence*, 239:118334, November 2021.

[72] A. Bluszcz and G. Adamiec. Application of differential evolution to fitting OSL decay curves. *Radiation Measurements*, 41(7-8):886–891, August 2006.

[73] Balanda and MacGillivray. Kurtosis: A Critical Review. *The American Statistician*, 42:10, 1988.

[74] D. N. Joanes and C. A. Gill. Comparing measures of sample skewness and kurtosis. *Journal of the Royal Statistical Society: Series D (The Statistician)*, 47(1):183–189, March 1998.

[75] Tae-Hwan Kim and Halbert White. On more robust estimation of skewness and kurtosis. *Finance Research Letters*, 1(1):56–73, March 2004.

[76] K V Mardia. Measures of Multivariate Skewness and Kurtosis with Applications. *Oxford University Press on behalf of Biometrika Trust*, 57:13, 1970.

[77] Ehri Ryu. Effects of skewness and kurtosis on normal-theory based maximum likelihood test statistic in multilevel structural equation modeling. *Behavior Research Methods*, 43(4):1066–1074, December 2011.

[78] John L. Lawless, R. Chen, and V. Pagonis. Effect of radiation physics on inherent statistics of glow curves from small samples or low doses. *Radiation Measurements*, 151:106698, February 2022.

[79] George Polymeris. Computational and statistical analysis using raw luminescence data. Invited Oral Presentation, 6th Asian Pacific Luminescence and Electron Spin Resonance Dating (APLED) Conference, 26 – 28 September 2022, Ankara, Turkey., September 2022.

[80] Jacopo Bonetto, Elena Pettenò, Francesca Veronese, Federica Trivisonno, and Caterina Previato. Il teatro romano di Padova. *Orizzonti*, 22(22), 2021.

[81] Giulia Ricci, Michele Secco, Fabio Marzaioli, Filippo Terrasi, Isabella Passariello, Anna Addis, Paolo Lampugnani, and Gilberto Artioli. The Cannero Castle (Italy): Development of Radiocarbon Dating Methodologies in the Framework of the Layered Double Hydroxide Mortars. *Radiocarbon*, 62(3):617–631, June 2020.

[82] Graciela Ponce-Antón, Luis Ortega, Maria Zuluaga, Ainhoa Alonso-Olazabal, and Jose Solaun. Hydrotalcite and Hydrocalumite in Mortar Binders from the Medieval Castle of Portilla (Álava, North Spain): Accurate Mineralogical Control to Achieve More Reliable Chronological Ages. *Minerals*, 8(8):326, July 2018.

[83] Gilberto Artioli, Michele Secco, Anna Addis, and Maurizio Bellotto. 5. Role of hydrotalcite-type layered double hydroxides in delayed pozzolanic reactions and their bearing on mortar dating: Composition, Properties, Application. In *Cementitious Materials*. De Gruyter, December 2017. Journal Abbreviation: Cementitious Materials.

[84] Philip Harsh. The Origins of the "Insulae" at Ostia. *Memoirs of the American Academy in Rome*, 12:7–66, 1935. Publisher: [American Academy in Rome, University of Michigan Press].

[85] Leonardo Bernardi and Maria Stella Busana. The Sarno Baths in Pompeii: Context and state of the art. *Journal of Cultural Heritage*, 40:231–239, November 2019.

[86] Simone Dilaria, Caterina Previato, Michele Secco, Maria Stella Busana, Jacopo Bonetto, Jessica Cappellato, Giulia Ricci, Gilberto Artioli, and Ping Tan. Phasing the history of ancient buildings through PCA on mortars' mineralogical profiles: the example of the Sarno Baths (Pompeii). *Archaeometry*, page arcm.12746, January 2022.

[87] Gilberto Artioli, Elena Francesca Ghedini, Claudio Modena, Jacopo Bonetto, and Maria Stella Busana. Foreword: The MACH Project and the case study of the Sarno Baths in Pompeii. *Journal of Cultural Heritage*, 40:228, November 2019.

[88] Michele Secco, Caterina Previato, Anna Addis, Giulia Zago, Angelique Kamsteeg, Simone Dilaria, Caterina Canovaro, Gilberto Artioli, and Jacopo Bonetto. Mineralogical clustering of the structural mortars from the Sarno Baths, Pompeii: A tool to interpret construction techniques and relative chronologies. *Journal of Cultural Heritage*, 40:265–273, November 2019.

[89] Teresa Demauro. *Restauri a Pompei (1748-1860)*. Number 44 in Studi e ricerche del Parco archeologico di Pompei. "L'Erma" di Bretschneider, Roma, 2020.

[90] Andrea Mariani and Fabio Carminati. Atti Convegno Capiate. In *La curtis di Capiate, fra tardo antico e Medioevo- Scoperte inedite e nuove ricerche sul territorio*, page 237, Monastero di S.Maria del Lavello, Calolziocorte, May 2016.

[91] K.J. Thomsen, L. Bøtter-Jensen, M. Jain, P.M. Denby, and A.S. Murray. Recent instrumental developments for trapped electron dosimetry. *Radiation Measurements*, 43(2-6):414–421, February 2008.

[92] D. Wróbel, P. Bilski, B. Marczewska, A. Mrozik, and M. Kłosowski. Characterization of the Risø TL/OSL DA-20 reader for application in TL dosimetry. *Radiation Measurements*, 74:1–5, March 2015.

[93] WT Bell. Thermoluminescence dating: radiation dose-rate data. *Archaeometry*, 21:243–245., 1979.

[94] Anna Galli, Marco Martini, Francesco Maspero, Laura Panzeri, and Emanuela Sibilia. Surface dating of bricks, an application of luminescence techniques. *The European Physical Journal Plus*, 129(5):101, May 2014.

[95] G Guérin, N Mercier, and G Adamiec. Dose-rate conversion factors: update. *Ancient TL*, 29:5, 2011.

[96] J.R. Prescott and J.T. Hutton. Cosmic ray contributions to dose rates for luminescence and ESR dating: Large depths and long-term time variations. *Radiation Measurements*, 23(2-3):497–500, April 1994.

[97] C K Kuhns, N Agersnap Larsen, and S W S McKeever. Characteristics of LM-OSL from several different types of quartz. *Radiation Measurements*, 32:413–418, 2000.

[98] Eren Şahiner, M. Korhan Erturaç, Georgios S. Polymeris, and Niyazi Meriç. Methodological studies on integration time interval's selection for the luminescence ages using quartz and feldspar minerals; sediments collected from Sakarya, Turkey. *Radiation Measurements*, 120:163–169, December 2018.

[99] Glenn F. Knoll. *Radiation detection and measurement*. Wiley, New York, 3rd ed edition, 2000.

[100] Rolf Sjöblom, Eva Hjärthner-Holdar, Carolyn I. Pearce, Jamie L. Weaver, Erik Ogenhall, John S. McCloy, José Marcial, Edward P. Vicenzi, Michael J. Schweiger, and Albert A. Kruger. Assessment of the reason for the vitrification of a wall at a hillfort. The example of Broborg in Sweden. *Journal of Archaeological Science: Reports*, 43:103459, June 2022.

[101] James Smith. III. Notice of an undescribed Vitrified Fort, in the Burnt Isles, in the Kyles of Bute. *Earth and Environmental Science Transactions of The Royal Society of Edinburgh*, 10(1):79–81, 1826. Edition: 2013/01/17 Publisher: Royal Society of Edinburgh Scotland Foundation.

[102] David Christison. *Early fortifications in Scotland : motes, camps, and forts / by David Christison.* Rhind lectures in archaeology; 1894. W. Blackwood and Sons, Edinburgh, 1898.

[103] M'Hardy. m Hardy 1906.pdf. ***On Vitrified Forts, with Results of Experiments as to the Probable Manner in Which Their Vitrification May Have Been Produced.***, February 1906.

[104] A vitrified fort at Dunagoil, Buteshire. *Nature*, 119(2988):213, 1927.

[105] V Gordon Childe. Excavation of the Vitrified Fort of Finavon, Angus. *Proceedings of the Society of Antiquaries of Scotland*, 69:49–80, November 1935.

[106] V Gordon Childe, Wallace Thorneycroft, and Cecil H Desch. The Vitrified Fort at Rahoy, Morvern, Argyll. *Proceedings of the Society of Antiquaries of Scotland*, 72:23–43, November 1938.

[107] V Gordon Childe and Wallace Thorneycroft. The Experimental Production of the Phenomena Distinctive of Virtified Forts. *Proceedings of the Society of Antiquaries of Scotland*, 72:44–55, November 1938.

[108] Helen C Nisbet. A geological approach to vitrified forts. *Sci. Archaeol*, 12:3–12, 1974.

[109] Peter Kresten and Björn Ambrosiani. Swedish vitrified forts - a reconnaissance study. *Journal of swedish antiquarian research*, 1992.

[110] Luis Berrocal-Rangel, Rosario García-Giménez, Lucía Ruano, and Raquel Vigil de la Villa. Vitrified Walls in the Iron Age of Western Iberia: New Research from an Archaeometric Perspective. *European Journal of Archaeology*, 22(2):185–209, May 2019.

[111] Neil Suttie and Catherine M. Batt. Re-evaluating archaeomagnetic dates of the vitrified hillforts of Scotland. *Journal of Archaeological Science: Reports*, 30:102233, April 2020.

[112] John S. McCloy, José Marcial, Jack S. Clarke, Mostafa Ahmadzadeh, John A. Wolff, Edward P. Vicenzi, David L. Bollinger, Erik Ogenhall, Mia Englund, Carolyn I. Pearce, Rolf Sjöblom, and Albert A. Kruger. Reproduction of melting behavior for vitrified hillforts based on amphibolite, granite, and basalt lithologies. *Scientific Reports*, 11(1):1272, January 2021.

[113] Chiara Elmi, Anna Cipriani, Federico Lugli, and Giampaolo Sighinolfi. Insights on the Origin of Vitrified Rocks from Serravuda, Acri (Italy): Rock Fulgurite or Anthropogenic Activity? *Geosciences*, 11(12):493, December 2021.

[114] D.C.W. Sanderson, S.E. Warren, and J.R. Hunter. *The TL properties of archaeological glass*. Risoe National Laboratory, Denmark, 1983.

[115] D.C.W. Sanderson, F. Placido, and J.O. Tate. Scottish vitrified forts: Background and potential for TL dating. *Nuclear Tracks and Radiation Measurements (1982)*, 10(4-6):799–809, January 1985.

[116] D.C.W. Sanderson. *Thermoluminescence dating on scottish vitrified forts*. PhD thesis, University of Glasgow, 1987.

[117] D.C.W. Sanderson, F. Placido, and J.O. Tate. Scottish vitrified forts: TL results from six study sites. *International Journal of Radiation Applications and Instrumentation. Part D. Nuclear Tracks and Radiation Measurements*, 14(1-2):307–316, January 1988.

[118] Gianluca Catanzariti, Gregg McIntosh, António M. Monge Soares, Enrique Díaz-Martínez, Peter Kresten, and M.L. Osete. Archaeomagnetic dating of a vitrified wall at the Late Bronze Age settlement of Misericordia (Serpa, Portugal). *Journal of Archaeological Science*, 35(5):1399–1407, May 2008.

[119] C.R.L. Friend, J. Dye, and M.B. Fowler. New field and geochemical evidence from vitrified forts in South Morar and Moidart, NW Scotland: further insight into melting and the process of vitrification. *Journal of Archaeological Science*, 34(10):1685–1701, October 2007.

[120] Clark R.L. Friend, James E. Kirby, Norman R. Charnley, and John Dye. New field, analytical data and melting temperature determinations from three vitrified forts in Lochaber, Western Highlands, Scotland. *Journal of Archaeological Science: Reports*, 10:237–252, December 2016.

[121] Peter Kresten, Christian Goedicke, and Ana Manzano. TL-dating of vitrified material. *Geochronometria*, 22:9–14, 2003.

[122] P. Müller and M. Schvoerer. Factors affecting the viability of thermoluminescence dating of glass. *Archaeometry*, 35(2):299–304, August 1993. Publisher: John Wiley & Sons, Ltd.

[123] Glenn W. Berger. The use of glass for dating volcanic ash by thermoluminescence. *Journal of Geophysical Research: Solid Earth*, 96(B12):19705–19720, November 1991. Publisher: John Wiley & Sons, Ltd.

[124] K. Rodrigues, S. Huot, and A. Keen-Zebert. Exploring the application of blue and red thermoluminescence for dating volcanic glasses. *Radiation Measurements*, 153:106731, April 2022.

[125] Cristina Chiavari, Marco Martini, Emanuela Sibilia, and Mariangela Vandini. Thermoluminescence (TL) characterisation and dating feasibility of ancient glass mosaic. *Quaternary Science Reviews*, 2001.

[126] A. Galli, M. Martini, C. Montanari, and E. Sibilia. Thermally and optically stimulated luminescence of early medieval blue-green glass mosaics. *Radiation Measurements*, 38(4-6):799–803, August 2004.

[127] A. Galli, G. Poldi, M. Martini, and E. Sibilia. Thermoluminescence and visible reflectance spectroscopy applied to the study of blue-green mosaic silica-glass tesserae. *physica status solidi c*, 4(3):950–953, March 2007.

[128] A. Galli, M. Martini, E. Sibilia, M. Vandini, and I. Villa. Dating ancient mosaic glasses by luminescence: The case study of San Pietro in Vaticano. *The European Physical Journal Plus*, 126(12):121, December 2011.

[129] Michael Discher, Céline Bassinet, and Clemens Woda. A TL study of protective glasses of mobile phones for retrospective dosimetry. *Optical Materials: X*, 18:100233, May 2023.

[130] M. Discher and C. Woda. Thermoluminescence of glass display from mobile phones for retrospective and accident dosimetry. *Radiation Measurements*, 53-54:12–21, June 2013.

[131] A. Galli, M. Caccia, M. Martini, L. Panzeri, F. Maspero, S. Fiorentino, M. Vandini, and E. Sibilia. Applying the "pre-bleached with blue LEDs" protocol to date Umayyad mosaic tesserae by thermoluminescence. *Quaternary Geochronology*, 49:218–222, February 2019.

[132] A. G. Wintle. Anomalous Fading of Thermo-luminescence in Mineral Samples. *Nature*, 245(5421):143–144, September 1973.

[133] D J Huntley and M Lamothe. Ubiquity of anomalous fading in K-feldspars and the measurement and correction for it in optical dating. *Canadian Journal of Earth Sciences*, 38(7):1093–1106, July 2001.

[134] Mario Bertolani. An enigmatic outcrop of vitrified rocks near Acri (Cosenza). Boll. Della Soc. Geol. Ital:683–692, 1972.

[135] Maurizio Gualtieri. Fortifications and settlement organization: An example from pre-Roman Italy. *World Archaeology*, 19(1):30–46, June 1987. Publisher: Routledge.